

Doctorate Dissertation

**Study on the roles of solar wind variations
and crustal magnetic fields in atmospheric
escape from Mars based on in-situ
spacecraft observations**

Takuya Hara

Graduate School of Science,
Division of Particle and Astrophysical Science,
Solar-Terrestrial Environment Laboratory (STEL),
Nagoya University.

Supervisor: Dr. Kanako Seki

February 27, 2014

Abstract

The variety of interactions between a planet and the supersonic shocked solar wind depends primarily on whether the planet possesses a global intrinsic magnetic field. Because of its global dipole intrinsic magnetic field, the Earth possesses a large magnetosphere that can prevent the solar wind from directly penetrating toward the terrestrial atmosphere; however, Mars lacks such a global intrinsic magnetic field. Because the solar wind can directly interact with the Martian upper atmosphere, the plasma environment around the unmagnetized planet is controlled by the solar wind conditions, such as the interplanetary magnetic field (IMF) strength and orientation. Moreover, Mars possesses localized crustal magnetic fields that are located primarily in the southern hemisphere [e.g., *Acuña et al.*, 1998, 1999]. The ambient electromagnetic fields around Mars are therefore expected to be highly spatiotemporally variable because the IMF embedded in the solar wind interacts with those asymmetric crustal magnetic fields.

Planetary ions can be energized through the direct interaction of the solar wind with the Martian upper atmosphere. This energization of planetary ions results in ion escape from the Martian upper atmosphere into the interplanetary space. Mars has undergone drastic climate change over its history [e.g., *Jakosky and Phillips*, 2001]; therefore investigating the present Martian atmospheric escape phenomena can provide an understanding of the evolution of the Martian atmosphere. These planetary escaping ions induced by the solar wind have been observed by several in-situ spacecraft [e.g., *Lundin et al.*, 1989; *Barabash et al.*, 2007a]. Global averaged ion escape rates, including all the possible ion escape processes caused in the Martian atmosphere, were estimated by these in-situ spacecraft observations. This results

indicate that the escape rates are largely dependent on the solar activity and solar wind conditions [e.g., *Barabash et al.*, 2007a; *Lundin et al.*, 2008a]. However, the role of solar wind variations and crustal magnetic fields have not been determined for several proposed candidates [e.g., *Chassefière and Leblanc*, 2004; *Lundin et al.*, 2007] of Martian atmospheric escape processes, based on in-situ spacecraft plasma observations. Among the candidate atmospheric escape processes, I have investigated the statistical characteristics of ion sputtering and magnetic flux ropes based on the current and previous spacecraft observations, such as those taken on the Mars Express (MEX) and Mars Global Surveyor (MGS).

Ion sputtering is a neutral escape process that can cause the precipitation of planetary heavy ions. Using the MEX ion observations, I studied the statistical properties of planetary heavy ions precipitating toward the Martian upper atmosphere. I confirmed that planetary heavy-ion signatures precipitating toward the Martian upper atmosphere are not always observed but are usually coincidental with passages of corotating interaction regions (CIRs). While the observed flux level is consistent with a previous model prediction of sputtering ions [*Chaufray et al.*, 2007], the intermittent occurrence of the planetary heavy-ion precipitation differs from the conventional expectation of constant precipitation. These results suggest that the efficiency of the sputtering process in the Martian atmospheric escape is highly variable with dynamic solar wind variations [*Hara et al.*, 2011].

Knowing the IMF orientation is important for determining the behaviors of planetary heavy ions precipitating toward the Martian upper atmosphere, because these ions are strictly controlled by the solar wind electric field directions, which depend on the solar wind bulk velocity and IMF direction. Because MEX does not carry a magnetometer, the IMF orientation is then estimated from the velocity distribution of exospheric-origin picked-up protons (ring ions) to probe the effects of the solar wind electric field on the planetary heavy-ion precipitation. The statistical study is conducted with respect to both ring ions and precipitating planetary heavy ions, as recorded by the MEX ion instrument between July 2007 and September 2009. The statistical results show that planetary heavy-ion precipitation events tend to be frequently observed in the region where the expected crustal magnetic fields is rather

small, suggesting that precipitating planetary heavy ions might also be controlled by crustal magnetic fields. The statistical results also show that the precipitation of planetary heavy ions tends to be observed around pole regions in the MSE (Mars-centered, solar electrical) coordinate system, as determined using the solar wind electric field (\mathbf{E}_{sw}), in which the pole axis directs to the parallel or anti-parallel to \mathbf{E}_{sw} because of the ambiguity in the IMF polarity determination. The observed precipitating planetary heavy ions are only accelerated up to a few keV. This feature may reflect the short distance from the picked-up region. For one event, the IMF polarity is estimated by comparing the velocity distribution of exospheric-origin pickup protons observed by MEX with those obtained from statistical trajectory tracing simulations under two cases of possible IMF polarity conditions. The estimated polarity indicates that the planetary heavy-ion precipitation for this event is likely in the downward electric field hemisphere in the MSE coordinate system where \mathbf{E}_{sw} points to Mars in the pole region [Hara *et al.*, 2013]. This tendency is consistent with the predictions obtained in previous simulations [e.g., Luhmann and Kozyra, 1991; Chaufray *et al.*, 2007].

Magnetic flux ropes are characteristically twisted and helical magnetic field structures. They can increase the atmospheric escape rates because they can confine large amounts of Martian ionospheric plasma that can be removed from the planet. However, we have not reached a consensus on the quantitative contribution of the Martian magnetic flux ropes compared to other candidate atmospheric escape processes because there is ambiguity about the estimation of their shape and size from single spacecraft measurements. It is not also easy to infer the possible formation scenarios of the observed magnetic flux ropes from the limited in-situ spacecraft observation data sets. In this study, I evaluated the spatial structure and possible formation process of the Martian magnetic flux ropes by applying the Grad-Shafranov reconstruction (GSR) technique, which can estimate both the two-dimensional spatial structure of the magnetic flux ropes and the axial orientation using single spacecraft particle and field data under the assumptions that the structure is magneto-hydrostatic, two-dimensional, and time-independent [e.g., Sturrock, 1994; Sonnerup and Guo, 1996]. Using the reconstructed spatial structures of the magnetic flux ropes, I can impose constraints on their shape and size to assess the escape rate associated with the re-

removal of ions via magnetic flux ropes propagating away from the planet.

First, I successfully recovered the spatial structures for 70 obvious magnetic flux rope events observed by MGS. The estimated flux rope axial orientation suggested that they are mostly oriented horizontal to the surface and are randomly distributed with respect to the typical plasma streamline. I found that the events observed at solar zenith angle larger than 75° with a duration longer than 240 sec are mostly observed downstream from the strong crustal magnetic field in the southern hemisphere. The estimated volumes vary by 2–3 orders of magnitude among the recovered events, and their potential escape rates are estimated to be on the order of 10^{22} – 10^{23} ions/sec [Hara *et al.*, 2014]. This estimated escape rate is approximately 10% of the global average ion escape rate (integrating all escape processes) during solar minimum [e.g., Barabash *et al.*, 2007a; Lundin *et al.*, 2008a].

In addition, I focused on the magnetic flux ropes observed downstream of the crustal magnetic fields in the southern polar region and examined whether they can be explained by the previously proposed formation processes based on GSR results suggesting that they are formed via magnetic reconnections between neighboring crustal magnetic field lines [Brain *et al.*, 2010a; Beharrell and Wild, 2012]. A statistical study of the 297 reconstructed events observed by the MGS downstream from the crustal magnetic fields indicated that two-thirds of their events can be explained by previously proposed formation scenarios; however, the remaining events cannot be explained by such scenarios. The GSR results indicated that these events might be formed by multiple magnetic reconnections between crustal and overlaid draping magnetic field lines. The resultant magnetic flux ropes should not be attached to the surface because the origin of such flux ropes is partially the result of overlaid draping magnetic field lines connecting the IMF. The spatial scale inferred from the GSR results is relatively small for the events involving overlaid draping magnetic fields. Therefore, the contribution of such magnetic flux ropes towards the ion escape rates from Mars is expected to be smaller than what has been suggested in previous studies [e.g., Brain *et al.*, 2010a].

Acknowledgments

I think there are three turning points for 5 years of my career as graduate student of science at Nagoya University, Japan. I have had so invaluable, strong interest and attraction for Mars that I asked my parents to give me a ‘Mars’ globe when I graduated from a high school. Unfortunately, Nagoya University has few science groups to be able to study a planet of Mars. That is why I was at a loss which laboratories (or perhaps universities) I should take as my graduate school of science when I was the last grade of bachelor school of science, Nagoya University. The first turning point is to come across my science supervisor, Assoc. Prof. Kanako Seki. I would like to express my largest gratitude to her, for her invaluable support and continuous guidance throughout my career as graduate student. She gave me the interesting study about the solar-wind interaction with Mars based on the knowledge of space plasma physics. I appreciate to having been given a lot of things from her, such as way of thinking, how to proceeding research, the attitude as a professional scientist, or so on.

She also encouraged me to go to the foreign institute in order to collaborate and discuss foreign researchers actively on myself. Since I had never been to any foreign countries when I entered the graduate school of science, that was big tough mission for me at first. However, I express my thanks to her recommendations now. I have been to the Swedish Institute of Space Physics (Institutet för rymdfysik, IRF), Kiruna, Sweden twice in order to study in-situ plasma data obtained by the ASPERA-3 onboard Mars Express (MEX) during the summer season in 2009, 2012. Drs. Y. Futaana, M. Yamauchi and Prof. S. Barabash at IRF-Kiruna are acknowledged to give me insightful, constructive comments and suggestions to my study based on the

MEX data. Thanks to them including all IRF members, I had fruitful experience in Kiruna to study at the frontier of the research in the solar wind interaction with unmagnetized planets, as well as to know Swedish culture, custom, and foods, or so on. In this autumn, 2013, Prof. R. Lundin, who is a principle investigator (PI) of MEX/ASPERA-3, visited our institute for about 1 month to discuss us with respect to the planetary cold ion observed by MEX/ASPERA-3. I appreciate him to help us to convert MEX/ASPERA-3 raw data to useful plasma moment data. I am sure that this collaboration is strongly leading to our next future study beyond my doctorate thesis. I express my great gratitude to all of the Mars Express members for keeping the safe operation.

The second turning point for me is that I began collaboration studies based on the Mars Global Surveyor (MGS) observations with Assist. Prof. David A. Brain at Laboratory for Atmospheric and Space Physics (LASP), University of Colorado at Boulder, USA. I met him for the first time when I gave my first English oral presentation in 5th Alfvén Conference held at Hokkaido on October 2010. He said to me that “Good presentation. Is this your first talk?” just after my oral presentation. This might be a only chat with him during this conference, but I clearly remembered his words, because his words got rid of my afraid feeling for my oral presentation, and made me happy. After about one and half year from this conference, I contacted him in order to know how to use the MGS data. I would like to heartily appreciate him that he remembered me and accepted I stayed him at LASP, University of Colorado at Boulder for twice times in 2012. He provided me with not only scientific interests of the interaction of the solar wind with Mars seen from the magnetic field data onboard MGS, but also the attitude to enjoy our science. I really enjoyed my staying at Boulder to analyze the MGS data. My doctorate thesis could not be completed his assistance and fruitful suggestions, because a half of my thesis is based on the MGS data analyses.

I am also supported by a lot of people to complete my doctorate course. I am deeply grateful to Assist. Prof. H. Hasegawa at ISAS/JAXA, and Dr. M. H. Saito to Tokyo Tech, providing me with knowledge and general idea to recover a two-dimensional magneto-hydrostatic structure from the single spacecraft plasma and

magnetic field data from the Grad-Shafranov reconstruction (GSR) technique. This technique allows us to further understand the spatial structure and potential ion escape rates of Martian magnetic flux ropes. I would like to thank all the members in STEL for helping me my scientific study life at STEL. Moreover, I would like to thank my intelligent, talented friends, who are the same grade of doctorate course students to study space plasma physics in other universities. I am happy to study with them through friendly rivalry.

The third turning point in my career is that new Mars mission, MAVEN (Mars Atmosphere and Volatile Evolution) was successfully launched on November 18, 2013. MAVEN possesses comprehensive plasma and field measurement packages to investigate the Martian plasma environment and the interaction of the solar wind with Martian upper atmosphere. MAVEN will address my study described in this thesis further. I am lucky that new Mars spacecraft strongly related to my study was successfully launched when I am the last grade of the doctorate course student. My knowledge acquired in this thesis will lead to the basis of the MAVEN data analyses.

Finally, I would like to express my grateful thanks to my parents for their permission that I can leave my hometown (Okayama) for Nagoya to enter Nagoya University, and can continue to study until I can get a doctorate of science. As final private comment for my father, I am promising him that I am going to go back to Okayama in my future, after I am able to be deeply proficient with the attractive world of the space plasma physics, based on the in-situ spacecraft observations.

Contents

Abstract	ii
Acknowledgments	vi
List of Figures	xviii
List of Tables	xx
1 Introduction	1
1.1 General Characteristics of Mars	1
1.2 Plasma Environment around Mars	3
1.3 Atmospheric Escape Processes from Unmagnetized Planet	10
1.3.1 Thermal Escape	10
1.3.2 Dissociative Recombination (DR)	11
1.3.3 Ion Pickup	12
1.3.4 Ion Sputtering	14
1.3.5 Ionospheric Outflow	15
1.4 Role of Solar Wind Variations in Atmospheric Escape	17
1.5 Role of Crustal Magnetic Fields in the Martian Plasma Environment	22
1.6 Objectives of This Thesis	28
2 Instrumentations and Data Sets	33
2.1 Mars Express (MEX)	33
2.1.1 Overview of MEX	33

2.1.2	ASPERA-3 (Analyser of Space Plasmas and Energetic Atoms)	
	Instrumentation	34
2.2	Mars Global Surveyor (MGS)	37
3	Planetary heavy-ion precipitations toward Martian ionosphere during CIR passages	39
3.1	Introduction	39
3.2	Estimation of Solar Wind Velocity from MEX Observations	41
3.3	Characteristic Planetary Heavy-Ion Enhancement Event	43
3.4	Dependence on Solar Wind Variations with Planetary Heavy-Ion Enhancements	47
3.5	Discussion of Effects of Solar Wind Variations on Planetary Heavy-Ion Precipitations	51
4	Statistical properties of planetary heavy-ion precipitations toward the Martian ionosphere	55
4.1	Introduction	55
4.2	Method of Estimating the IMF Orientation	57
	4.2.1 Automated Extraction of Ring Ions	57
	4.2.2 Determination of IMF Orientation	61
4.3	Statistical Analysis	63
4.4	IMF Polarity Assessment based on Test Particle Simulation	67
	4.4.1 Statistical Trajectory Tracings of Picked-up Exospheric Protons	67
	4.4.2 Comparisons of Velocity Distribution Functions between Simulated Test Particles and Observed Ring Ions	69
4.5	Discussion of Possible Ion Precipitation Mechanism	72
4.6	Summary	75
5	The spatial structure of Martian magnetic flux ropes recovered by the Grad-Shafranov reconstruction technique	77
5.1	Introduction	77
5.2	Grad-Shafranov Reconstruction (GSR)	81

5.2.1	Assumptions	81
5.2.2	Application Procedures	82
5.3	Application to Martian Flux Ropes	84
5.3.1	Identification of Magnetic Flux Ropes in MGS data	84
5.3.2	September 24, 1999 Event	84
5.4	Statistical Properties of Magnetic Flux Ropes	87
5.5	Magnetic Flux Rope Size Estimation	92
5.6	Summary and Discussion	95
6	Formation processes of Martian flux ropes downstream from crustal magnetic fields deduced from Grad-Shafranov reconstruction	99
6.1	Introduction	99
6.2	Identification of Magnetic Flux Ropes Candidates from MGS Data . . .	102
6.3	Application of Grad-Shafranov Reconstruction to Magnetic Flux Rope	105
6.4	Properties of Reconstructed Magnetic Flux Ropes	109
6.4.1	Axial Orientation	109
6.4.2	Dependence on Solar Wind Conditions	110
6.4.3	Flux Rope Size	115
6.5	Discussion	116
6.5.1	Formation Scenarios	116
6.5.2	Contribution to Ion Escape from Mars	122
6.6	Summary	123
7	General Conclusions and Future Perspective	127
	References	132
	Publications	151

List of Figures

1.1	Comparison between approximate relative sizes among terrestrial planets: Venus, Earth, and Mars.	2
1.2	Three-dimensional cutaway view of the Earth's magnetosphere.	4
1.3	A schematic illustration of the global Martian plasma environment [Brain, 2006].	7
1.4	Altitude profiles of Martian upper atmosphere and ionosphere based on Fox [2009].	8
1.5	A map of the global distribution of the Martian crustal magnetic field [Connerney <i>et al.</i> , 2005].	9
1.6	The summary sketch of the nonthermal escape processes from Mars. . .	11
1.7	Schematic illustration of interior magnetic field configurations of a flux rope [Russell and Elphic, 1979].	16
1.8	A typical event of cold ion escape from Mars observed by MEX [Lundin <i>et al.</i> , 2009].	18
1.9	A map of the integrated planetary heavy-ion fluxes measured by MEX/IMA in the MSE coordinate system [Barabash <i>et al.</i> , 2007a].	19
1.10	Comparison of averaged antisunward fluxes of planetary heavy ions from Mars observed by MEX/IMA during between CIR passages and 'nominal' solar wind conditions [Edberg <i>et al.</i> , 2010].	21
1.11	Evidence of aurora-like plasma acceleration around the open field line areas above the Martian crustal magnetic fields observed by MEX/ASPERA-3 instruments [Lundin <i>et al.</i> , 2006a,b].	24

1.12	Schematic illustration of the aurora-like plasma acceleration above cusps of the Martian crustal magnetic fields [<i>Lundin et al.</i> , 2006a,b].	25
1.13	A typical nightside current sheet crossing observed by MGS [<i>Halekas et al.</i> , 2006].	26
1.14	An overview of a large-scale isolated magnetic flux rope event observed by MGS in the downstream of the Martian crustal magnetic field in the southern hemisphere [<i>Brain et al.</i> , 2010a].	27
1.15	Predicted magnetic field configuration around Mars obtained from global MHD simulation taking into account the crustal magnetic fields [<i>Ma et al.</i> , 2002].	29
2.1	The IMA instrument in the vacuum chamber during calibrations [<i>Barabash et al.</i> , 2006].	35
2.2	Cross section of the IMA sensor (left) with example of the ion trajectories, and magnet separator (right) [<i>Barabash et al.</i> , 2006].	36
2.3	Schematic figure of ASPERA-3 locations on the MEX spacecraft. Reproduced from <i>Barabash et al.</i> [2006].	37
3.1	Energy-time spectrograms of ions measured by MEX/IMA during the typical CIR passage event on September 19, 2007.	44
3.2	Energy-mass distribution observed by MEX/IMA during planetary heavy-ion enhancement in the vicinity of Martian ionosphere.	46
3.3	(a) Energy-azimuth (ϕ) angle (b) Energy-elevation (θ) angle distributions observed by MEX/IMA during planetary heavy-ion enhancement in the vicinity of Martian ionosphere.	48
3.4	An overview of time series plots of the estimated solar wind conditions at Martian orbit as well as planetary heavy-ion precipitations measured by MEX from September 17 to October 11, 2007.	50
3.5	Spatial distributions of the precipitating flux at an altitude of 300 km from the Martian surface based on the results of hybrid simulation [<i>Chaufray et al.</i> , 2007]. Adapted from Figure 6 of <i>Chaufray et al.</i> [2007].	53

4.1	A typical example of the MEX ring ion observations in near the Martian bow shock on August 3, 2005.	58
4.2	An overview of the typical ring ion events observed by MEX on September 19, 2007.	60
4.3	Velocity distribution function of the ring ion population observed by MEX/IMA in the SWB coordinate system.	62
4.4	Data coverage for MEX periapsis measurements between July 2007 (Orbit # 4480) and September 2009 (Orbit # 7265).	64
4.5	Event (a) geographic and (b) solar zenith angle distribution of the 59 precipitating planetary heavy-ion events observed by MEX/IMA. . . .	65
4.6	MEX periapsis location of planetary heavy-ion precipitation events (black crosses) as a function of the solar zenith angle and crustal magnetic field strength.	65
4.7	MEX positions for the 10 planetary heavy ion precipitation events for which we successfully derived the IMF orientation in $ Y_{mse} $ - $ Z_{mse} $ projection	66
4.8	Spatial distribution of the exospheric proton number density derived from the statistical trajectory tracing under the solar wind conditions estimated for MEX orbit #4767.	69
4.9	Comparison of the velocity distribution functions between the ring ion observations by MEX/IMA and results from test particle simulation of exospheric protons between two possible IMF sector polarity cases. . .	71
4.10	Schematic illustration of a possible scenario of planetary heavy ion precipitation events.	74
5.1	GSR results of two-dimensional axial (B_z) magnetic field map of the magnetic cloud event measured by WIND satellite on October 18, 1995 [<i>Hu and Sonnerup, 2002</i>].	80
5.2	GSR results of two-dimensional axial (B_z) magnetic field map of the flux transfer event measured by Cluster spacecraft on March 8, 2003 [<i>Hasegawa et al., 2006</i>].	81

5.3	Schematic illustration of magnetic field rotation sampled by spacecraft passing through a flux rope and its hodograms in the Minimum Variance Analysis (MVA) coordinate system. Reproduced from <i>Elphic et al.</i> [1980].	85
5.4	An overview of magnetic field observations during the magnetic flux rope event recorded by MGS on September 24, 1999.	86
5.5	Hodograms of a magnetic flux rope observed by MGS on September 24, 1999 in the MVA coordinate system.	86
5.6	Results from the Grad-Shafranov reconstruction for the magnetic flux rope event using MGS data on September 24, 1999.	88
5.7	Scatter plot of the duration versus solar zenith angle of the observed magnetic flux ropes for all the 135 selected events.	89
5.8	Scatter plots of the magnetic flux rope events in which their spatial structures could be recovered by the Grad-Shafranov reconstruction technique.	90
5.9	The geographic location, viewed from above the south pole in the geographic coordinate system of the 12 magnetic flux rope events which are observed at SZA larger than 75° with duration longer than 240 sec.	91
5.10	The shifted and normalized two-dimensional axial magnetic field B_z map recovered by the GSR technique to determine the magnetic flux rope boundary.	93
5.11	Schematic illustration of the possible formation scenario of the magnetic flux rope observed downstream from the crustal magnetic fields [<i>Brain et al.</i> , 2010a].	97
5.12	Schematic illustration of the possible formation scenario of the magnetic flux rope proposed by <i>Beharrell and Wild</i> [2012].	98
6.1	The average direction of the plasma streamline of the 3,007 orbits utilized so as to conduct our statistical study of magnetic flux ropes, viewed from above the south pole.	104

6.2	Geographic distribution of the 297 identified magnetic flux ropes events, viewed from above the south pole. Magenta crosses are their observed locations.	106
6.3	An example of the GSR results for the large-scale Martian magnetic flux rope observed downstream from the crustal magnetic fields on March 21, 2005.	107
6.4	External field viewed from above the south pole, with tangential components represented by whisker length and direction originating from orbital track during the magnetic flux rope event on March 21, 2005.	108
6.5	Histogram of the 297 identified magnetic flux rope events as a function of the rope axis orientation θ in the SPC coordinate system.	110
6.6	The observed geographic location of the 297 magnetic flux rope events divided into 4 categories.	111
6.7	Three-dimensional visualization of the Martian crustal magnetic field lines, viewed from above the south pole in the geographic coordinate system, based on the Martian crustal magnetic field model [<i>Cain et al.</i> , 2003].	112
6.8	Histogram of the 297 identified magnetic flux rope events as a function of solar wind dynamic pressure P_{sw} proxy obtained from <i>Brain et al.</i> [2005].	113
6.9	Histogram of the 297 identified magnetic flux rope events as a function of the local external draped magnetic field orientation in the SPC coordinate system divided into 4 categories.	114
6.10	Schematic illustration of new possible scenarios for (a) dawnward, and (b) anti-sunward types to form large-scale magnetic flux ropes observed downstream from the strong crustal magnetic fields.	120

List of Tables

1.1	A summary of physical characteristics on terrestrial planets (ratio to Earth value). ^a	3
1.2	Overview of plasma observations of Mars	5
1.3	A summary of planetary escape velocities and energies [<i>Shizgal and Arkos, 1996</i>].	12
3.1	A summary of estimated gyro radius of picked-up O ⁺ ions before and after CIR passages.	51
4.1	A summary of ring ion observations and IMF orientation estimation.	67
5.1	A summary of an equivalent radius and a stretched length of the reconstructed magnetic flux ropes and photoelectron observation probability for Event categories A and B.	94
6.1	A summary of lower limits on the averaged magnetic flux rope spatial properties for the four types categorized according to axial orientation based on the Grad-Shafranov reconstruction (GSR) technique.	115
7.1	Summary of results obtained in this thesis.	131

Chapter 1

Introduction

1.1 General Characteristics of Mars

Mars is the fourth planet in the solar system from the Sun. It is generally known that Mars is currently a drier and colder planet compared to Earth, and it does not possess a thick atmosphere. Therefore, human inhabitation of the red planet is expected to be extremely harsh, which is why Mars is often called a ‘dead’ planet. However, previous observations have discovered a significant number of pristine and diverse surface signatures, including aeolian [e.g., *Greeley et al.*, 1992], volcanic and tectonic [e.g., *Tanaka et al.*, 1992] processes as well as punctuation by impact events and fluvial and glacial erosion networks [reviewed in e.g., *Carr*, 1996; *Jakosky and Phillips*, 2001]. It is suggested that Mars once possessed a thick atmosphere and abundant water inventory and that it had a warmer and humid climate similar to Earth [e.g., *Jakosky and Phillips*, 2001].

Table 1.1 summarizes the similarities and differences of the physical characteristics among Mars, Earth, and Venus. Mars is the second smallest among the terrestrial planets; consequently, its gravitational acceleration is approximately one-third that of Earth’s. The orbit of Mars is more elliptic than that of Earth, and the difference in energy input from solar irradiation is between ~ 490 (perihelion) and 720 (apohelion) W/m^2 [*Lundin et al.*, 2007].

The current atmospheric environment and climate of the terrestrial planets are

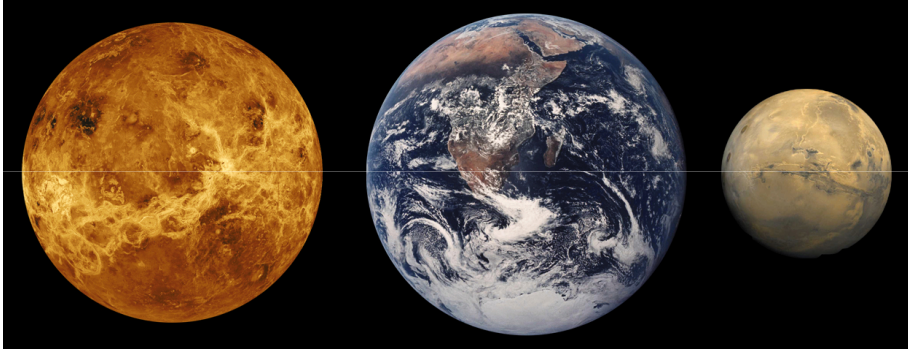


Figure 1.1: Comparison between approximate relative sizes of the terrestrial planets, from left to right: Venus, Earth, and Mars. Distances are not to scale. Courtesy of NASA.

quite different from each other. The Earth's atmosphere is mainly composed of nitrogen N_2 (79 %) and oxygen O_2 (21 %), with carbon dioxide CO_2 (~ 0.04 %) being a minor component. Earth also possesses abundant water. Mars possesses a tenuous atmosphere with a surface pressure corresponding to approximately 0.007 bars. The main constituents of the Martian atmosphere are CO_2 (95.3 %) and N_2 (2.7 %). The ratio of water vapor is only approximately 0.02 %. Conversely, Venus, which is the second planet from the Sun, has a surface pressure that is approximately 92 times higher than that of Earth, although the planetary size and gravitation force of Venus are similar to those of Earth. The surface temperature of Venus is higher than that of Earth because Venus possesses a dense CO_2 (~ 96.5 %) atmosphere with a strong resulting greenhouse effect.

Earth possesses strong global intrinsic dipole magnetic fields that forms a magnetosphere; however, Mars and Venus do not and are referred to as unmagnetized planets. The solar wind, a supersonic plasma flow released from the Sun, is filled with the interplanetary field, but it cannot easily protrude into a strong planetary magnetic field. Therefore the Earth's magnetosphere prevents the solar wind from penetrating into the near Earth. The typical stand-off distance from the Earth is approximately 10 Earth radii away in the subsolar region [e.g., *Shue et al.*, 1997]. However, unmagnetized planets, such as Mars and Venus, have no magnetic shielding, and the solar wind can deeply penetrate into and directly interact with their upper atmosphere.

Table 1.1: A summary of physical characteristics on terrestrial planets (ratio to Earth value).^a

	Venus	Earth	Mars
Mass [10^{24} kg]	4.87 (0.82)	5.97	0.642 (0.11)
Diameter [km]	12014 (0.95)	12756	6792 (0.53)
Density [kg/m^3]	5243 (0.95)	5515	3933 (0.71)
Gravity [m/s^2]	8.9 (0.91)	9.8	3.7 (0.37)
Escape velocity [km/s]	10.4 (0.93)	11.2	5.0 (0.45)
Rotation period [hours]	-5832.5 (-244) ^b	23.9	24.6 (1.03)
Distance from Sun [AU]	0.723	1	1.52
Perihelion [AU]	0.73	1	1.41
Aphelion [AU]	0.716	1	1.64
Orbital Period [days]	224.7 (0.615)	365.2	687.0 (1.88)
Axial Tilt [degrees]	177.4	23.4	25.2
Mean Temperature [$^{\circ}\text{C}$]	464	15	-65
Surface Pressure [bars]	92	1	0.01
Global Magnetic Field ?	No	Yes	No

^a <http://nssdc.gsfc.nasa.gov/planetary/factsheet/>

^b Negative numbers indicate retrograde (backwards relative to the Earth) rotation.

Therefore, atmospheric escape is caused by direct interaction with the solar wind in unmagnetized planets.

Under the assumption that all terrestrial planets have the same chemical origin, the current atmospheric and climatic differences may be related to evolutionary processes [e.g., *Lundin et al.*, 2007], which is why atmospheric escape is expected to be a key controlling factor in the planetary evolution that caused the present differences.

1.2 Plasma Environment around Mars

Numerous in-situ spacecraft missions over the past 50 years have been devoted to investigating Mars. However, we still do not have a completed survey of the particles, fields, and waves in the Martian near-space. Table 1.2 shows an overview of the

plasma and fields measurements of Mars collected since the initial investigations of Mars. As observed from Table 1.2, despite an impressive number of missions carrying plasma and field instruments, limited comprehensive plasma investigations have been conducted. Although the Phobos-2 mission carried a full set of plasma instruments, it had limited operational time (approximately 2 months), an unsuitable higher orbit, and experiments that were not fully functional. The Mars Global Surveyor (MGS) lacks an ion measurement, whereas Mars Express (MEX) did not have a magnetometer on board. However, though the measurement is limited, the plasma investigation on MEX is an important step for overall advances in the field of solar wind interaction. The latest mission to Mars is known as MAVEN (Mars Atmosphere and Volatile Evolution); it was successfully launched on November 18, 2013, with the goal of conducting comprehensive plasma and field measurements around the Martian plasma and atmospheric environment.

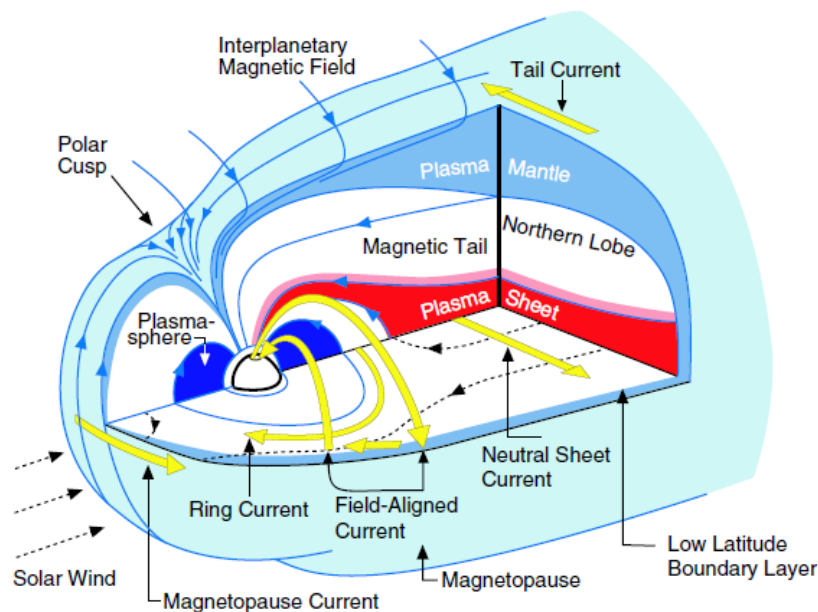


Figure 1.2: Three-dimensional cutaway view of the Earth's magnetosphere. The light blue outer surface is the magnetopause, and its boundary layers are shown in lighter blue. Magnetic field lines are shown in blue, electric currents in yellow. The polar region where the magnetic field lines converge is the polar cusp. The bow shock has been omitted for clarity. (Adapted from *Kivelson and Russell [1995]*).

Table 1.2: Overview of plasma observations of Mars (reproduced of *Barabash and Lundin [2006]*)

Mission (launch)	B field	E field Waves	e^-	Ion ^a	Ion species	Thermal plasma	Neutral atoms	Comment/results
Mariner 4 (1964)	o	x	x	o	x	x	x	Plasma probe faild
Mars probes (1971-1973)	o	x	o	o	x	x	x	Basic idea on the type of interaction
Viking 1/2 (1975)	x	x	x	x	x	o	x	Ionospheric profile during entry and descent
Phobos 1 (1988)	o	o	o	o	o	o	x	Mission was failed.
Phobos 2 (1988)	o	o ^b	o	o	o	o	x	Limited (2 months) operation
Mars Observer 1 (1992)	o	x	o	x	x	x	x	Mission was failed.
Mars-96 (1996)	o	o	o	o	o	x	o	Mission was failed.
Nozomi (1998)	o	o	o	o	o	o	x	Mission was failed.
MGS (1996)	o	x	o	x	x	x	x	400 km circular orbit
Mars Express (2003)	x	Δ^c	o	o	o	x	o	Limited operation in the eclipse
Phobos-Grunt / Yinghuo 1 (2011)	o	x	o	o	o	x	x	First Chinese mission, but Mission was failed.
Mangalyaan (2013)	x	x	x	x	x	x	Δ	First Indian mission. Now cruising.
MAVEN (2013)	o	Δ	o	o	o	o	o	Comprehensive plasma & field instruments. Now cruising.

^a Hot plasma, solar wind, particle energy > a few eV.

^b Only E-component.

^c Mainly operated the sounding mode.

As mentioned in Section 1.1, Mars does not possess a global intrinsic magnetic field [Acuña *et al.*, 1998, 1999]. The solar wind can directly interact with the Martian upper atmosphere because of the lack of magnetic shielding, so the Martian plasma environment is quite different from that of Earth [e.g., Brain, 2006; Lundin *et al.*, 2007].

Figure 1.2 illustrates a general three-dimensional sketch of the Earth’s magnetosphere inferred from spacecraft observations, and the main features of the Martian global plasma environment are summarized in cartoon form in Figure 1.3. Varieties of different plasma regimes and boundaries are formed as a result of the interaction between the solar wind and Martian upper atmosphere and can be distinguished using spacecraft particle and field measurements. The solar wind transitions from supersonic to subsonic as it crosses the bow shock into the hotter, denser, more turbulent magnetosheath, which is a similar feature to that of Earth. A boundary where few solar wind protons are observed downstream that result from the presence of the Earth’s magnetosphere is referred to as the magnetopause. Mars also has a boundary similar to the magnetopause in Earth, but Mars does not have a magnetosphere because the interplanetary magnetic field (IMF) embedded in the solar wind is draped and deposited to the planet, which forms an induced magnetosphere. This Martian boundary is often referred as the magnetic pileup boundary (MPB) or induced magnetosphere boundary (IMB). Hereafter, we refer to this boundary as the MPB. Below the MPB, the photoelectron boundary (PEB) separates the planetary ionosphere from the magnetic pileup region (MPR).

In the 1970’s, two Viking landers performed the only in-situ comprehensive measurements of the upper atmosphere of Mars with a neutral mass spectrometer and retarding potential analyzer (RPA) [e.g., Hanson *et al.*, 1977]. Remote observations by thousands of radio occultations have been performed by MGS and MEX over the last decade [e.g., Withers, 2009, and reference therein]. In addition, an ionospheric sounding was performed by the MARSIS experiment on board MEX [e.g., Gurnett *et al.*, 2008]. The Viking landers measured the altitude profiles of the neutral particle and ion densities, which are shown in Figure 1.4, together with the modeled values from Fox [2009]. It is remarkable to note that while CO₂ is the dominant neutral

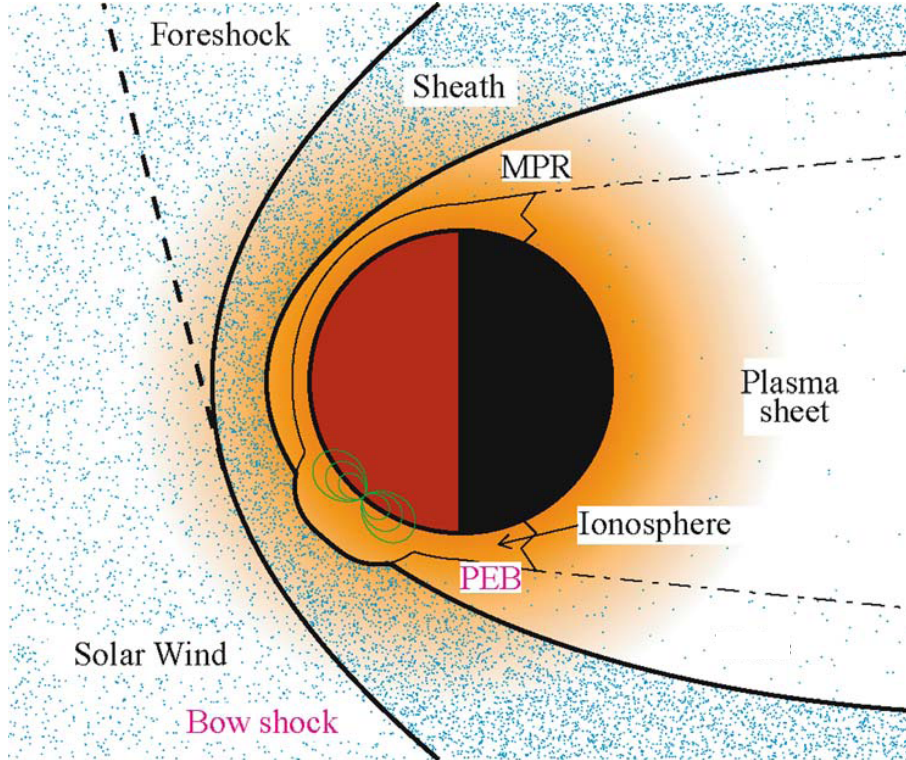
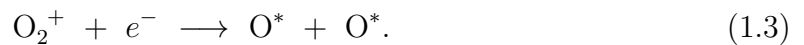
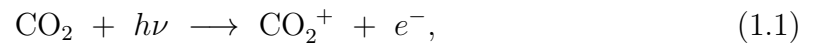


Figure 1.3: A schematic illustration of the global Martian plasma environment [Brain, 2006]. Orange shading indicates density of planetary neutrals. Blue indicates relative density of solar wind ions in different plasma regions (labeled in black), separated by different plasma boundaries (labeled in magenta). Boundary names in this figure are those specific to MGS literature.

species, the most abundant ion species in the Martian ionosphere is O_2^+ , whose peak density in the ionosphere reaches approximately 10^5 cm^{-3} at an altitude of about 120 km, as shown in Figures 1.4c and 1.4d, and results from the following important photochemical reactions driven in the Martian ionosphere:



This reaction of Equation (1.3) is referred to as the dissociative recombination and is the main atmospheric escape process for neutral oxygen atoms, as described in Subsection 1.3.2. This dissociative recombination reaction in the Martian ionosphere

provides the hot oxygen corona into a higher altitude at approximately > 200 km, which is the main reason that there are significant densities of oxygen at high altitudes compared with densities of CO_2 , which is the main species in the lower altitude at approximately < 200 km.

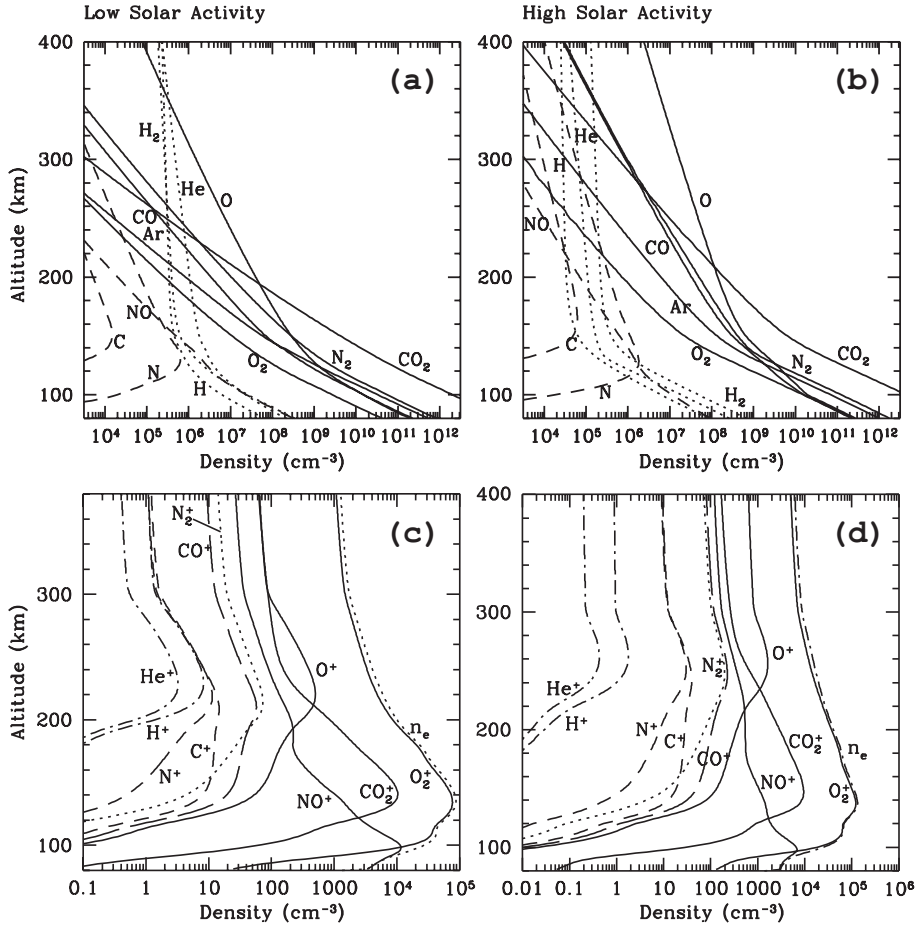


Figure 1.4: Altitude distributions of density of the Martian upper neutral atmosphere and ionosphere modeled by *Fox* [2009] at both solar activities using the data of two Viking landers [e.g., *Hanson et al.*, 1977], assuming that there is no upward flux escaping from Mars: (a) Neutral particles at low solar activity, (b) Neutral particles at high solar activity, (c) Major ion species at low solar activity, (d) Major ion species at high solar activity.

A magnetic field measurement conducted by the MGS has indicated that Mars is not totally unmagnetized. The MGS found that the localized crustal magnetic fields are primarily in the Martian southern hemisphere [e.g., *Acuña et al.*, 1998; *Connerney*

et al., 2005]. This is a remarkable feature of the Martian plasma environment compared to that of Earth and Venus. The maximum crustal magnetic field strength is ~ 250 nT at the MGS altitude (~ 400 km), which indicates that it might be approximately 1,500 nT at the surface (c.f., the Earth’s surface is typically $2.5\text{--}6.5 \times 10^4$ nT, whereas the IMF embedded in the solar wind is typically a few nT and sometimes up to several tens of nT). Figure 1.5 shows a global map of the Martian crustal magnetic fields [Connerney *et al.*, 2005]. The strongest magnetic field supplies sufficient magnetic field pressure to stand off the solar wind well above the ionosphere in certain locations. In addition, such spatially asymmetric crustal magnetic fields can interact with the IMF draping around Mars to form complex magnetic topologies. The magnetic reconnection can thus be caused [Krymskii *et al.*, 2002], or a “minimagnetosphere” may exist [Mitchell *et al.*, 2001; Lundin *et al.*, 2011a] in the vicinity of the crustal magnetic fields (Section 1.5).

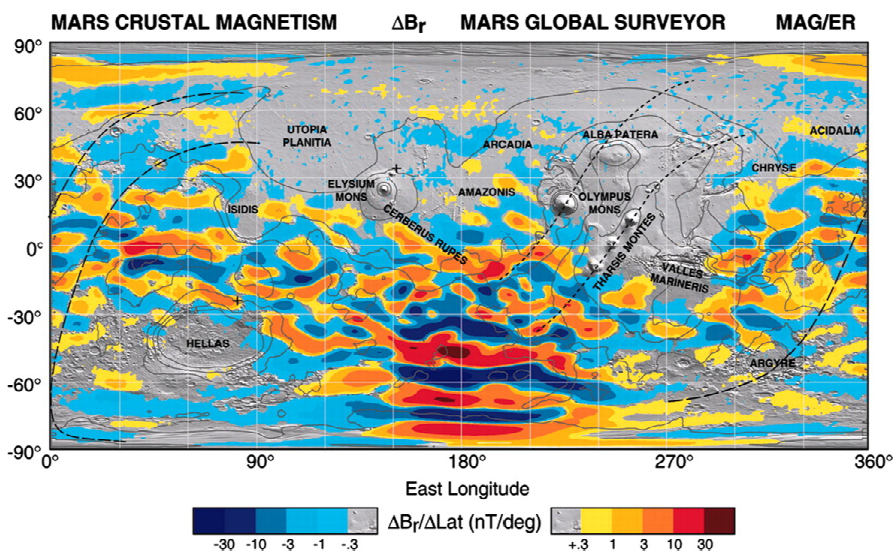


Figure 1.5: A map of the global distribution of the Martian crustal magnetic field [Connerney *et al.*, 2005]. The color code shows the median radial magnetic field component at 400 km from the Martian surface obtained by the MGS measurements in each $1^\circ \times 1^\circ$ latitude/longitude bin.

1.3 Atmospheric Escape Processes from Unmagnetized Planet

The absence of the magnetic field protection has been theoretically suggested to cause an atmospheric escape based on the solar wind interaction with unmagnetized planets such as Mars and Venus. Atmospheric escape processes are mainly divided into two processes: thermal escape and nonthermal escape. Most nonthermal escape processes are based on the existence of photoionization processes, whereas thermal escape processes are not. Figure 1.6 summarizes the nonthermal escape processes in cartoon form. In this section, we briefly review these atmospheric escape processes from unmagnetized planets.

(1) Thermal escape

- Jeans escape
- Hydrodynamic escape

(2) Nonthermal escape

- Dissociative recombination (DR)
- Ion pickup
- Ion Sputtering
- Ionospheric outflow

1.3.1 Thermal Escape

There are two thermal escape processes from an atmosphere: Jeans escape and hydrodynamic escape. Jeans escape is determined from a Maxwellian (thermalized) particle distribution. The escape rate is given by the temperature and the escape velocity at the exobase, which is the altitude at which the mean free path of the atmosphere is approximately equal to the density scale height. Theoretically, if thermal velocity is faster than the escape velocity, the thermal particles will escape. This process is caused by EUV and XUV heating at their upper atmosphere.

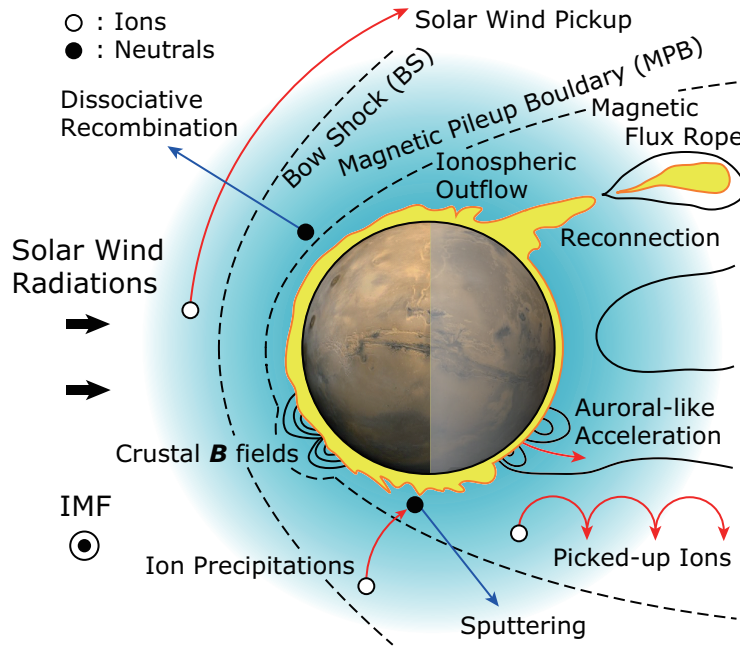


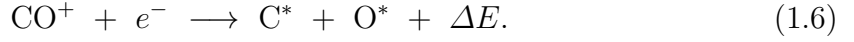
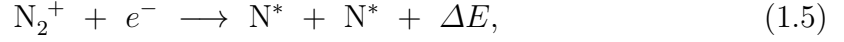
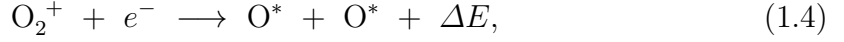
Figure 1.6: The summary sketch of the nonthermal escape processes from Mars.

Hydrodynamic escape consists of a bulk expansion of the upper atmosphere resulting from intense solar EUV/XUV fluxes that allow atoms to overcome the gravitational binding force. Hydrodynamic escape plays an important role in low-gravity environments (e.g., comets), but it is also considered to have played a major role in the Martian atmosphere during the beginning of the solar system [e.g., *Chassefière and Leblanc, 2004*]. Thermal escape processes, including Jeans escape and hydrodynamic escape, are responsible for the escape of light atoms, such as hydrogen (H) because it is easy for lighter atoms to escape from the planet.

1.3.2 Dissociative Recombination (DR)

Dissociative recombination (DR) is the escape process that leads to the Martian neutral atoms. The Martian neutral atoms near the exobase are mainly ionized via the solar UV photochemical reactions [e.g., *Shizgal and Arkos, 1996*]. Newly born ions immediately recombine ambient electrons, and as a result, they subsequently form energetic neutral atoms (ENA). An example of the Martian DR processes is as

follows:



Such reactions produce excess kinetic energy (ΔE), which results from the released ion-electron binding energy that can be larger than the escape energy of the produced atoms (e.g., 1.9 eV at the Martian exobase for O, 1.72 eV for N and 1.48 eV for C). Equation (1.4) is relative to the production of hot O atoms and is the main process involved in the loss of neutral oxygen to space. As shown in Section 1.2, Equation (1.4) also contributes to the hot O corona of Mars.

Table 1.3: A summary of planetary escape velocities and energies [*Shizgal and Arkos, 1996*].

Planet	r_c , km	v_{esc} , km/s	E_{esc}^H , eV	E_{esc}^O , eV
Earth	500	10.8	0.61	9.69
Venus	200	10.2	0.54	8.64
Mars	250	4.8	0.12	1.91

1.3.3 Ion Pickup

Ion pickup is a direct escape mechanism that is caused by the protrusion of the solar wind motional electric field into a planetary ionosphere. The Martian neutral atmosphere is ionized by photoionization, by impact with solar wind electrons or the charge exchange with solar wind ions [e.g., *Shizgal and Arkos, 1996*]. The product ions can be immediately captured in the IMF of the solar wind, and swept away from the planet and/or the accelerated convective electric field \mathbf{E} such that the combined solar wind electric and magnetic field ($\mathbf{E} \times \mathbf{B}$) results in a cycloid motion of energized ionospheric ions. Therefore the ion pickup is associated with the loss of planetary heavy ions.

Previous in-situ spacecraft observations conducted by Phobos-2 at the solar maximum and data from the MEX orbiter retrieved primarily during the solar minimum phase have detected a large outflow of heavy planetary ions such as O^+ [e.g., *Lundin et al.*, 1989, 2004; *Barabash et al.*, 2007a; *Lundin et al.*, 2008a, and many publications]. These escaping ions were expected to result mainly from ion pickup because of the mass loading of the solar wind in the Martian boundary layer. Picked-up ions are generally subject to the forces driving the planetary plasma into motion that arise because of the convective electric field. This convective electric field is induced by the interaction between the solar wind and the magnetic field tension of the draped IMF. Therefore, the escape resulting from ion pickup is strongly distributed in an asymmetrical fashion between the convective electric field hemispheres. The asymmetrical distribution associated with the ion pickup because of the acceleration of the convective electric field has been reported by both spacecraft observations [e.g., *Barabash et al.*, 2007a; *Dubinin et al.*, 2008] and numerical simulations [e.g., *Modolo et al.*, 2005; *Böfswetter et al.*, 2004]. In addition, both Phobos-2 and MEX measured picked-up protons around the Martian bow shock [*Barabash et al.*, 1991; *Dubinin et al.*, 2006; *Yamauchi et al.*, 2006, 2008]. These picked-up ions are gyrating in the plane perpendicular to the IMF and they are observed as a ring-like distribution in the velocity phase space. Computer simulations have also estimated the escape rate of ion pickup from Mars, and most of the estimations of picked-up ion escape are on the order of several 10^{24} s^{-1} for O^+ . For example, *Chaufray et al.* [2007] conducted a three-dimensional hybrid simulation and predicted escape rates of ion pickup for low and high solar activities in the present epoch at 2×10^{23} and $3 \times 10^{24} \text{ s}^{-1}$, respectively. *Fang et al.* [2008] constructed a new test particle model in which more than a billion test particles were launched to more accurately resolve the Martian picked-up ion distribution in the velocity phase space. As a result, the predicted total escape rate of ion pickup was $3.7 \times 10^{24} \text{ s}^{-1}$.

1.3.4 Ion Sputtering

Some of the ions picked up by the solar wind can precipitate into the Martian upper atmosphere, and the precipitate ions can transfer sufficient energy to escape to the local neutral atmospheric particles through subsequent collisions. This process has been referred to as ion sputtering and is related to the escape of the neutral atoms.

Observational signatures inferred that the sputtering process is quite rare, whereas the presence of the escape resulting from the sputtering has been suggested by a number of numerical simulations [e.g., *Luhmann and Kozyra*, 1991; *Luhmann et al.*, 1992; *Leblanc and Johnson*, 2001, 2002; *Chaufray et al.*, 2007]. For instance, *Luhmann and Kozyra* [1991] modeled the fluxes and energy spatial distributions of picked-up planetary O^+ incident on the dayside atmosphere of Mars and Venus, and found the spatial asymmetry of the precipitating ions resulting from the convective electric field. *Luhmann et al.* [1992] suggested that up to 90 % of the picked-up ion number flux can reimpact to the Martian upper atmosphere. In principle, the sputtering is non-selective and can escape all particles that are present at the Martian exobase, including C, O, N, N_2 , CO, O_2 , and CO_2 [*Leblanc and Johnson*, 2002]. This feature is different from the dissociative recombination. *Johnson and Luhmann* [1998] suggested that the energetic O produced by ion sputtering can be added to the Martian oxygen corona, which initiates a feedback process that can enhance the atmospheric sputtering rate. The escape rate from ion sputtering has been estimated to be approximately $7.0 \times 10^{23} \text{ s}^{-1}$ [*Luhmann et al.*, 1992], with a more recent estimation of $2.0 \times 10^{23} \text{ s}^{-1}$ [*Chaufray et al.*, 2007] at the solar minimum. These escape rates are much smaller than those of the other nonthermal escape processes. However, several numerical simulations [e.g., *Luhmann et al.*, 1992; *Leblanc and Johnson*, 2001, 2002] have indicated the importance of ion sputtering in a primitive Mars atmosphere because of the drastic and extreme solar wind and/or solar EUV fluxes. Conversely, a three-dimensional multi-species magneto-hydrodynamic (MHD) simulation by *Terada et al.* [2009] indicated that a strong magnetic field was induced in the entire dayside ionosphere and resulted from an interaction between extreme solar wind and the Martian upper atmosphere. This strongly induced magnetic field could effectively protect the upper atmosphere from

sputtering escape. Hence, the contribution of ion sputtering escape in ancient Mars is not quantitatively understood.

1.3.5 Ionospheric Outflow

Ionospheric outflow is the plasma energization and escape process that is driven by direct solar wind forcing below the ionopause. Planetary ions receive energy and momentum from the solar wind, and ions escape from Mars. Several spacecraft observations (e.g., Phobos-2 and MEX for Mars, and the Pioneer Venus Orbiter (PVO) and Venus Express (VEX) for Venus) have clarified that planetary ions also escape from Mars and Venus into their plasma tails [e.g., *Lundin et al.*, 1991, 2008a, 2009; *Barabash et al.*, 2007b]. According to *Pèrez-de-Tejada* [1987]; *Pèrez-de-Tejada* [1998], the conservation of energy and momentum in the transfer of energy and momentum flux for the solar wind (Φ_{SW}) and planetary ions (Φ_P) can theoretically produced the following:

$$\Phi_P = \frac{v_{SW} \cdot m_{SW}}{v_P \cdot m_P} \left(\Phi_{SW} - \frac{v_{i,SW}}{v_{SW}} \Phi_{i,SW} \right) \cdot \frac{\delta_{SW}}{\delta_P}, \quad (1.7)$$

where m_{SW} and v_{SW} are the solar wind mass and velocity, respectively, m_P and v_P in the planetary ion mass and velocity, respectively, and $\Phi_{i,SW}$ and $v_{i,SW}$ are the local-decelerated solar wind flux and velocity, respectively. The ratio δ_{SW}/δ_P defines the relative momentum exchange thickness. Equation (1.7) indicates that the planetary ion flux is strongly dependent on the velocity (v_P) and mass (m_P) of the escaping ions. Equation (1.7) also indicates that the ratio between the solar wind velocity and planetary ions (v_{SW}/v_P) provides a flux amplification for ions of equal masses. However, because of the restriction of observations, the physical mechanisms how to transfer energy and momentum of the solar wind to planetary ions are under debate. Therefore, ionospheric outflow is less understood than are the other escape processes. Possible candidates of a physical mechanism to drive ionospheric outflow are plasma waves [e.g., *Ergun et al.*, 2006; *Lundin et al.*, 2011b; *Halekas et al.*, 2011], viscous-type plasma instabilities (such as Kelvin-Helmholtz (KH) instability [e.g, *Penz et al.*, 2004; *Terada et al.*, 2002, 2009]), and/or magnetic reconnection [e.g., *Eastwood et al.*, 2008;

Halekas et al., 2009] (as described in Section 1.5).

As a result of the magnetic reconnection between interplanetary magnetic field lines (or crustal field lines for Mars), magnetic flux ropes (sometimes called plasma clouds) can be formed [e.g., *Russell and Elphic*, 1979; *Vignes et al.*, 2004]. Magnetic flux ropes are generally known to be twisted magnetic field structures because the magnetic field near the center of the flux rope is strong and aligned axially and becomes gradually weaker and more azimuthally aligned with distance from the center, as shown in Figure 1.7 [*Russell and Elphic*, 1979]. Magnetic flux ropes have been observed throughout the solar system, even in the unmagnetized planets, such as Venus and Mars [e.g., *Russell and Elphic*, 1979; *Vignes et al.*, 2004]. The characteristics of the magnetic flux ropes observed in the unmagnetized planets have been extensively studied by the Pioneer Venus Orbiter (PVO), which conducted observations on Venus [e.g., *Luhmann and Cravens*, 1991, and references therein]. These magnetic flux ropes can also be a candidate for the solar wind intrusion into the lower altitude, and their formation can result from interplanetary magnetic field lines draping around the ionosphere and intruding into the ionosphere, where they are twisted and distorted by KH or shear instabilities at the ionopause as they sink [e.g., *Wolff et al.*, 1980; *Luhmann and Cravens*, 1991]. However, the definite penetration of interplanetary magnetic field lines through the ionopause has been under debate. The flux ropes associated with the Martian crustal magnetic fields are detailed in Section 1.5.

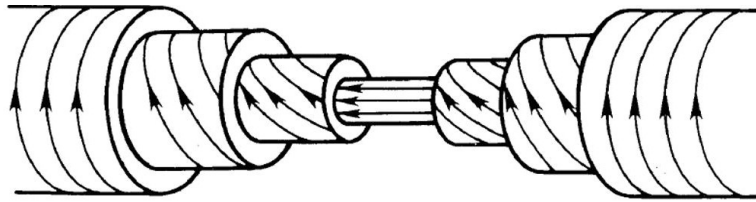


Figure 1.7: Schematic illustration of interior magnetic field configurations of a flux rope. Reproduced from *Russell and Elphic* [1979].

Recently, *Lundin et al.* [2008a] reported that cold ion outflow from the Martian ionosphere with energies less than 200 eV can significantly contribute to atmospheric escape from Mars. Such low-energy ions originating in the Martian ionosphere were

observed to be expanding symmetrically into the tail in a cometary manner. In particular, *Lundin et al.* [2009] demonstrated that cold ion escape with energies of approximately 10 eV, which is slightly above the escape energy of Mars, can be a dominant ion escape process in the present epoch. Figure 1.8 shows a typical cold ionospheric ion escape event observed by MEX [*Lundin et al.*, 2009]. Because MEX does not operate any spacecraft potential control, they adopted a spacecraft potential of -9 V. It should be noted that this value was confirmed to be typically reasonable for use in their statistical analyses [*Lundin et al.*, 2009]. It is clearly shown that cold dayside ionospheric ions are gradually energized toward the nightside at between 08:30 and 08:40 UT as shown in Figure 1.8 [*Lundin et al.*, 2009]. Moreover, *Fränz et al.* [2010] reported new measurements of the transterminator outflow from the Martian ionosphere using the ASPERA-3 plasma and MARSIS radar instruments on board MEX for the certain orbit. The ionospheric pressure gradient between dayside and nightside or the momentum transfer from the solar wind has been suggested to cause the transterminator outflow, which has been detected by PVO at the terminator above the ionosphere of Venus [*Knudsen et al.*, 1980, 1982]. If the transterminator outflow is symmetrically observed around the terminator, escape rates can reach approximately $1.5 \pm 0.5 \times 10^{25} \text{ s}^{-1}$, which could explain a significant part of the ion escape from the Martian upper atmosphere [*Fränz et al.*, 2010].

1.4 Role of Solar Wind Variations in Atmospheric Escape

As mentioned in Section 1.3, outflows of planetary ions from the Martian upper atmosphere based on plasma observations by the Phobos-2 and MEX missions have been reported [e.g., *Lundin et al.*, 1989, 2004; *Carlsson et al.*, 2006; *Barabash et al.*, 2007a]. Phobos-2 observations were conducted during a high solar activity period, and measurements of escaping ions by Phobos-2 led to an estimated O^+ loss rate of $2\text{-}3 \times 10^{25} \text{ s}^{-1}$, with energies from 0.5 eV to 24 keV [*Lundin et al.*, 1989]. Moreover, this total ion escape rate has recently been confirmed by *Ramstad et al.* [2013] using a different

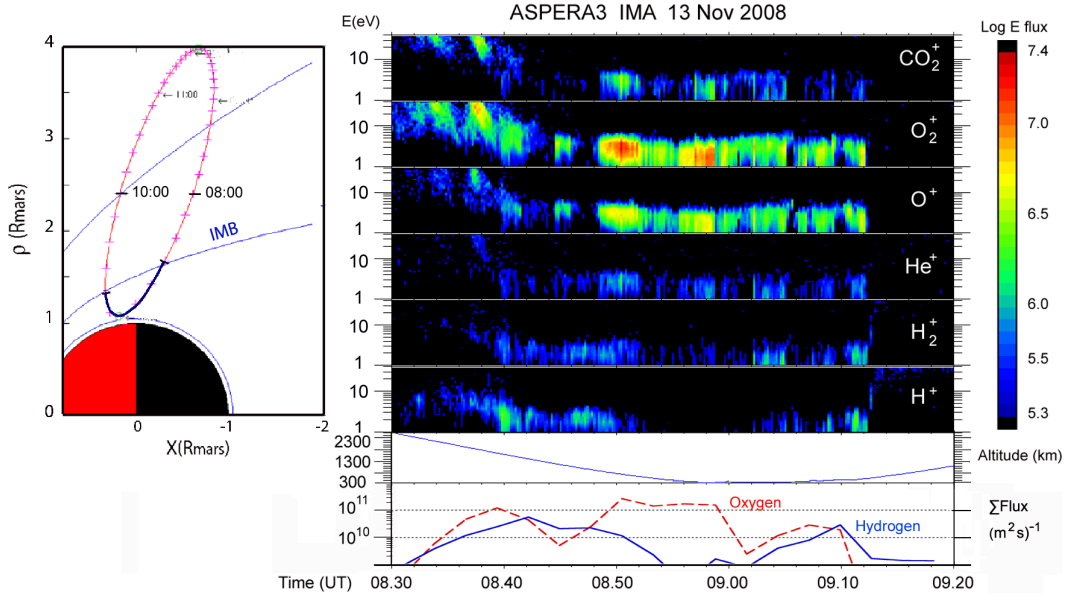


Figure 1.8: Energy-time spectrograms for cold ionospheric ion fluxes, CO_2^+ , O_2^+ , O^+ , He^+ , H_2^+ , and H^+ , around a periapsis crossing on November 13, 2008. Color code represents ion energy fluxes with unit of $\text{keV}/(\text{cm}^2 \text{ sec sr keV})$. The bottom plot shows ion escape fluxes of oxygen (O_2^+ , O^+) and hydrogen (H_2^+ , H^+) group ions with energies $< 50 \text{ eV}$. The MEX orbital projection in a cylindrical coordinate system, and the corresponding time interval, is displayed in the plot to the left. Adapted from *Lundin et al. [2009]*.

methodology from that used by *Lundin et al. [1989]*. Surprisingly, the outflow rate derived from the Phobos-2 measurement nearly corresponds to the amount of time it would take to evacuate all of the CO_2 ($< 10^8$ years), which is the main constituent in the present Martian atmosphere. However, the Phobos-2 observations were only conducted for approximately 2 months: therefore, the validity of the estimated outflow rate has been under debate. However, the global average escape rates of planetary ions derived from the MEX observations during a low solar activity period are much lower, with the escape rates of O^+ , O_2^+ , and CO_2^+ estimated to be 1.6×10^{23} , $1.5 \times 10^{23} \text{ s}^{-1}$, and $8.0 \times 10^{22} \text{ s}^{-1}$, respectively, and with energies from 30 eV to 30 keV, as shown in Figure 1.9 [*Barabash et al., 2007a*]. After June 2007, MEX was able to observe low-energy ions ($\sim 10 \text{ eV}$) because a new energy table for the ion sensor was uploaded. *Lundin et al. [2008a]* estimated the heavy-ion escape rate at $3.3 \times$

10^{24} s^{-1} with energies from 10 eV to 20 keV. These previous studies suggest that the estimated total ion escape fluxes vary by a factor of ~ 10 at least between the solar minimum and maximum periods. However, it is poorly understood which energized and escaping processes mentioned in Section 1.3 are quantitatively responsible for the observed difference under the various solar wind conditions.

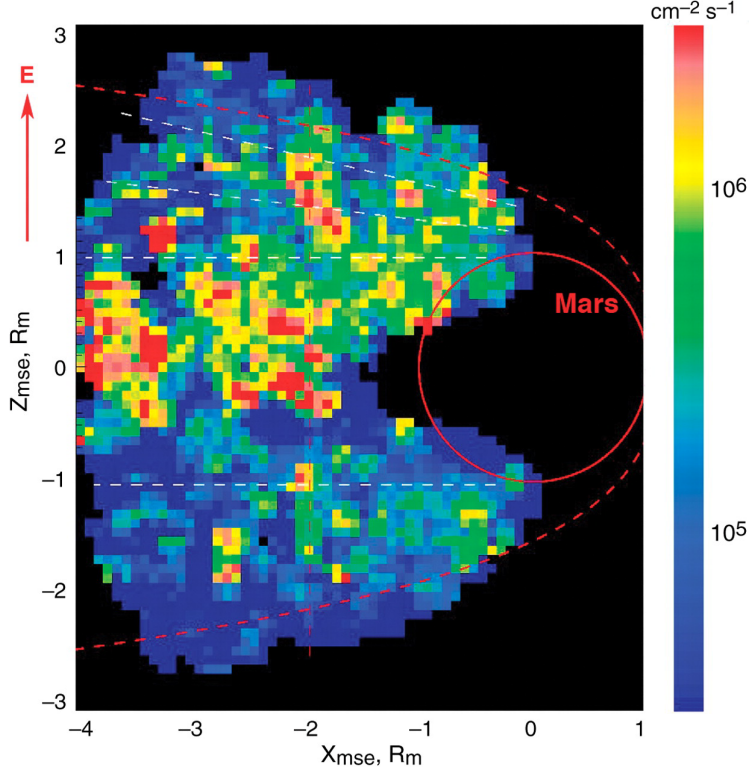


Figure 1.9: A map of the integral fluxes measured by the MEX ASPERA-3 IMA sensor for all heavy three ions (O^+ , O_2^+ , CO_2^+) together averaged over the range $-0.8 R_M < Y < 0.8 R_M$ in the $z - x$ plane in a coordinate system relative to the direction of the convective electric field [Barabash *et al.*, 2007a].

Computer simulations have also been utilized to determine the interaction of the solar wind with the Martian upper atmosphere. A number of numerical simulation models, including MHD, multi-fluid, hybrid, and combinations of MHD and test-particle simulations [e.g., Ma *et al.*, 2004; Terada *et al.*, 2009; Chaufray *et al.*, 2007; Fang *et al.*, 2008], have been used to estimate escape fluxes for several solar-wind-induced processes such as ion pickup, sputtering, and viscous interaction under several

solar wind conditions. For example, *Brain et al.* [2010b] reviewed numerical models of the global plasma environment around Mars and compared the results from different Martian global plasma interaction models under the same solar wind conditions. However, most of the previous modeling studies investigated typical solar wind conditions on Mars, and the response of each escape process to dynamic solar wind changes, such as interplanetary shock arrival, is still far from understood.

Observations conducted by MEX have provided the first in-situ Martian plasma data in nearly 10 years, which corresponds to approximately one solar cycle; however, MEX lacks a magnetometer. Several studies about the relationship between the atmospheric escape from Mars and the solar activities have been reported based on the MEX observations. For example, *Lundin et al.* [2008b] used data from 42 orbits of MEX over 17 months from December 2004 to June 2006, and suggested that the escape fluxes are directly connected to the variability of the solar wind. They also found that the decreases in ion outflow were associated with EUV during the declining phase of the solar cycle. *Nilsson et al.* [2010] conducted a statistical analysis to investigate the influence of solar EUV and solar wind conditions on ion escape from Mars using MEX observations combined with solar wind proxy data obtained from MGS [*Brain et al.*, 2005, 2006a] from May 2004 to November 2005. They reported that ion fluxes measured by MEX were clearly dependent on the strength of the subsolar magnetic field as inferred from the MGS measurements. Recently, *Lundin et al.* [2013] analyzed the Martian planetary heavy-ion outflow and escape from Mars by using the MEX ion observations from June 2007 to January 2013. This time periods are the rising phase of the latest solar cycle 24. They also confirm only from the MEX ion data that the average heavy ion escape rate increased by a factor of ~ 10 , from $\approx 1 \times 10^{24} \text{ s}^{-1}$ (solar minimum) to $\approx 1 \times 10^{25} \text{ s}^{-1}$ (solar maximum) [*Lundin et al.*, 2013]. Moreover, they show that average and median tail fluxes of low-energy ($< 300 \text{ eV}$) heavy ions are highly correlated with the solar activity proxies $F_{10.7}$ and the sunspot number [*Lundin et al.*, 2013].

Recently, the plasma interaction between an unmagnetized planet and interplanetary disturbances in the solar wind, such as corotating interaction regions (CIRs) or coronal mass ejections (CMEs), has been found to be important for determining the

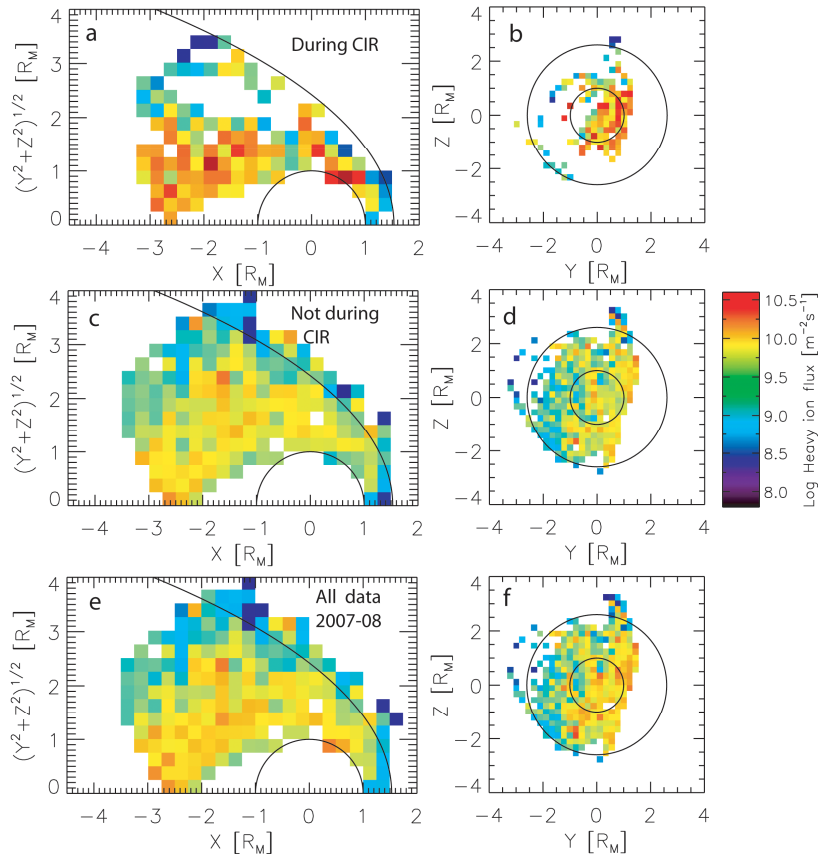


Figure 1.10: Averaged antisunward fluxes of planetary heavy ions from Mars observed by MEX/IMA (a, b) during CIR passages, whereas (c, d) during ‘normal’ solar wind conditions, and (e, f) for all data combined [Edberg *et al.*, 2010]. The measured fluxes are averaged over $0.25 \times 0.25 R_M$ bins in Mars-centered Solar Orbital (MSO) coordinates.

atmospheric escape from the unmagnetized planets. CIRs are formed at the interface of slow- and high-speed solar wind streams. When a CIR passes through a magnetized planet like Earth, it is observationally known to cause geoeffective activities, such as magnetic storms as a consequence of the interaction with the Earth’s magnetosphere [e.g., Tsurutani *et al.*, 2006; Richardson *et al.*, 2006]. CMEs are also remarkable interplanetary disturbances in the solar wind and are known to have large impacts on the geospace environment. Therefore, it is expected that interplanetary disturbances such as CIRs, CMEs, and/or associated high-energy particles may result in more drastic dynamic changes to Martian atmospheric erosion than to Earth’s [Futaana *et al.*,

2008]. In addition, Mars has a higher chance of encountering CIR shock structures than Venus because the CIRs are developed well beyond 1 AU from the Sun [e.g., *Gosling and Pizzo, 1999*].

Indeed, *Dubinín et al. [2009]* identified a scavenging of the Martian ionosphere during the passage of a CIR. The estimated increase in the escape rate was as high as a factor of ~ 10 . A statistical survey based on MEX ion observations during the solar minimum indicated that the escape rate during CIRs passage increases by a factor of ~ 2.5 for Mars [*Edberg et al., 2010; Nilsson et al., 2011*] and ~ 1.9 for Venus [*Edberg et al., 2011*] because of the pressure pulse in the solar wind, as shown in Figure 1.10. CMEs also significantly disturb the plasma environment around unmagnetized planets and can enhance the atmospheric escape rate [e.g., *Luhmann et al., 2007; Futaana et al., 2008; McEnulty et al., 2010*]. For example, *Luhmann et al. [2007]* showed the planetary ion escape enhancements on Venus related to several CMEs or ICMEs. The cause of the escape enhancement accompanied by the ICMEs could be complicated as inferred from the recent VEX observational data [*Luhmann et al., 2008*]. The studies mentioned above indicate that atmospheric escape phenomena are highly variable depending on the solar wind conditions. However, these studies focused on the change in the global average ion escape rates; thus the physical processes responsible for the enhancement of planetary heavy-ion escape resulting from the interplanetary disturbances such as CIRs and CMEs are still up for debate.

In summary, numerous previous and ongoing studies have revealed that the escape rate of planetary ions varies by an order of magnitude within a short time scale (hours or days) because of solar disturbances (e.g., CIRs or CMEs) and with the course of a solar cycle (≈ 11 years).

1.5 Role of Crustal Magnetic Fields in the Martian Plasma Environment

Although Mars lacks a global intrinsic magnetic field, it possesses strong localized crustal magnetic fields [e.g., *Acuña et al., 1998, 1999*] as shown in Section 1.2. Because

the IMF embedded in the shocked solar wind interacts with the Martian crustal magnetic fields, the electromagnetic environment around Mars is known to be highly complicated and dynamic. It has been reported that crustal magnetic fields influence the Martian upper atmosphere and plasma interaction region on local scales and perhaps on global scales [Brain, 2006].

Based on spacecraft measurements and numerical simulations, the Martian crustal magnetic fields may provide additional atmospheric escape channels in several different ways. For example, ionospheric plasma can be removed via aurora-like plasma acceleration in the vicinity of the open field line areas above the crustal magnetic fields, which is analogous to the cusp regions of Earth’s magnetosphere [e.g., Brain *et al.*, 2006b; Lundin *et al.*, 2006a,b; Nilsson *et al.*, 2006]. Figure 1.11 represents the ion end electron energy-time spectrograms observed by MEX around the regions of the open crustal magnetic field lines (“cusps”) [Lundin *et al.*, 2006b], wherein narrow beams of planetary heavy ions are flowing upward/tailward and substantial electrons are moving in the opposite direction (downward/sunward) [e.g., Lundin *et al.*, 2006a,b]. Therefore, this signature observed by MEX is evidence of a field-aligned plasma acceleration, which suggests the existence of a parallel electric field acceleration as illustrated in Figure 1.12. In the Phobos-2 measurements, Lundin *et al.* [1989] identified a cold ion outflow and energetic ions with energies reaching keV because of the aurora-like acceleration in the Martian wake region. Using MEX/SPICAM ultraviolet and near-infrared spectrometers, Bertaux *et al.* [2005] identified auroral processes that operate on Mars by depositing energy and particles into the nightside atmosphere, which should alter in certain locations.

The current sheet structures characterized by the B_x reversal (the x direction is parallel to the Mars-Sun line) observed near Mars might also be affected by crustal magnetic fields [e.g., Halekas *et al.*, 2006, 2008; Halekas and Brain, 2010]. Phobos-2 first detected those structures far from the planet, with a distance of approximately $2.86 R_m$ (R_m means the Martian radius) in the Martian magnetotail region [e.g., Yeroshenko *et al.*, 1990]. MGS has also frequently observed these signatures even at a relatively low altitude of approximately 400 km, as shown in Figure 1.13 [Halekas *et al.*, 2006]. Figure 1.13 indicates that an electron flux enhancement with energies

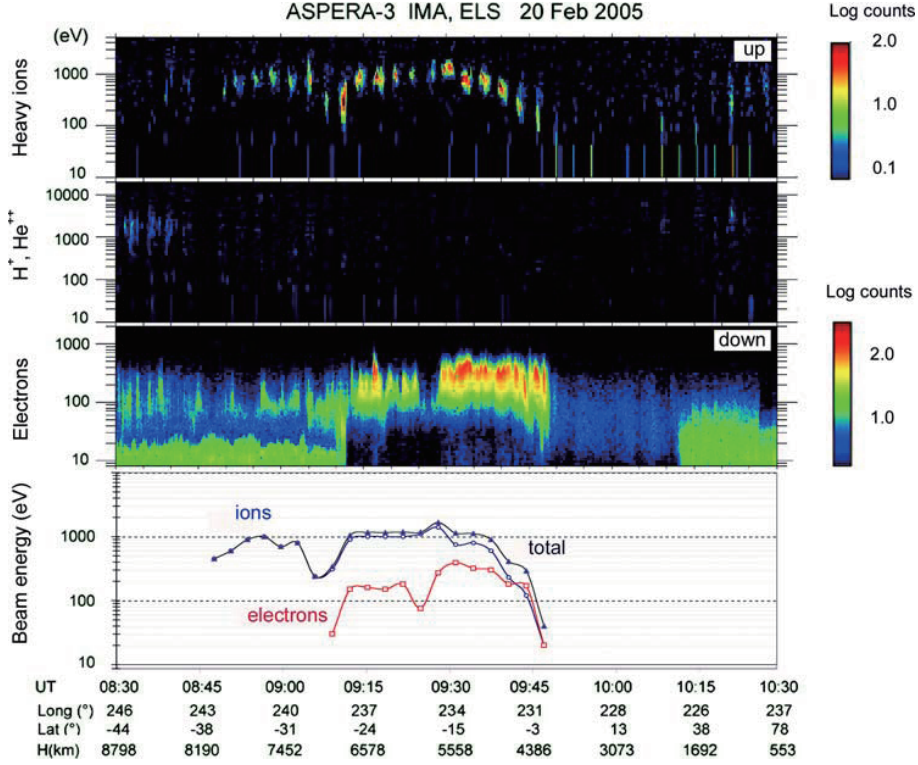


Figure 1.11: MEX/ASPERA-3 energy-time spectrograms and flux peak data for ions and electrons on February 20, 2005, when MEX traversed above the Martian crustal magnetic fields in the tail-eclipse between 09:13 and 10:12 UT. Top panel shows upward traveling planetary heavy ions, second panel is anti-sunward solar wind ions, and third panel is downward electrons, respectively. The bottom panel represents peak energy for ion (blue), electrons (red), and both in total (black). Adapted from *Lundin et al.* [2006b].

below approximately 1 keV is simultaneously observed during B_x reversal (current sheet crossing) and is analogous to terrestrial plasma sheet crossing. Because the observed current sheet has an orientation that is roughly consistent with the field configuration inferred from the draping field directions in an induced magnetosphere, its formation is thought to be controlled by upstream IMF conditions [e.g., *Yeroshenko et al.*, 1990; *Halekas et al.*, 2006]. However, *Halekas et al.* [2006] noted that the structure and location of the current sheet, particularly on the nightside, is highly variable and depends on both the solar wind variations and the relative position of the crustal magnetic fields. *Halekas and Brain* [2010] used their automated procedure

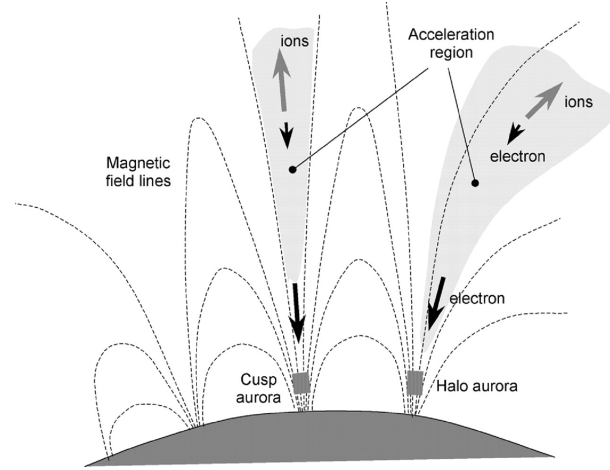


Figure 1.12: Schematic illustration of the aurora-like plasma acceleration above cusps of the Martian crustal magnetic fields. Adapted from Figure 5 of *Lundin et al.* [2006a].

to conduct a systematic statistical survey of the Martian current sheets encountered by MGS and successfully identified over 10,000 current sheet crossings during the nearly 7.5 years of the MGS mapping mission [*Halekas and Brain, 2010*]. The statistical properties of the Martian current sheet based on the results of *Halekas and Brain* [2010] can be summarized as follows: (i) The current sheet crossings are most frequently observed above the nightside and in the terminator/polar regions, which is consistent with an origin associated with the draping magnetic field; (ii) however, a significant number of current sheets were observed above the dayside, which could have resulted from the solar wind discontinuities; and (iii) crustal magnetic fields may also play a significant role in the formation of the dayside current sheet. For example, anti-parallel draping of the IMF over a crustal magnetic field could preferentially form a current sheet or a pre-existing solar wind current sheet could be compressed and amplified over a crustal magnetic field [*Halekas and Brain, 2010*].

Both Phobos-2 and MEX have recorded accelerated cold planetary heavy ions proximal to the current sheet in the Martian magnetotail [e.g., *Lundin et al., 1989; Fedorov et al., 2006, 2008*]. The magnetic tension force associated with the current sheets is thought to be responsible for the energization of planetary heavy ions, because it can accelerate ionospheric plasma away from Mars [*Dubinin et al., 1993*]. As current sheets become too thin, they are theoretically capable of causing mag-

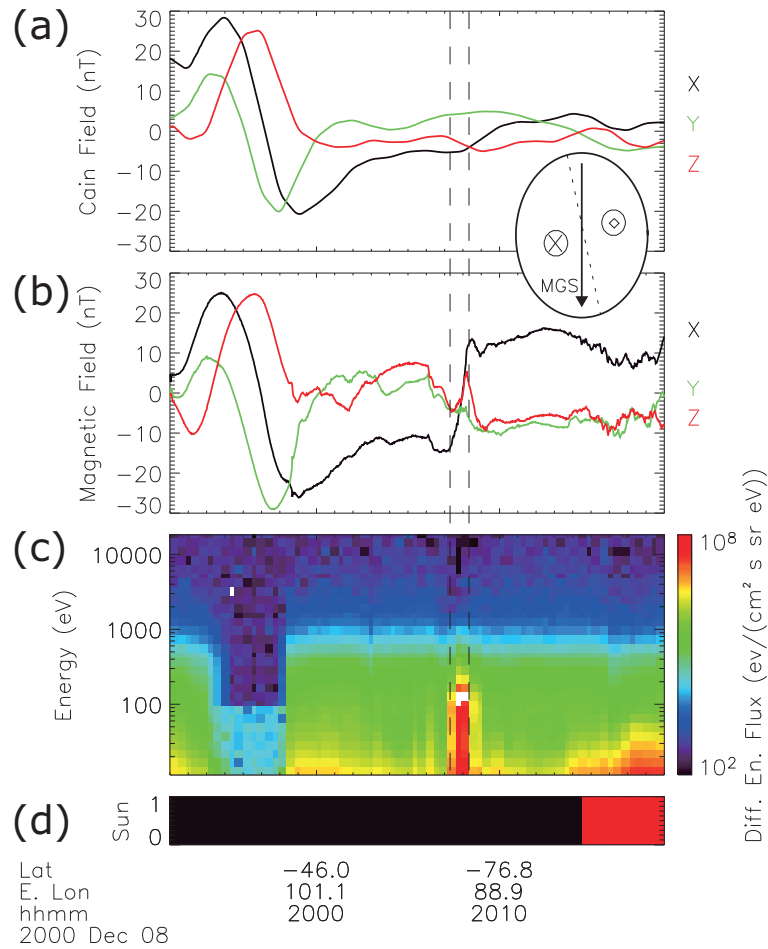


Figure 1.13: Current sheet crossing observed by MGS at 20:08 UT on December 8, 2000. Time series plots of vector magnetic field for (a) expected crustal magnetic fields modeled by *Cain et al.* [2003] and (b) MGS observations in the MSO coordinate system. (c) Energy-time spectrogram of electrons. The approximate extent of the current sheet crossing is bracketed by two vertical dashed lines. (d) Color bar indicates whether MGS was illuminated (red) or in eclipse (black). The inferred geometry, viewed from the tail is shown in the inset, the dashed line showing the current sheet, and symbols indicating magnetic field polarities. Reproduced from *Halekas et al.* [2006].

netic reconnection via a number of different methods, even in the Martian plasma environment. It is widely accepted that magnetic reconnection is capable of changing magnetic topology and transporting magnetic energy into low-altitude planetary plasma kinetic energy. Hence, magnetic reconnection between crustal magnetic fields and/or the IMF draped around the conducting the Martian ionosphere may also be responsible for ripping Martian ionospheric plasma away to space. The MGS electron and magnetic field measurements have detected Hall magnetic field signatures associated with magnetic reconnection [Eastwood *et al.*, 2008; Halekas *et al.*, 2009], but the MGS observations lacked ion measurements.

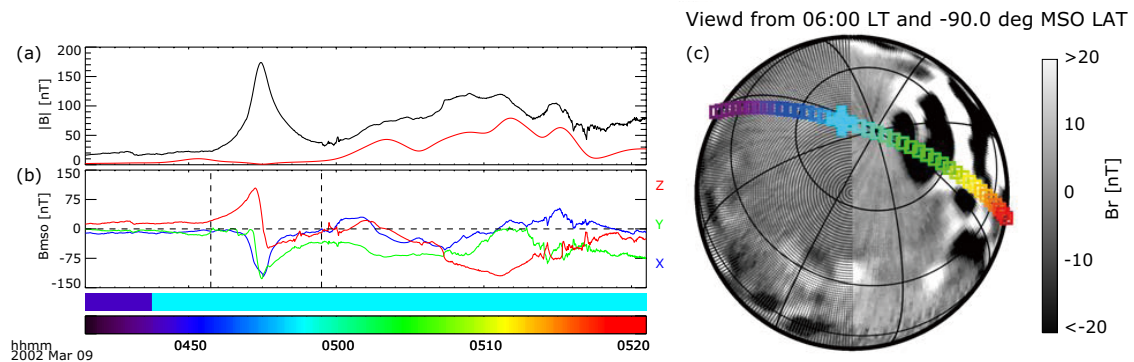


Figure 1.14: Time series plots of (a) magnetic field magnitude and (b) vector magnetic field in the Mars-centered, Solar Orbital (MSO) coordinate system observed by MGS on March 9, 2002. Expected crustal magnetic field magnitude deduced from *Cain et al.* [2003] is shown by the red solid line in Figure 1.14a. Color bars indicate whether MGS was illuminated (light blue) or in eclipse (dark blue) and observation time. MGS observed a magnetic flux rope during the time interval between two vertical dashed lines in Figure 1.14b. (c) The MGS orbital track is indicated by the squares with colors, which are corresponding to the color bar with respect to the observation time seen in the bottom of Figure 1.14b. The blue plus marks the location of the largest observed magnetic field amplitude. Grayscale background in the globe indicates the expected radial component of the crustal magnetic field, viewed from above the south pole, with the Sun to the right. Reproduced from *Brain et al.* [2010a].

Magnetic flux ropes and associated plasma clouds strongly correlated with magnetic reconnection are key phenomena thought to confine large amounts of ionospheric

plasma that can be removed from the planet [e.g., *Vignes et al.*, 2004; *Brain et al.*, 2010a; *Briggs et al.*, 2011]. The origin of their magnetic flux ropes is thought to be the IMF draping around the planets as described in Subsection 1.3.5, but *Brain et al.* [2010a] investigated the MGS observations downstream of the strong crustal magnetic fields and found a large-scale isolated magnetic flux rope associated with these fields, as shown in Figure 1.14. They proposed that the magnetic flux rope could intermittently carry significant large amounts of atmosphere away from Mars via a bulk removal process such as magnetic reconnection, with the process capable of accounting for as much as 10% of the total present-day ion escape from Mars. Thus, in-situ plasma and/or magnetic fields observations can determine the characteristic signatures of additional atmospheric escape channels associated with crustal magnetic fields.

In contrast, the global MHD simulations conducted by *Ma et al.* [2002] suggested that the crustal magnetic field can prevent the Martian ionospheric plasma from escaping to space because of the formation of ‘mini-magnetospheres’, which are observed primarily in the Martian southern hemisphere, as illustrated in Figure 1.15. The potential influence of ‘mini-magnetospheres’ was also deduced from the spacecraft in-situ plasma measurements [e.g., *Mitchell et al.*, 2001; *Lundin et al.*, 2011a]. Therefore, it is not well understood whether the crustal magnetic fields increase or decrease atmospheric escape rates relative to an ‘unmagnetized’ Mars; however, it is important to understand the role of crustal magnetic fields in atmospheric escape from Mars.

1.6 Objectives of This Thesis

As mentioned in Section 1.1, the current climate of Mars is too cold and the atmosphere too tenuous for liquid water to be sustained stably on its surface. However, there are many indications that the climate was different in ancient Mars. For example, the geological fluvial networks of certain valleys [*Carr*, 1996] indicate that Mars was once Earth-like planet that possessed an abundant CO₂ atmosphere capable of sustaining water in the liquid state for at least the first tens to hundreds of millions of years of the planet’s lifetime [e.g., *Lammer et al.*, 2003; *Chassefière and Leblanc*,

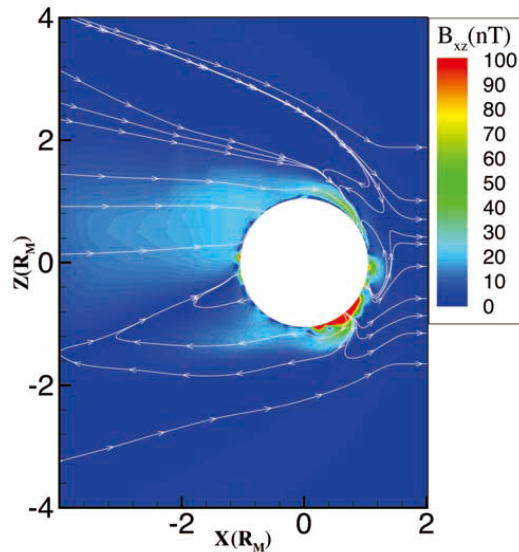


Figure 1.15: Global MHD simulation results taking into account the crustal magnetic fields in terms of the calculated magnetic field configuration in the noon-midnight meridian ($X - Z$) plane. The color represents the magnetic field amplitude: the white lines marked with arrows indicate the projected vector magnetic field direction. Reproduced from *Ma et al.* [2002].

2004, and references therein]. Therefore, the water inventory and equivalent CO_2 atmosphere that Mars initially possessed must have been removed from the Martian atmosphere.

The process that removed the water inventory and CO_2 atmosphere from the Martian atmosphere are considered to be either atmospheric escape to the interplanetary field (as discussed in Sections 1.3, 1.4), restoration into the Martian crustal soil, or both. In fact, certain water reservoirs in the Martian near surface were found by the 2001 Mars Odyssey satellite [e.g., *Feldman et al.*, 2002, 2004]. This fact indicates that all of the water vapor inventories from primordial Mars did not escape to space from the Martian surface during the formation of the present parched Martian climate. In addition, there are permanent ice cap deposits of both water inventory and CO_2 at both Martian poles [e.g., *James et al.*, 1992; *Bibring et al.*, 2004]. However, the possible amount of CO_2 deposited in the Martian soil is insufficient to completely remove CO_2 from the Martian atmosphere compared with the relevant initial CO_2

atmosphere in Mars.

Therefore, the amount of CO₂ required to cause significant greenhouse effects must have been removed from Mars to realize the present Martian climate [e.g., *Jakosky and Phillips, 2001; Lammer et al., 2013*, and references therein]. It is important to determine when, how, and what amount of the Martian atmosphere escaped throughout Martian history. To understand the above questions, the atmospheric escape processes of the present epoch must be determined along with their dependence on solar wind conditions and crustal magnetic field topologies. Therefore, the outflows of planetary ions from the Martian upper atmosphere caused by solar-wind-induced processes must be determined to understand the evolution of the Martian atmosphere [*Jakosky and Phillips, 2001*].

The main objectives of this thesis are to investigate the role of the solar wind variations and the crustal magnetic fields in the atmospheric escape from Mars, based on in-situ plasma and magnetic fields observations. In this thesis, I have analyzed in-situ plasma and magnetic field data acquired by current and previous spacecraft missions, including the Mars Express (MEX) from 2003–present for ESA and Mars Global Surveyor (MGS) from 1997–2006 for NASA. I have primarily utilized ion (MEX/IMA), electron (MEX/ELS and MGS/ER), and magnetic field (MGS/MAG) data.

In Chapter 2, I provided a general introduction and outline the instrumentation on board MGS and MEX that was used in this thesis. In Chapter 3, I focus on the role of the solar wind variations in atmospheric escape from Mars based on the MEX observations, and in particular, I study the solar wind dependence on planetary heavy-ion precipitation phenomena, which can potentially cause ion sputtering, as described in Subsection 1.3.4. The characteristic planetary heavy-ion signatures observed in the vicinity of the Martian ionosphere are also reported. These events are mostly accompanied by passages of CIRs, which is one of the characteristic recurrent solar wind conditions. The solar wind conditions (in particular, velocity) that arrive at Mars are deduced from the MEX ion data and compared with the ACE solar wind data, considering the travel time from Earth to Mars.

In Chapter 4, I statistically probe the role of the solar wind motional electric fields on planetary heavy-ion precipitation onto the Martian ionosphere, which is result of

the behavior of planetary heavy ions precipitating toward the Martian ionosphere that are strictly controlled by the solar wind electric field direction \mathbf{E} , which is determined by $\mathbf{E} \equiv -\mathbf{V}_{\text{sw}} \times \mathbf{B}$, where \mathbf{V}_{sw} is the solar wind bulk velocity and \mathbf{B} is the interplanetary magnetic field (IMF) direction. However, the IMF orientation cannot be directly obtained because MEX does not possess any magnetic field detectors; therefore, a semi-automated method is developed to estimate the IMF orientation from the velocity distribution functions of exospheric-origin pickup protons with energies well above that of the solar wind. Based on the results of the semi-automated method, the IMF orientation without its polarity can be estimated for 10 events in which significant precipitating planetary heavy ions were detected by MEX within the same orbit between July 2007 and September 2009. Because the IMF polarity cannot be determined only from the MEX ion data analyses, statistical trajectory tracing simulations of exospheric-origin protons are also performed to determine the IMF sector polarity. The IMF polarity can be determined by comparing the velocity distribution of exospheric-origin pickup protons observed by MEX with those obtained from statistical trajectory tracing simulations under two cases of possible IMF polarity conditions. Through data analyses and test particle simulations, I analyze the statistical properties of planetary heavy-ion precipitation toward the Martian ionosphere and the role of the solar wind variations in atmospheric escape from Mars based on the MEX observations.

In Chapter 5, I explore the role of crustal magnetic fields in atmospheric escape from Mars based on the MGS observations. As shown in Section 1.5, several additional escape processes associated can be with crustal magnetic fields. In particular, I evaluate the contribution of magnetic flux ropes to the ion escape from Mars. Although detached magnetic flux ropes filled with a number of Martian ionospheric plasma can be enhanced the ion escape rates, it is difficult to evaluate the atmospheric escape rate resulting from Martian flux ropes based on single spacecraft data because of the ambiguity in estimating the shape and size of the observed magnetic flux ropes. To overcome the observational limitation of the Martian magnetic flux ropes observed by single spacecraft, the Grad-Shafranov reconstruction (GSR) technique is applied in Chapter 5 to the Martian flux ropes observed by MGS to estimate their shape and

size. The GSR technique can provide a two-dimensional axial magnetic field map as well as the axial orientation from single spacecraft particle and field data under the assumption that the structure is magneto-hydrostatic and time-independent. Using their reconstructed spatial structures, I then impose constraints on their shape and size to assess the escape rate associated with removal of ions via magnetic flux ropes propagating away from the planet.

In Chapter 6, I examine a possible formation process of the Martian magnetic flux ropes observed downstream from the strong crustal magnetic fields in the southern hemisphere based on the results derived from the GSR technique. Because the magnetic flux ropes observed downstream from the Martian crustal magnetic fields have a large spatial scale [e.g., *Brain et al.*, 2010a], they could significantly contribute to the atmospheric escape from Mars. A statistical study is conducted for the 297 reconstructed magnetic flux rope events obtained from the MGS measurements between April 1999 and November 2006. Based on the statistical results, I investigate the dependence of crustal magnetic fields on their formation, which is based on the GSR results.

In Chapter 7, the results are summarized with respect to the Martian plasma environment derived from the MEX and MGS measurements. I conclude with the role of solar wind variations and crustal magnetic fields in the atmospheric escape from Mars based on current and previous in-situ spacecraft observations devoted to determining the solar wind interaction with Mars.

Chapter 2

Instrumentations and Data Sets

2.1 Mars Express (MEX)

2.1.1 Overview of MEX

Mars Express (MEX) is the first European mission to the red planet managed by the European Space Agency (ESA). MEX was successfully launched on June 2, 2003 and was captured into Martian orbit on December 25, 2003. MEX is a three-axis stabilized spacecraft with a fixed high-gain antenna and body-mounted instruments, and is dedicated to the orbital and in-situ comprehensive measurements of the planetary interior, subsurface, surface and atmosphere. MEX established a highly elliptical quasi-polar orbit (inclination: 86°) with a periapsis (apoapsis) of about 270 (10,000) km from the surface, respectively. The MEX orbital period is approximately 6.75 hours.

The MEX orbiter scientific payload totals about 116 kg shared by six instruments, in addition to a radio-science experiment. The description of objectives of each instrument is summarized below;

- Surface/subsurface instruments
 - HRSC (High Resolution Stereo Camera)

- OMEGA (Visible and Infrared Mineralogical Mapping Spectrometer)
- MARSIS (Sub-surface Sounding Radar Altimeter)
- Atmosphere/Ionosphere instruments
 - PFS (Planetary Fourier Spectrometer)
 - SPICAM (Ultraviolet and Infrared Atmospheric Spectrometer)
 - ASPERA-3 (Space Plasma and Energetic Neutral Atoms Analyzer)
- Radio link
 - MaRS (Mars Radio Science experiment)

In this thesis, the ASPERA-3 package is only utilized. *Chicarro et al.* [2004] shows more detailed description of the MEX spacecraft.

2.1.2 ASPERA-3 (Analyser of Space Plasmas and Energetic Atoms) Instrumentation

The ASPERA-3 (Analyzer of Space Plasma and Energetic Atoms) instrument is a comprehensive plasma package capable of measuring energetic neutral atoms (ENA), electrons, and ions [*Barabash et al.*, 2006]. ASPERA-3 consists of two units, the main unit (MU) and the ion mass analyzer (IMA). The MU comprises three sensors, neutral particle imager (NPI), neutral particle detector (NPD), electron spectrometer (ELS). The highly ecliptic orbit of MEX allows to observe various plasma domains around Mars, that is, the solar wind, magnetosheath, the magnetic pileup region (MPR) down to the vicinity of Martian ionosphere. In this thesis, the data acquired from IMA is only utilized.

The IMA instrument (Figure 2.1) determines the composition, energy, and angular distribution of ions in the energy range from ~ 10 eV/ q to 30 keV/ q (where q is the electric charge) with an energy resolution of 7 %. The instantaneous field of view (FOV) is $4.5^\circ \times 360^\circ$. The IMA instrument can detect ion species with a mass per charge ratio of up to ~ 80 and can distinguish H^+ , He^{2+} , O^+ , O_2^+ and CO_2^+ ions.

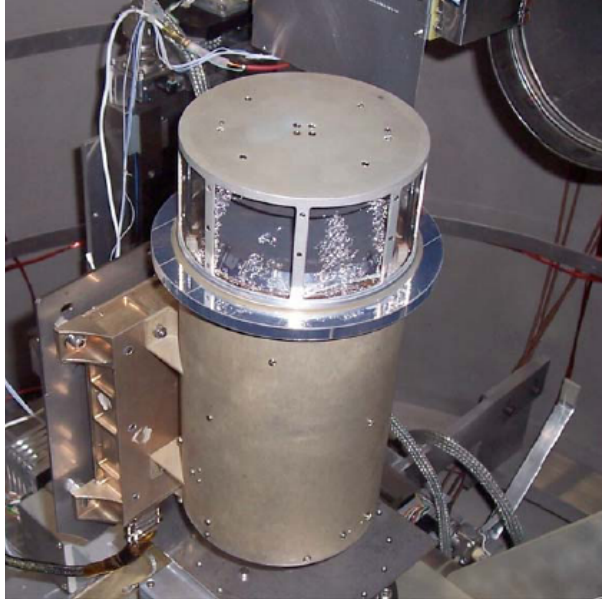


Figure 2.1: The IMA instrument in the vacuum chamber during calibrations [*Barabash et al.*, 2006].

The principal diagram of the IMA instrument is shown in 2.2. Ions enter the analyzer through the external grounded grid. Behind the grid, there is a deflection system whose purpose is to vary the incident polar angle of particles (shown in 2.2 as trajectories 1, 2 and 3). The deflection angle depends on the voltage applied to the deflector electrodes and lies within the $\pm 45^\circ$ from the equatorial plane in the instrument. The ions pass through the top-hat analyzer, which has a full 360° cylindrical symmetry in the azimuth range perpendicular to the symmetry axis, and selects only the given particle energy according to the internal voltage. The total FOV of the IMA is thus to be $90^\circ \times 360^\circ$. The ions subsequently pass through the magnetic separation section. The cut of this section in the azimuth plane is shown in the right panel of Figure 2.2. The radial deviation of the ion trajectories at the exit of the magnetic field region corresponds to the particle velocity per charge. Since the particles exiting the electrostatic analyzer have the same energy per charge, the radial deviation where particles are detected reflect the incident ion species (mass per charge).

To provide the possibility to measure light ions at the low energies, such as protons

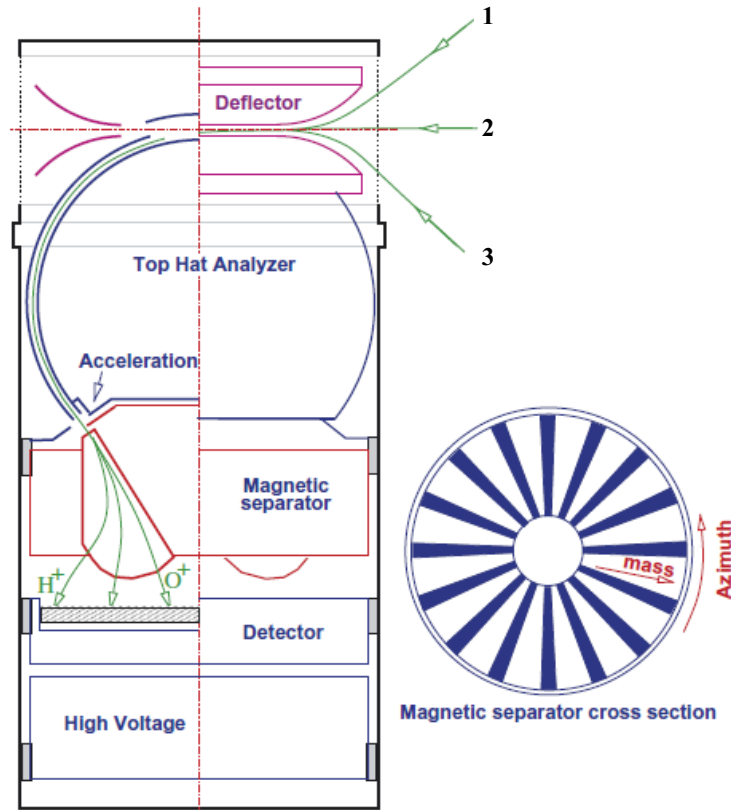


Figure 2.2: Cross section of the IMA sensor (left) with example of the ion trajectories, and magnet separator (right) [Barabash *et al.*, 2006].

which have too small gyro radius to reach the detector, can be accelerated by certain voltage between the exit of top-hat analyzer and the magnetic separator entrance. This acceleration system is referred as post-acceleration (PACC). The locations where the ions which have the same mass per charge can be detected depend on the PACC mode. However, a part of the light ions with low energies ($\lesssim 700$ eV) tend to detect regardless of the mass channels, even though the PACC is used.

When a full three-dimensional ion spectrum is observed by IMA, the fastest changing parameter is the particle energy, It sweeps from 30 keV down to the 10 eV over 96 logarithmically equidistant steps. The exposure time on the each step is 125 msec. During the time interval, 16 azimuth sectors are accumulated. After each complete energy sweep the instrument changes the elevation angle of the field of view. Electrostatic sweeping performs elevation from -45° up to $+45^\circ$ of the elevation angle over

16 steps. The time resolution to complete a full three-dimensional spectrum scan is 192 sec. This spectrum consists of 32 radial mass points \times 16 azimuth sectors \times 96 energy steps \times 16 elevation angles. In addition, The low energy measurements (≤ 50 eV) were performed without elevation scanning after May 2007 [Lundin *et al.*, 2008a]. As a result, a FOV is limited to be $4.5^\circ \times 360^\circ$ in this low energy range (See Barabash *et al.* [2006], for details of ASPERA-3's general performance).

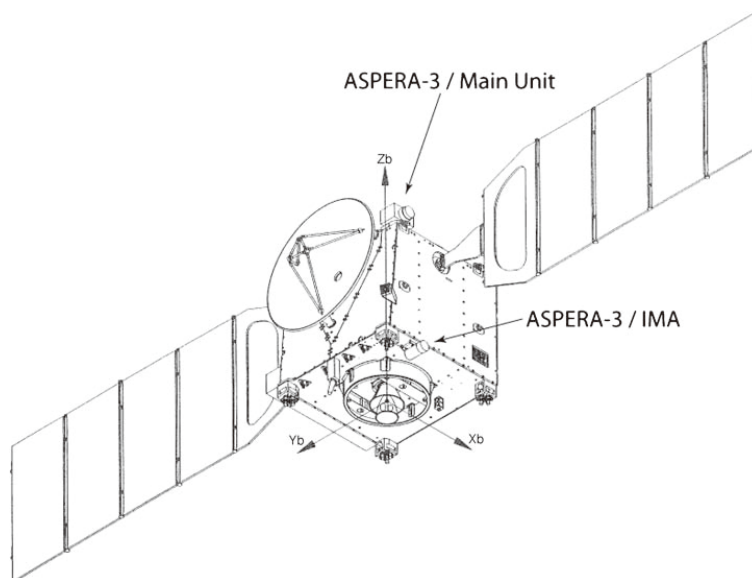


Figure 2.3: Schematic figure of ASPERA-3 locations on the MEX spacecraft. Reproduced from Barabash *et al.* [2006].

Figure 2.3 shows the sketch of the locations where ASPERA-3 instruments are accommodated. It should be noted that a part of FOV of the IMA instrument can be obstructed by the spacecraft body or a solar panel, because MEX is three-axis stabilized spacecraft. In fact, ion fluxes could be lower in the direction of the elevation angle below $\sim -2^\circ$ and azimuthal sectors mainly from 9 to 15, or the elevation angle $\sim 8^\circ$ and the azimuthal sectors from 11 to 13.

2.2 Mars Global Surveyor (MGS)

The Mars Global Surveyor (MGS) spacecraft for the NASA mission was inserted into the Martian orbit on September 1997, and had observed in orbit for approxi-

mately 9 years. The MGS mission was mainly divided into 2 phases, which are the pre-mapping and mapping phases, respectively. The pre-mapping phase lasted until March, 1999, whose orbital configuration is highly elliptical, and was gradually altered to be circularized via an aerobreaking technique. After March, 1999, the MGS mission began mapping phase, and lasted until the end of the mission (November, 2006). In this mapping phase, MGS was in quasi-circular orbit at an altitude of approximately 400 km from the surface, and the spacecraft orbit had fixed local time of $\sim 2\text{am}/2\text{pm}$ during the mapping phase [e.g., *Albee et al.*, 2001]. The orbital periods during the mapping phase had been also fixed approximately 2 hours. In this thesis, I used the MGS data only during the mapping phase.

The MGS science payload included the Mars Orbital Camera (MOC), Mars Orbiter Laser Altimeter (MOLA), Thermal Emission Spectrometer (TES), Ultrastable Oscillator (USO) for Radio Science experiments, and Magnetometer/Electron Reflector (MAG/ER) packages, respectively. In additions to those instruments, the spacecraft accelerometers as well as horizon sensors were used to investigate Martian atmospheric dynamics during aerobreaking. The MAG/ER package is only utilized in this thesis. See *Albee et al.* [2001] for more detailed description of the MGS spacecraft.

MAG consists of two identical triaxial fluxgate magnetometers. MAG provides vector magnetic fields every 0.75–3.0 seconds [*Acuña et al.*, 1992]. ER is a cylindrically symmetric top-hat electrostatic analyzer used to detect suprathermal electrons. ER determines energy and angular distribution of electrons in the energy range from 10 eV to 20 keV with an energy resolution of 25%. ER measures electron fluxes in 16 sectors within the total field of view (FOV) of $14^\circ \times 360^\circ$, in which each sector has FOV of $14^\circ \times 22.5^\circ$. Omni-directional energy spectra can be sampled every 12–48 seconds depending on the telemetry rate between Earth and Mars [*Mitchell et al.*, 2001]. By combining the two datasets described above, electron pitch angle distributions can be constructed. However, the coverage in pitch angle space varies as a function of time and location because this coverage depends on the orientation of the two-dimensional FOV of the ER experiment with respect to the observed magnetic field direction.

Chapter 3

Planetary heavy-ion precipitations toward Martian ionosphere during CIR passages

3.1 Introduction

Based on the in-situ plasma measurements obtained from Mars Express (MEX), escape rates of planetary heavy ions (PHIs) have a large dependence on the solar wind and solar radiation varieties not only in a short-time scale (\approx a few days), e.g., CIRs or CMEs [e.g., *Dubinin et al.*, 2009; *Edberg et al.*, 2010], but also in the long time (\approx the solar cycle, 11 years), e.g., the solar EUV/XUV flux [e.g., *Lundin et al.*, 2008b; *Nilsson et al.*, 2010]. It is thus important to understand how the upper atmosphere responds to the solar wind variations, and to quantitatively clarify which atmospheric escape process is responsible for the atmospheric erosion from Mars under various solar wind conditions. To perceive the solar wind conditions arrived at Mars is necessary so as to investigate the response between a dynamics of Martian upper atmosphere and the solar wind variations.

As shown in Section 1.4, escape rates of PHIs from Martian upper atmosphere have been reported on the basis of plasma observations by the Phobos-2 as well as the MEX spacecraft [e.g., *Lundin et al.*, 1989, 2004; *Carlsson et al.*, 2006; *Barabash*

et al., 2007a]. Phobos-2 observations first revealed that upper atmospheric plasmas were escaping from Mars during a period of high solar activity. The estimated O^+ escape rate at that time was $2.0\text{--}3.0 \times 10^{25} \text{ s}^{-1}$ with energies from 0.5 eV to 24 keV [e.g., *Lundin et al.*, 1989; *Ramstad et al.*, 2013]. The MEX measurements were taken under conditions of low solar activity (2004–). The global averaged escape rates of PHIs, such as O^+ , O_2^+ , and CO_2^+ , range between 3.9×10^{23} and $3.3 \times 10^{24} \text{ s}^{-1}$, based on MEX observations [*Barabash et al.*, 2007a; *Lundin et al.*, 2008a]. Previous studies indicate that the ion escape rate from Mars depends on the solar activity and the solar wind conditions [e.g., *Barabash et al.*, 2007a; *Lundin et al.*, 2008a, 2013]. It is important to understand how the interaction between the solar wind and the Martian upper atmosphere is influenced by the variability of the solar wind. There are several possible candidates of the ion escape processes induced by the solar wind, as described in Section 1.3. However, the ion escape processes responsible for the different solar wind conditions are not fully understood.

It is observationally known in Earth that interplanetary disturbances, such as CIRs and CMEs, can cause geoeffective activities, such as magnetic storms, as a consequence of the interaction with the Earth’s magnetosphere [e.g., *Tsurutani et al.*, 2006; *Richardson et al.*, 2006]. If these interplanetary disturbances arrive at unmagnetized planets like Mars or Venus, their disturbances, and/or associated high-energy particles may result in more drastic dynamic change around unmagnetized planets’ plasma environment than Earth [*Futaana et al.*, 2008]. In addition, Mars has a higher chance of encountering CIR shock structures than Venus, because CIRs are developed well beyond 1 AU from the Sun [e.g., *Gosling and Pizzo*, 1999].

The plasma interaction of unmagnetized planets with interplanetary disturbances in the solar wind has been an important issue to understand atmospheric escape from those planets. *Dubinin et al.* [2009] identified a scavenging of the Martian ionosphere during the passage of a CIR. The estimated increase in the escape rate was as high as by a factor of ~ 10 . A statistical survey in terms of anti-sunward PHI fluxes during the solar minimum indicates that the PHI escape rates during the passage of a CIR increases by a factor of ~ 2.5 for Mars [*Edberg et al.*, 2010; *Nilsson et al.*, 2011] (Figure 1.10) and ~ 1.9 for Venus [*Edberg et al.*, 2011], owing to pressure pulses in the solar

wind. CMEs also significantly disturb the plasma environment around unmagnetized planets and can enhance the atmospheric escape rate [e.g., *Luhmann et al.*, 2007; *Futaana et al.*, 2008; *McEnulty et al.*, 2010]. The enhancement of atmospheric escape rate due to the high-energy particles associated with CMEs had been detected at least by a factor of ~ 10 [e.g., *Futaana et al.*, 2008]. While the physical processes responsible for the enhancement of the escape rate during interplanetary disturbances are not yet fully understood, atmospheric escape phenomena are highly variable owing to them.

In this chapter, we reported on the characteristic PHI signature observed in the vicinity of the Martian ionosphere during passages of CIRs on the basis of analyses of MEX/IMA instrument. We confirmed from the velocity distribution function during this signature that the observed PHIs are not escaping, but mostly precipitating toward the Martian upper atmosphere in Section 3.3. We performed semi-statistical survey in terms of the PHI precipitation signatures by using approximately 1 month data observed by MEX on September, 2007 in order to investigate the solar wind dependence on such precipitating PHI phenomena. Since the elongation between Mars and Earth as viewed from the Sun is about 42° in average during the surveyed time period, it was capable of comparing the solar wind velocity estimated from MEX ion data (Section 3.2) with the time-shifted ACE solar data observed upstream from Earth. By comparisons of the solar wind data derived from different methods, we revealed that the solar wind variations indicated the CIR passages arrived at Mars quasiperiodically in the surveyed time period. Further, we investigated the potential effects of PHI precipitations on the solar wind variations as well as CIR passages arrived at Mars (Section 3.4).

3.2 Estimation of Solar Wind Velocity from MEX Observations

There is no solar wind monitor in the Martian orbit. However, MEX partly passes in the solar wind region, because MEX is eccentric elliptical orbit. We can thus estimate the solar wind conditions from MEX plasma observations, while MEX observes

in the solar wind region.

The solar wind key parameters are the number density, bulk velocity, temperature, and magnetic field. We can derive the number density n , and bulk velocity vector \mathbf{v} , and temperature T from IMA measurements by using moment calculation of phase space distribution function $f(\mathbf{r}, \mathbf{v}, t)$ with below equations;

$$n(\mathbf{r}, t) = \int_{\mathbf{v}} f(\mathbf{r}, \mathbf{v}, t) d^3\mathbf{v}, \quad (3.1)$$

$$n(\mathbf{r}, t)\mathbf{v}(\mathbf{r}, t) = \int_{\mathbf{v}} \mathbf{v}f(\mathbf{r}, \mathbf{v}, t) d^3\mathbf{v}, \quad (3.2)$$

$$\mathbf{P}(\mathbf{r}, t) = \int_{\mathbf{v}} m\mathbf{v}\mathbf{v}f(\mathbf{r}, \mathbf{v}, t) d^3\mathbf{v}, \quad (3.3)$$

where at a certain position \mathbf{r} and at a time t , m is the ion mass and \mathbf{P} is the pressure tensor. The temperature can then be calculated as $T = \mathbf{P}/nk_B$, where k_B is the Boltzmann constant. However, it is somewhat difficult to calculate n , in conjunction with T , because the IMA is not optimized for the solar wind light ion observations, and IMA sensor often detects the solar wind light ion with low energy ($\lesssim 700$ eV, depending on the post acceleration (PACC) mode of IMA), regardless of the relevant mass channel [Barabash *et al.*, 2006; Fränz *et al.*, 2006]. Therefore, we only calculated the magnitude of the solar wind velocity from IMA. The procedure of the estimations of the solar wind velocity is described below.

In order to calculate the solar wind velocity from the IMA data, we carried out the shifted Maxwellian fitting to each IMA velocity distribution obtained in one full three-dimensional scan, i.e., every 192 sec. First, assuming that the main ion component observed in the solar wind region consists of protons and has one-dimensional shifted Maxwellian distribution for the magnitude of velocity. A shifted Maxwellian distribution used as the fitting function can be written as follows:

$$f(v) = A_1 \exp(-A_2(v - v_i)^2), \quad (3.4)$$

where v represents the magnitude of velocity in the phase space. Both A_1 and A_2 are coefficients related to solar wind density and temperature, and v_i is the solar wind velocity to be obtained. Then using the equation of (21) in Subsection 3.2 of Fränz

et al. [2006], the observed ion distribution function to be fitted can be constructed as:

$$f(v) = \frac{m^2}{2G\tau} \cdot \frac{C(E)}{\Delta E \cdot E} = \left(\frac{2}{G\varepsilon\tau} \right) \cdot \frac{C(v)}{v^4}, \quad (3.5)$$

where C , G , and τ represent the detector counts integrated over mass channels as well as azimuth (ϕ) and elevation (θ) channels, the geometric factor of the detector, and the sampling time, respectively. $\Delta E (= E_{n+1} - E_n)$ indicates the energy width of the n -th energy channel. In order to focus on the main component in the distribution function, we also performed the noise reduction. The Newton-Raphson as well as Levenberg-Marquardt least-squares methods are utilized in the fitting. The solar wind velocity derived from this method described above is used to investigate the solar wind dependence on the characteristic PHI signature shown in the following sections.

3.3 Characteristic Planetary Heavy-Ion Enhancement Event

In this section, we report on a typical CIR passage event observed by MEX on September 19, 2007. Figure 3.1a shows a typical example of IMA observation during a quiet solar wind condition. As shown in the energy-time spectrogram, the MEX spacecraft first passed through the solar wind region and subsequently crossed the Martian bow shock (BS) at $\sim 03:32$ UT to the magnetosheath and then the magnetic pileup boundary (MPB) at $\sim 04:35$ UT in the nightside. In this thesis, MPB is defined as where the count rate of solar wind plasma decreases sharply [Nagy *et al.*, 2004] because of the absence of the magnetometer onboard MEX, although MPB is generally defined from the magnetic field measurement. After the spacecraft traverses the vicinity of the Martian ionosphere corresponding to the MEX periapsis (the magenta vertical line), the spacecraft again traverses MPB, the dayside magnetosheath, and BS again in the outbound path. A characteristic periodic pattern (with a period of 192 seconds) evident in Figure 3.1, corresponds to the full-elevation scan of IMA (16 directions from -45 degree to +45 degree).

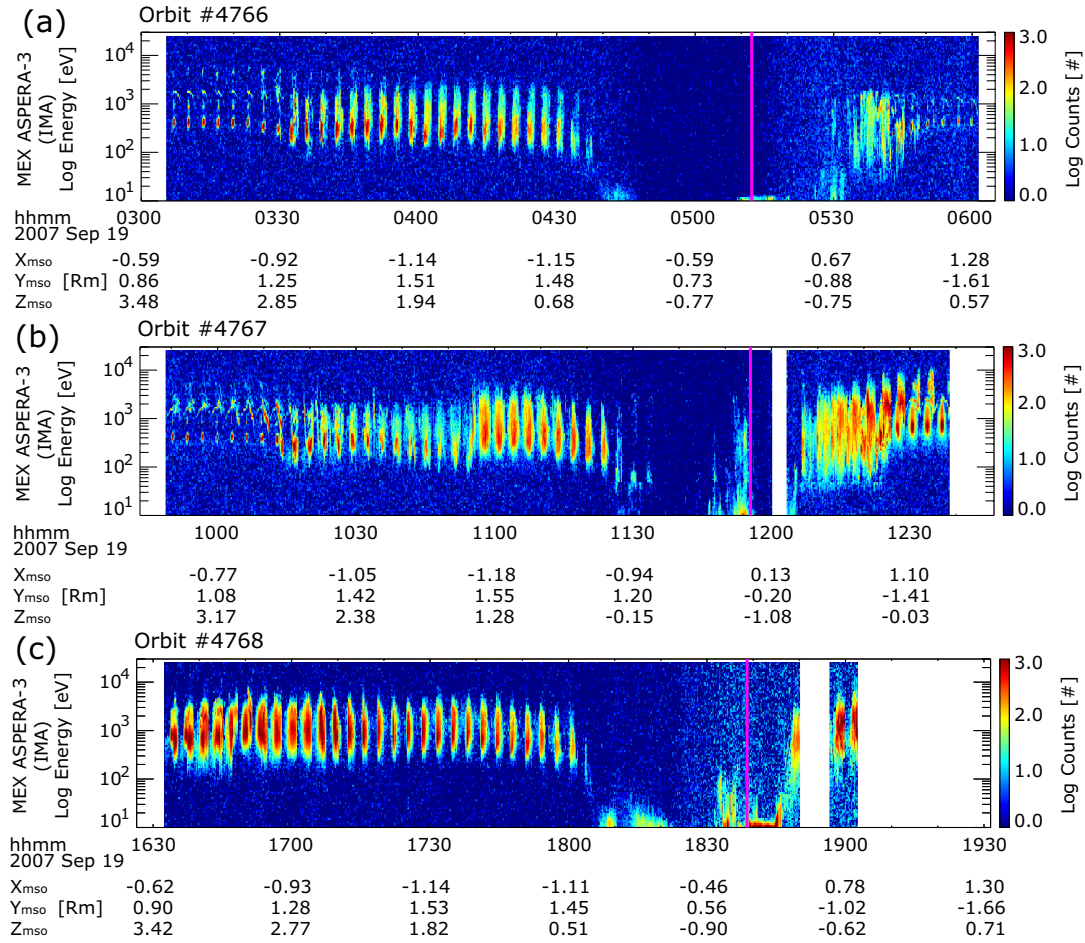


Figure 3.1: Energy-time spectrograms of ions measured by ASPERA-3 IMA observed in MEX orbit (a) #4766, (b) #4767, and (c) #4768, respectively. The color code shows ion counts integrated over all mass channels and azimuth sectors. The magenta vertical line in each panel corresponds to the time when MEX passed through the periapsis. The background noise level in raw data gradually increased after $\sim 18:20$ UT on September 19, 2007 for orbit #4768, and the uniform background noise reduction is performed in panel (c). The background noise to be subtracted is estimated from a smoothed time profile (with moving average over 192 sec) of average all-mass-integrated counts detected in the two highest energy channels.

In the following orbit #4767 shown in Figure 3.1b, we can identify an additional signature in the energy-time spectrogram $\sim 10:55$ UT on September 19, 2007, which shows the abrupt discontinuous increases of both the average ion energy and temperature. The estimated ion velocity calculated by the shifted Maxwellian fitting described in Section 3.2 indicates a shock-like increase. The discontinuity signature turn out to be that MEX encountered a CIR structure of the solar wind, based on the solar wind comparison shown in the following section. Due to the CIR structure passage, the ion flux observed by IMA increased in the following orbit #4768 shown in Figure 3.1c. Another remarkable feature in Figure 3.1b is that the ion flux enhancement attained to a few keV is detected at $\sim 11:53$ UT, when MEX passed the vicinity of the Martian ionosphere just after the CIR structure arrival. The ion flux enhancement was not detected in the previous orbit #4766 (Figure 3.1a).

As clearly shown in the mass-energy matrix obtained at the time when heavy-ion flux was found in orbit #4767 (Figure 3.2), the ion enhancement signature up to a few keV observed near the periapsis is mostly composed of the PHIs. The ions counted in the high-energy range above 1 keV mainly consist of O^+ , while the ions in the low energy range (< 100 eV) include the group of molecular ions such as O_2^+ and CO_2^+ together with O^+ . Since the distributions of O^+ , O_2^+ , and CO_2^+ components in the IMA mass spectrum are expected partially overlap to each other, it is thus difficult to distinguish these PHIs clearly.

Figure 3.3 shows the cut of the three-dimensional distribution function of the PHIs in the MEX spacecraft (SC) coordinates [*Barabash et al.*, 2006], which is obtained by integration over all mass channels corresponding to ≥ 8 amu, for the same PHI enhancement event. Both Figures 3.3a and 3.3b depict the SC coordinates, and the red and orange circles around the distributions show the looking directions of Mars and Sun, respectively. It is clear that the ions observed in the energy range of ≥ 100 eV are predominantly precipitating toward the Martian upper atmosphere (from Figure 3.3a) with some anti-sunward velocity component (from Figure 3.3b). On the other hand, the low energy component (a few tens of eV) is mainly flowing upward from Mars. Therefore, the observation revealed that PHI fluxes precipitating toward the Martian upper atmosphere are enhanced during the CIR passage. However, a

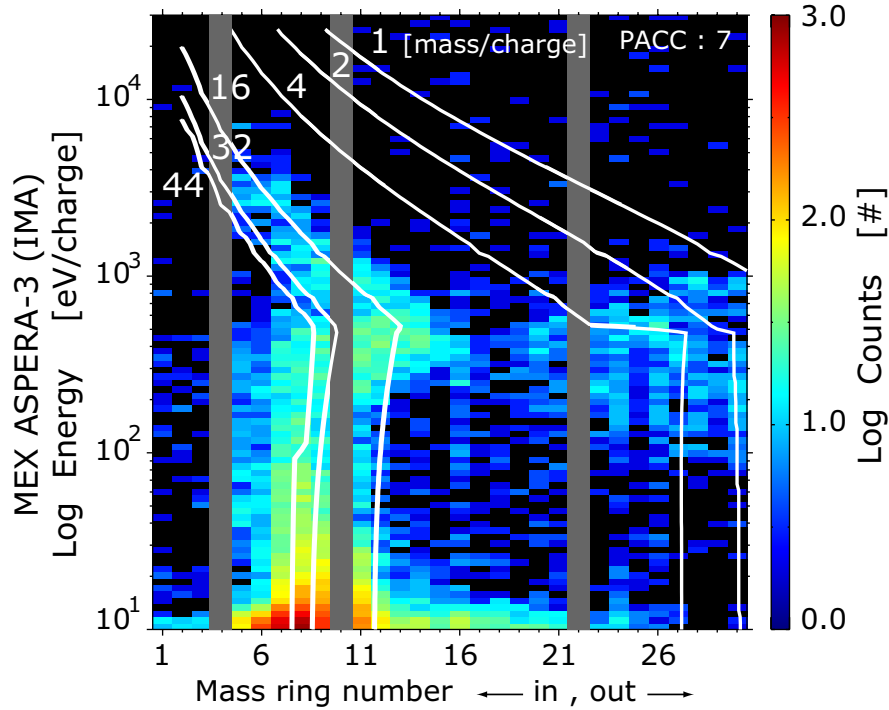


Figure 3.2: An energy-mass matrix observed by ASPERA-3 IMA during 11:50:33-11:56:44 UT (two full scans of data) on September 19, 2007, when the flux enhancement of ions up to a few keV is detected in the vicinity of the MEX periapsis as shown in Figure 3.1b. The ordinate indicates the energy per charge, and the abscissa shows the mass ring number of the instrument. The color code shows the ion counts, and the gray color indicate data gaps at the mass ring #4, 10, and 22. Over-plotted white lines display the expected locations in the matrix for ions with indicated atomic mass unit (amu) to be detected. Thus counts around lines for 16, 32, and 44 amu represent planetary heavy ions such as O^+ , O_2^+ , and CO_2^+ . Note that the noise level of mass ring #16 is known to be higher than that of other rings.

part of the IMA field-of-view, the elevation angle below ~ -2 degrees and azimuth sectors mainly from 9 to 15 or the elevation above ~ 8 degrees and the azimuth from 11 to 13 is significantly obstructed by the spacecraft body or a solar panel. Therefore, ion fluxes observed in these directions could be low due to artificial reasons. In this specific case near the MEX periapsis, the obstructed directions correspond to mostly the upward half of the distribution function. Thus we may miss the upward ions, if any, but the detection of the downward precipitation ions are not affected by the field-of-view (FOV) obstruction.

3.4 Dependence on Solar Wind Variations with Planetary Heavy-Ion Enhancements

In this section, we investigate the relationship between the PHI enhancement signature reported in the previous section and CIR passages in the solar wind using MEX data from September to October, 2007. Figure 3.4 shows the dependence on the solar wind conditions and PHI precipitation flux. In Figures 3.4a \sim c, we compared the solar wind velocity derived from the direct fitting of MEX data described above in Section 3.2 with ACE solar wind data, considering the travel time from Earth to Mars. We represents that the solar wind velocity derived from the MEX data is shown as blue filled circles seen in Figure 3.4a, and time-shifted ACE solar wind data is shown as black solid lines.

Here the time shift of the ACE satellite data (~ 111 hours) is determined from a combination of the traveling time estimation between ACE and MEX and adjustment by a few hours from the timing of the CIR-shock arrival between ACE and MEX data. This method of the constant time shifting might cause an overestimation during the latter of time period, because Mars gradually gets closer to Earth in this time period by ~ 11 hours or so [Vennerstrom *et al.*, 2003]. However, the time deviation is not large compared to the MEX's orbital period (~ 6.7 hours). The solar wind density (Figure 3.4b) and magnetic field strength (3.4c) observed by ACE at ~ 1 AU are also time-shifted without compensating about the spatial development from Earth to

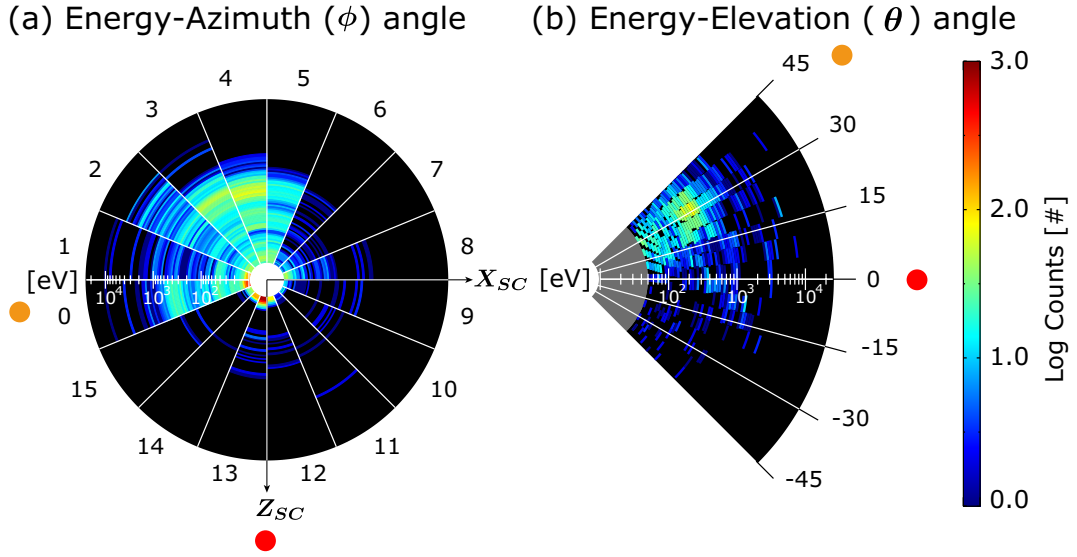


Figure 3.3: The three-dimensional distribution function of PHI observed by MEX/IMA during the one full electrostatic scanning near the MEX periapsis, when the flux enhancement of ions up to a few keV is detected in the MEX orbit #4767 as shown in Figure 3.1b. The radial scale in each panel represents the ion energy. The ion counts on a logarithmic scale is shown by color, and only the mass channels of heavy-ion components (≥ 8 amu) are integrated. Both panels depict the MEX spacecraft (SC) coordinates, and the red and orange circles show the looking directions of Mars and Sun, respectively. The ion counts detected in the bottom half of the panel (a) corresponds to the upward (outflow) fluxes from Mars. (a) Energy-azimuth sectors distribution: All elevation angle channels are integrated. The numbers noted around the periphery of the plot correspond to IMA azimuth sector numbers. (b) Energy-elevation angle distribution: All azimuth angle channels are integrated. The data in the low energy range below 50 eV are not shown (gray area), because the elevation scanning is not operated in this energy range. Description of the field-of-view obstruction for the IMA data by the spacecraft body and a solar panel is given in the text.

Mars to infer the solar wind conditions of the Martian orbit.

As shown in Figure 3.4a, the solar wind velocities obtained from MEX and time-shifted ACE data have similar time variation, and both spacecraft observed the CIR-like velocity variation, i.e., the change from slow to fast solar wind flows, four times during the period of interest. We thus identified CIR structures passed through Mars quasiperiodically.

Figure 3.4d represents the flux of precipitating PHIs observed near the MEX periapsis of each orbit. In this thesis, we investigated the observation only around the MEX periapsis so as to avoid the solar wind proton contamination as pointed out by *Fränz et al.* [2006] and effects of the spacecraft attitude change. However, the PHI precipitations are sometimes observed continuously from the magnetic pile-up region. The obstruction areas of the IMA field-of-view are located mostly in the upward half of the field-of-view near the periapsis as mentioned in the previous subsection. Hence, the effect of the obstruction is negligible in calculation of the downward (precipitation) flux. The division of the energy range at 500 eV is adopted to compare the result with a previous model calculation by *Chaufray et al.* [2007]. The value of 50 eV corresponds to the lower limit of the IMA observations with the elevation scanning. It should be noted that the level of background noise counts is not always uniform, and therefore, the low precipitation flux (about $\leq 10^5 \text{ cm}^{-2} \cdot \text{s}^{-1}$) can sometimes be affected by noise counts.

While MEX had reasonably good data coverage in the vicinity of the ionosphere (around the MEX periapsides) as shown in Figure 3.4e, the PHI precipitation is detected only in the limited time intervals (Figure 3.4d). A remarkable feature here is that the precipitating PHI detections mostly coincide with passage of CIR structures identified from the solar wind data. As shown in Figures 3.4b and 3.4c, the precipitation flux of $\geq 10^5 \text{ cm}^{-2} \cdot \text{s}^{-1}$ events tend to be observed during the period of the high magnetic field strength rather than during a high density period. The September 19, 2007 event reported in Section 3.3 corresponds to the left-most magenta vertical dashed line. It should be noted that the ion flux in the low energy range ($10 \leq E < 50$ eV) in which the ASPERA-3 IMA operates with a non-elevation scanning mode (not shown) indicates that the upward flux is more frequently observed near the MEX

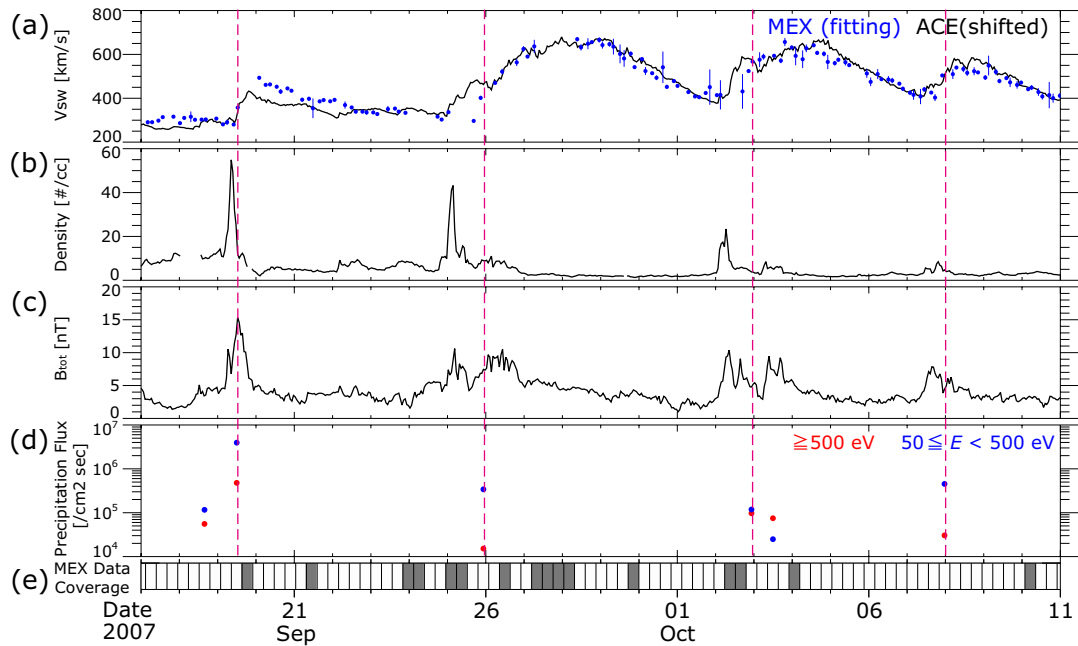


Figure 3.4: A summary time series plots of the solar wind and MEX precipitating PHI observations from September 17 to October 11, 2007: (a) The solar wind velocity derived from a shifted Maxwellian fitting of the MEX ASPERA-3 IMA data (blue circles), and the time-shifted ACE satellite data considering the traveling time of the solar wind from Earth to Martian orbit (black solid line). (b) The solar wind density and (c) the interplanetary magnetic field strength (B_{tot}) measured by ACE, which are also time-shifted to the Martian orbit. (d) Precipitating PHI fluxes derived by the moment calculation of MEX/IMA data with the same method as in *Fränz et al.* [2006]. The red and blue solid circles correspond to the high-energy (≥ 500 eV) and low-energy ($50 \leq E < 500$ eV) ions, respectively. (e) Data coverage of MEX/IMA at periapsis. Gray color shows the data gaps of IMA at the periapsides. Magenta vertical dashed lines indicate the MEX orbit when the enhancement of PHIs in the vicinity of Martian ionosphere are observed, and corresponding energy-time spectrograms are shown in Figure 3.1b.

periapsis locations and, its correlation with the solar wind conditions is less clear.

3.5 Discussion of Effects of Solar Wind Variations on Planetary Heavy-Ion Precipitations

In this section, we discussed potential effects of solar wind variations on the intermittent observations of precipitating PHIs. PHIs are generally produced in the Martian upper atmosphere at dayside via photoionization, impact with solar wind electrons, or charge exchange reaction with solar wind ions [e.g., *Shizgal and Arkos, 1996*]. Once ionized, these PHIs can be picked up in the solar wind and rapidly swept away from Mars mainly in the solar wind electric field direction, because the gyro radii of the picked-up PHIs are typically much larger scale than the planetary size (c.f., the Martian radius is $\simeq 3397$ km). However, when the strength of the IMF is increased due to the compressed interplanetary magnetic field structure in front of CIR, the gyro radii of picked-up PHIs become smaller, and sometimes are comparable to the Martian size. During the period, picked-up PHIs have more chance to precipitate into Martian upper atmosphere.

Table 3.1: A summary of estimated gyro radius of picked-up O^+ ions before and after CIR passages.

Event date	2007/09/19		2007/09/25		2007/10/03		2007/10/08	
Orbit #	4767		4790		4815		4833	
CIR shock	Before	After	Before	After	Before	After	Before	After
velocity [km/s]	280	380	310	525	430	575	405	510
magnetic field [nT]	2.0	7.1	2.4	4.5	1.7	4.5	1.3	3.5
gyro radius [km]	23800	8900	21700	19200	41600	21150	52100	24600
ratio	0.37		0.88		0.51		0.47	
gyro radius [km] (precipitate ions)	4400		1400		4850		3700	

Table 3.1 shows a summary of the typical gyro radius estimation for picked-up O^+

ions before and after CIR passages. Those events are corresponding to 4 magenta vertical dashed lines in Figure 3.4. Each gyro radius is calculated by using the solar wind velocity derived from the MEX data and the IMF strength B inferred from ACE data assuming that the falling factor is $1/r^2$ from Earth to the Martian orbit. Here we took into account the decrease of B from Earth to the Martian orbit, however we cannot know the accurate falling factor, considering the time development of the CIR from terrestrial to the Martian orbit. Therefore, this may have caused an overestimation of the gyro radii. For example, if we do not assume that the falling factor is $1/r^2$ but constant over r , the gyro radii becomes about 2.3 times smaller than the listed values in Table 3.1. These values are closer to the Martian values. For calculation of gyro radius before a CIR, averages of the solar wind velocity and magnetic field strength are used. As for the values after a CIR passage, the peak value of B and simultaneous solar wind velocity in each CIR structure are used. The result indicates that the gyro radii of picked-up O^+ ions became smaller after the CIR arrival and became comparable to the Martian radius or diameter. In addition, the gyro radius estimated from the maximum energy of the precipitating heavy ions is smaller than the Martian radius for all events as shown in the bottom row in Table 3.1. This variation of the gyro radius of picked-up ions before and after CIR passage is corresponding to the evidence that enhancements of the IMF strength due to CIR passages can depend on the PHI precipitations.

The previous studies based on the MEX observations show that the enhancement of anti-sunward escaping flux of PHIs coincides with the CIRs arrival [e.g., *Dubinin et al.*, 2009; *Edberg et al.*, 2010]. In the semi-statistical survey for the MEX ion data, we only focus on the observations in the vicinity of the terminator region due to the orbit geometry. It should be noted that the PHI precipitations are sometimes observed continuously from the magnetic pileup region. In the event reported by *Dubinin et al.* [2009] around February 10, 2008, the MEX periapsis was located in the dayside (local time of ~ 3 pm). At this location, we confirmed that the ion distribution function shows a drastic anti-sunward flow. This suggests that the ion distribution function during CIR passages depends on the observation location. A statistical study by *Edberg et al.* [2010] showed that the tailward flux of O^+ from the Martian upper

atmosphere during CIR passages is about 2.5 times larger than usual on the basis of MEX ASPERA-3 observations. As shown in Figure 1.10, the tailward direction is often included in the precipitating sector of the ion distribution function in the vicinity of the pericenter for the period we investigated in this chapter. Therefore, the results are consistent with those of the tailward O^+ flux enhancement during CIR passages. On one hand, the results also suggest that it is important to investigate three dimensional velocity distribution function data to understand the meaning of the tailward flux enhancement.

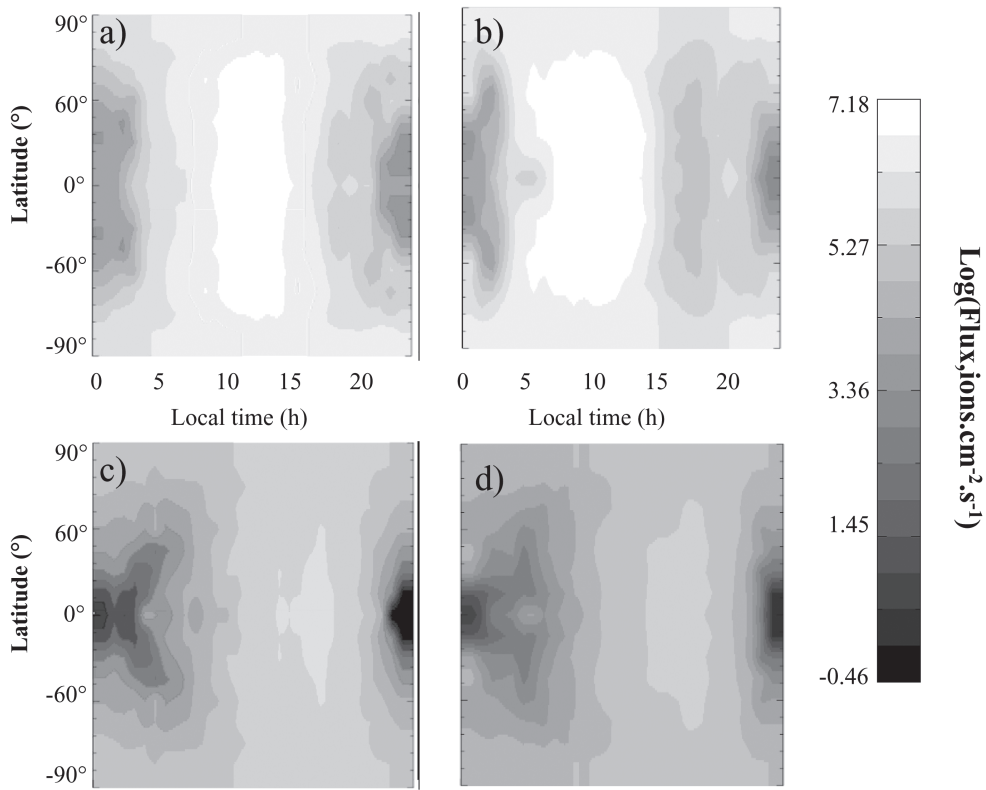


Figure 3.5: Hybrid simulation results of spatial distributions of the precipitating flux at an altitude of 300 km from the Martian surface [*Chaufray et al.*, 2007]. The top row represents the distribution for the low-energy (50–500 eV) incident particles for (a) a period of low solar activity and (b) a period of high solar activity, and the bottom row displays the distribution for the high-energy (≥ 500 eV) incident particles for (c) a period of low solar activity and (d) a period of high solar activity. The solar wind electric field is oriented along the Martian east-west axis.

Furthermore, the observed PHI precipitation flux during CIR passages is compared with a hybrid simulation result by *Chaufray et al.* [2007]. As shown in Figures 3.5a and 3.5c, the precipitating O^+ flux, which is thought to cause the ion sputtering, is $\sim 10^5\text{--}10^6$ ($\sim 10^4\text{--}10^5$) $\text{cm}^{-2}\cdot\text{s}^{-1}$ with energies of 50–500 eV (≥ 500 eV) at the periapsides when MEX observed precipitating PHIs. The simulation results agree well with the observed flux reported in Figure 3.4d on average. On the other hand, the important discrepancy between the model prediction and the MEX observations is an occurrence frequency of these events. Observations reveal that this level of PHI precipitation flux is only operating during the CIR passages, while the simulation results indicate that PHI precipitation always exist even under typical moderate solar wind conditions. These results suggest that the efficiency of the ion sputtering among the atmospheric escape processes from Mars is highly variable with dynamic solar wind variations [*Hara et al.*, 2011].

Chapter 4

Statistical properties of planetary heavy-ion precipitations toward the Martian ionosphere

4.1 Introduction

As reported in the previous Chapter 3, Mars Express (MEX) intermittently detected planetary heavy ions (PHIs) precipitating toward the Martian ionosphere, mostly accompanied with CIR passages in the solar wind [*Hara et al.*, 2011]. We proposed in *Hara et al.* [2011] that compressed interplanetary magnetic field (IMF) strength enhancements is important for picked-up PHIs to precipitate toward the Martian ionosphere, because gyro radii of picked-up PHIs might be comparable to the Martian planetary size during CIR passages.

In addition to the enhancement of the IMF strength, another key parameter relevant for understanding atmospheric energization and precipitation is the convective electric field ($\mathbf{E} = -\mathbf{V}_{\text{sw}} \times \mathbf{B}$, where \mathbf{V}_{sw} is the solar wind bulk velocity and \mathbf{B} is the interplanetary magnetic field (IMF) vector). It has been known from the MEX ion measurements that picked-up PHIs are distributed in a highly asymmetric fashion with respect to the convective electric field [*Barabash et al.*, 2007a; *Dubinin et al.*, 2008]. In addition, a part of picked-up ions precipitates onto Martian upper at-

mosphere. As mentioned in Section 1.3.4, picked-up ions precipitating onto Martian upper atmosphere should contribute to the atmospheric escape via ion sputtering process for ambient neutral particles [e.g., *Luhmann and Kozyra, 1991; Luhmann et al., 1992*]. *Luhmann and Kozyra [1991]* investigated the precipitating O^+ flux and energy on the dayside using test particle simulations. They predicted that the direction of the IMF determines the maximum precipitating energy and positions, and that the spatial distribution of the precipitating ions is also asymmetric with respect to the convective electric field in the solar wind. *Chaufray et al. [2007]* also investigated the spatial distribution of the precipitating flux of picked-up O^+ for both the solar maximum and minimum periods using a three-dimensional hybrid simulation. They found that high energy (≥ 500 eV) picked-up O^+ can preferentially precipitate into the downward electric field hemisphere, where the solar wind electric field is pointing to Mars (Figure 3.5). Chapter 3 reported on the PHI precipitation during passages of the compressed IMF region in front of CIRs [*Hara et al., 2011*]. However, the lack of magnetic field observations by MEX prevents a direct assessment of the effects of the solar wind electric field direction based on MEX measurements.

Although MEX does not have a magnetometer, in some cases we can estimate the IMF orientation from the three-dimensional velocity distribution of accelerated protons in the solar wind. These accelerated protons have a ring-like geometry because of their gyro-motion in the solar wind rest frame (We hereafter refer to these ions as ‘ring ions’). Using the fact that the gyration plane in the velocity phase space is perpendicular to the IMF, the IMF orientation is derived. Such ring ions were observed near Mars with Phobos-2 [*Barabash et al., 1991*]. As shown in Figure 4.1, MEX also occasionally detected ring ions near the Martian bow shock [*Yamauchi et al., 2006, 2008*]. The newly ionized neutral particles in the Martian hydrogen corona [*Yamauchi et al., 2006*] and the reflected solar wind from the bow shock [*Yamauchi et al., 2011*] may both provide substantial sources of the ring-ion population. The initial velocity \mathbf{V}_0 of the ring-ion population depends on their source mechanisms. Newly born ions have velocities $\mathbf{V}_0 \simeq 0$, whereas reflected ions have $\mathbf{V}_0 \neq 0$. The three-dimensional velocity distribution of the ions may be complicated owing to a variety of physical processes, including wave excitation, shock acceleration, and various instabilities [e.g.,

McClements and Dendy, 1993, and reference therein].

To derive the magnetic field direction, *Yamauchi et al. [2006]* applied minimum variance methods to the velocity vectors of ring ions. Later, the ring ions were manually separated from other ions. The method were improved to derive the IMF orientation from a limited portion of the ring distributions in *Yamauchi et al. [2008]*. Their estimation was compared with the IMF clock angle deduced from the magnetometer onboard the Mars Global Surveyor (MGS) spacecraft. Since the MGS data is available until November 2006, we cannot refer to MGS magnetometer after that time.

In this chapter, we investigated the effects of the solar wind electric field on PHI precipitations toward the Martian ionosphere, based on the MEX ion observations. The solar wind electric field as well as an associated IMF orientation is inferred from velocity distribution functions of ring ions. In Section 4.2, an automated method to discriminate the ring ion is shown to estimate the IMF orientation. We then perform a statistical survey of MEX/IMA data acquired between July 2007 and September 2009. We select the events in which both precipitating PHIs and ring ions are observed in the same orbit of MEX. The statistical results of precipitating PHIs into the Martian upper atmosphere are reported in Section 4.3. We then investigate the dependence of the precipitating PHIs on the solar wind electric field direction. In Section 4.4, we also assess a possibility to determine the IMF polarity with a help by a test particle simulation. In Section 4.5, we discuss possible physical mechanisms that control the precipitation of PHIs. Finally we summarize our results and suggest a possible scenario of precipitation of PHIs in Section 4.6.

4.2 Method of Estimating the IMF Orientation

4.2.1 Automated Extraction of Ring Ions

The IMF orientation can be estimated from the three-dimensional ring-ion velocity distribution functions obtained by MEX/IMA. We here describe our newly developed method of estimating the IMF orientation from the ring ion distribution. We assume that the IMF is nearly uniform over a distance greater than an ion gyroradius. We also

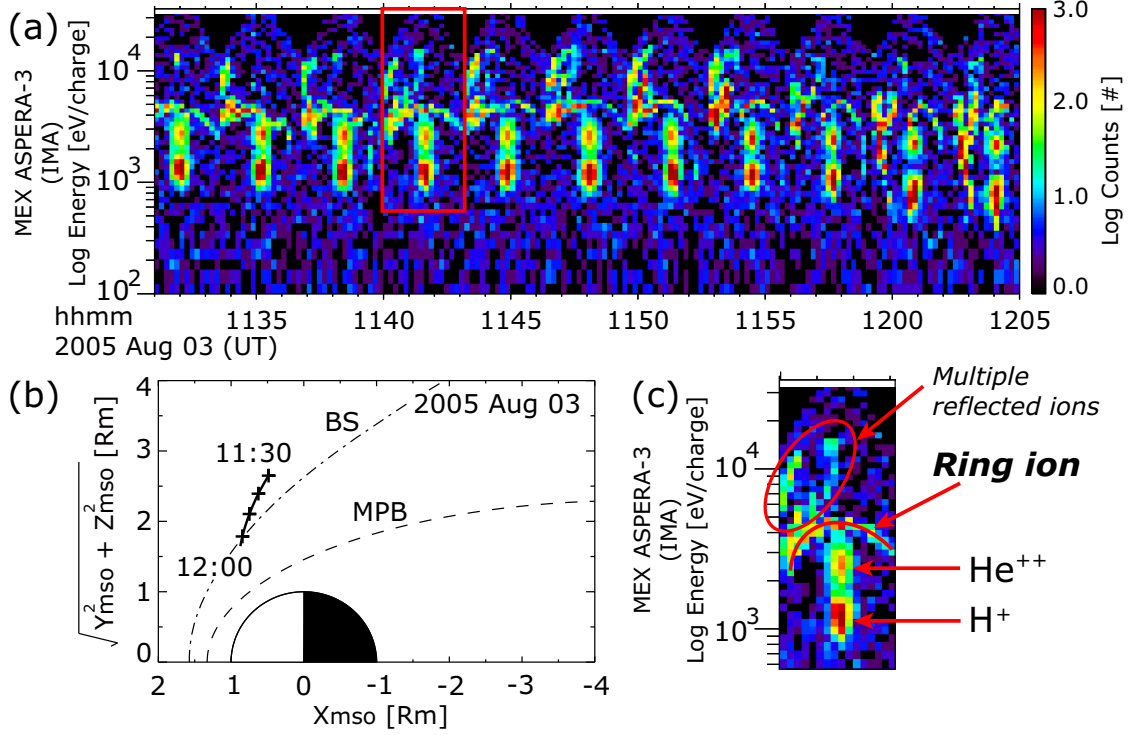


Figure 4.1: A typical example of the MEX ring ion observations in the solar wind near the Martian bow shock on August 3, 2005. (a) Energy-time spectrogram of the ions obtained by MEX/IMA. The color code shows the ion counts integrated over all mass channels and azimuth sectors. (b) The correspondent MEX trajectory in cylindrical $X_{\text{mso}}, \sqrt{Y_{\text{mso}}^2 + Z_{\text{mso}}^2}$ coordinates. The expected average boundary positions, such as bow shock (BS) and magnetic pileup boundary (MPB), are drawn dash-dotted and dashed lines based on *Edberg et al.* [2008]. (c) Closed-up figure of MEX/IMA one full scan shown in the red box on Figure 4.1a. Interpretation of each energy-bunched ion structure including solar wind protons (H^+) and alpha particles (He^{++}), together with accelerated ring ions (picked-up protons of exospheric origin) and multiple reflected ions at the Martian bow shock [*Yamauchi et al.*, 2011] is also given. This event was reported in *Yamauchi et al.* [2012].

assume that the IMF does not significantly change over the duration of the observation cycle(s) of MEX/IMA (192 seconds). Sometimes it is necessary to integrate over several cycles to obtain better count rate statistics. For simplicity and better stability of the algorithm, we focus only on the picked-up protons with zero initial velocity, which is the one of the most intense population generated from the Martian hydrogen exospheric corona extending far beyond the bow shock [e.g., *Nagy et al.*, 1990; *Galli et al.*, 2006]. Under this assumption, we succeeded in automatically extracting ring ions from the multiple ion populations. Now we can address the large number of events semi-automatically using the fact that the ring ions form a circular trajectory perpendicular to the IMF with a radius of $|\mathbf{V}_{\text{sw}\perp}|$ in the solar wind rest frame. The concrete procedure is as follows:

- (1) The time periods of the MEX/IMA data with the ring-ion signatures are manually identified.
- (2) The solar wind bulk velocity vector is automatically derived using the observed three-dimensional ion distribution function. It is obtained as the velocity vector of the data bin in which the phase space density of solar wind ions is the highest. Data is pre-integrated over all mass channels because the light ions with lower energy ($\lesssim 700$ eV) tend to be detected regardless of the mass channels of IMA [*Barabash et al.*, 2006; *Fränz et al.*, 2006]. The noise reduction for raw data is also performed. It should be noted that all the ion counts detected in the IMA azimuth $\neq 0$ sector are neglected here, because the sector tends to collect artificial counts.
- (3) The assumption of the zero initial velocity, data bins where the ring ion component is expected to appear are selected from three-dimensional velocity distribution data. We utilize a criterion of a spherical shell in the velocity space centered at \mathbf{V}_{sw} with the radius of $|\mathbf{V}_{\text{sw}}|$, whose thickness is 15 % of $|\mathbf{V}_{\text{sw}}|$. This is about double of the energy resolution of IMA (7 %).

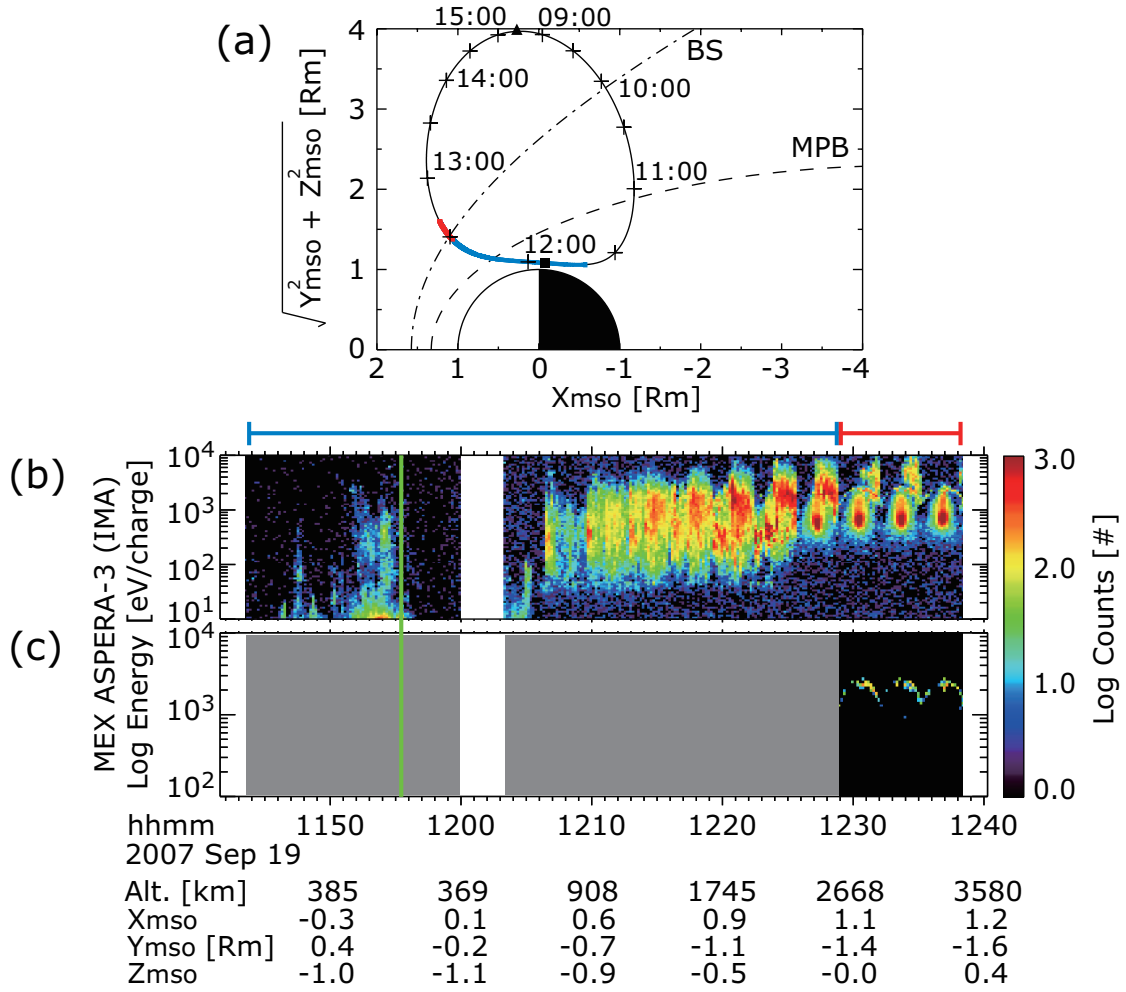


Figure 4.2: (a) The trajectory of MEX in cylindrical $X_{\text{mso}}, \sqrt{Y_{\text{mso}}^2 + Z_{\text{mso}}^2}$ coordinates on 19 September 2007. The black triangle and square indicate the locations of apoapsis and periapsis, respectively. The dash-dotted and dashed lines describe the average positions of the bow shock (BS) and the magnetic pileup boundary (MPB) [Edberg *et al.*, 2008]. The red and blue solid lines correspond to the time range shown in top of panel b. (b) Energy-time spectrogram of the ions obtained by MEX/IMA. The color code shows the ion counts integrated over all mass channels and azimuth sectors. MEX traversed the bow shock at $\sim 12:26$ UT. (c) Energy-time spectrogram automatically extracted ring ion populations between 12:29 and 12:40 UT.

Figure 4.2 shows an example of MEX/IMA observations with ring ions. The MEX position is indicated in Figure 4.2a in the Mars-centered Solar orbital (MSO)

coordinate system, where the X_{mso} axis points toward the Sun, the Z_{mso} axis is perpendicular to the planetary revolution velocity and points to the northern ecliptic hemisphere, and the Y_{mso} completes the right-hand system. The omni-directional energy-time spectrogram is shown in Figure 4.2b, which is completely same to Figure 3.1b. Ring ions were detected at approximately 1–2 keV/ q well above the solar wind protons (0.4 keV/ q) in addition to the solar wind alpha particles (~ 0.8 keV/ q) from $\sim 12:29$ UT (when MEX exited from the bow shock) until $\sim 12:40$ UT (when MEX/IMA stopped its operation). Figure 4.2c displays the result of filtering after the third step described above. Our method reasonably discriminates the ring ion component. The flux enhancement of planetary heavy ions (PHIs) is observed around periapsis (vertical green line) as seen in Figure 4.2b. *Hara et al.* [2011] revealed that the ion distribution function during this PHI enhancement signature suggests that PHIs are mostly precipitating toward the Martian ionosphere as shown in Figure 3.3. As mentioned in Chapter 3, *Hara et al.* [2011] found that PHI precipitations are not always observed, but coincide with the passages of CIRs. This tendency can be because compressed IMF strength associated with CIRs allows gyro radii of picked-up PHIs to be comparable to the Martian size.

4.2.2 Determination of IMF Orientation

Once the ring ions are extracted, determination of the IMF orientation is relatively straight forward. We simply find the unit vector normal to the plane in which the ring ion population is distributed [*Yamauchi et al.*, 2006].

We adopt the normal unit vector to determine the plane whose distance from the ring ions in velocity phase space is minimal. As an example, we apply this method to the ring ion data between 12:28:57 and 12:32:57UT, corresponding to the first full scan in Figure 4.2c.

The normal unit vector of the ring-ion plane derived for this event is $\hat{\mathbf{b}} = [-0.266, 0.963, -0.038]$ in the MSO coordinate system. Figure 4.3 represents the projected velocity distribution of the ring ion population in the newly constructed Cartesian coordinate system: B indicates the direction parallel to the $\hat{\mathbf{b}}$ derived using our method,

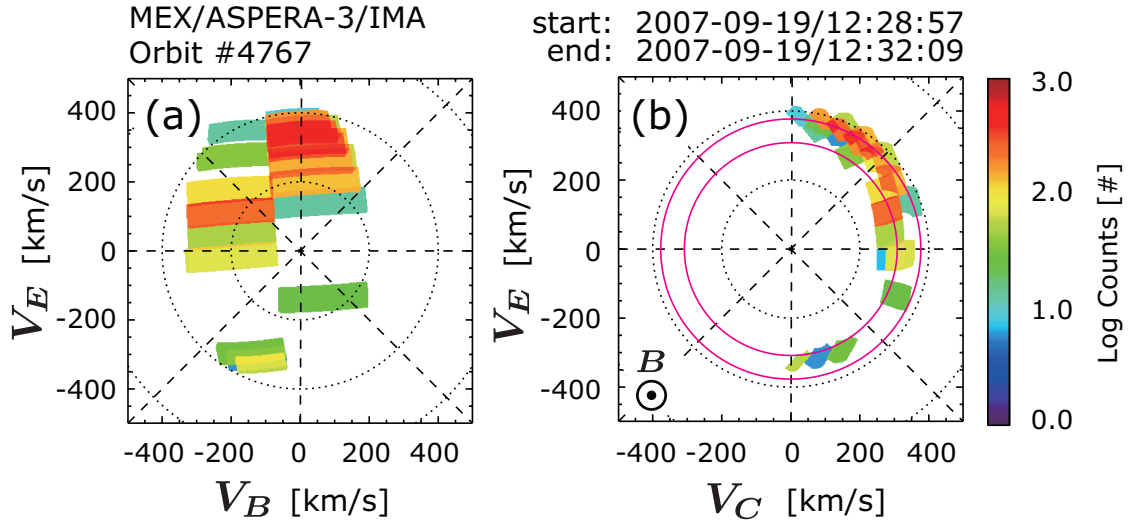


Figure 4.3: Velocity distribution function of the ring ion population observed by MEX/IMA between 12:28:57 and 12:32:08 on 19 September, 2007. The ion counts observed by MEX/IMA is projected onto the plane perpendicular to (a) the plasma convection direction and (b) the magnetic field direction in the solar wind rest frame. V_B , V_E and V_C indicate the velocity components parallel to the direction of the magnetic field unit vector ($\mathbf{b} \equiv \mathbf{B}/|\mathbf{B}|$) derived using our automated method, the convective electric field ($\mathbf{E} = -\mathbf{V}_{\text{sw}} \times \mathbf{b}$), and the plasma convection direction, ($\mathbf{E} \times \mathbf{b}$), respectively. The ion counts are integrated over the direction perpendicular to each plane. The two magenta circles in panel b indicate the shell-shaped region with radii of $|\mathbf{V}_{\text{sw}} \pm 0.1\mathbf{V}_{\text{sw}}|$ in the velocity space.

E corresponds to the direction of the solar wind electric field ($\mathbf{E} = -\mathbf{V}_{\text{sw}} \times \hat{\mathbf{b}}$), and C corresponds to the direction of plasma convection ($\mathbf{E} \times \hat{\mathbf{b}}$), and it is in the solar wind rest frame. Hereafter, we refer to this Cartesian coordinate system as the solar wind centered, magnetic field-aligned (SWB) coordinate system. The color code in Figure 4.3 is the ring ion counts, which is roughly proportional to the energy flux. It should be noted that the ion counts are accumulated in the area where the projection of the field of view (FOV) of MEX/IMA onto each plane is overlapped in the velocity phase space. We cannot determine the strength and polarity of the IMF using this method. The IMF direction can be either parallel or anti-parallel to $\hat{\mathbf{b}}$. If the IMF orientation

is anti-parallel to $\hat{\mathbf{b}}$, i.e., $\hat{\mathbf{b}} = [0.266, -0.963, 0.038]$, then the V_B and V_E axes in Figure 4.3 should have negative signs. Figure 4.3a suggests that the mean ion velocity parallel to the IMF orientation is similar to $\mathbf{V}_{sw\parallel}$. The ion counts show the partial ring distribution between the two magenta circles in Figure 4.3b, corresponding to the spheres in the velocity space with radii of $|\mathbf{V}_{sw}| \pm 0.1|\mathbf{V}_{sw}|$.

4.3 Statistical Analysis

Using the above method for estimating the IMF orientation from ring ions observed by MEX/IMA, we statistically investigate the effects of the IMF orientation on planetary heavy ions (PHIs) precipitating toward the Martian ionosphere. We surveyed the MEX/IMA data acquired between July, 2007 (Orbit # 4480) and September, 2009 (Orbit # 7265). The time interval is approximately 1 Martian year. In this study, we only focus on the PHI precipitation events observed near the MEX periapsis to investigate the behavior of precipitating ions near the ionosphere. To ensure the correct selection of the events, we excluded low quality data using the criteria of (i) minimal UV interference (low background) and (ii) no obvious interference from other instruments (e.g., MARSIS) onboard MEX. After the selection, in total, 1381 MEX periapsis crossings were analyzed. The MEX periapsis distribution is shown in Figure 4.4a in the geographic coordinate system. The number of MEX periapsis observations in the northern hemisphere with the latitude above 15° are relatively smaller and the observation is seldom around the north pole, however, the locations of MEX periapsis are distributed in both hemispheres. In addition, the solar zenith angle (SZA) at MEX periapsis (Figure 4.4b) distributes quite differently between the hemispheres owing to the MEX orbital configuration.

We then selected PHI precipitation events when the precipitating flux integrated over > 100 eV is larger than 10^5 $\text{cm}^{-2} \cdot \text{sec}^{-1}$ so as to ensure clear identification of precipitation events. The method to calculate the precipitating flux of PHIs is based on *Fränz et al. [2006]*. *Fränz et al. [2006]* proposed a standard method of calculating plasma moment derived from the velocity distribution functions of MEX/IMA. The precipitation flux can be calculated by using the IMA azimuth sectors which detected

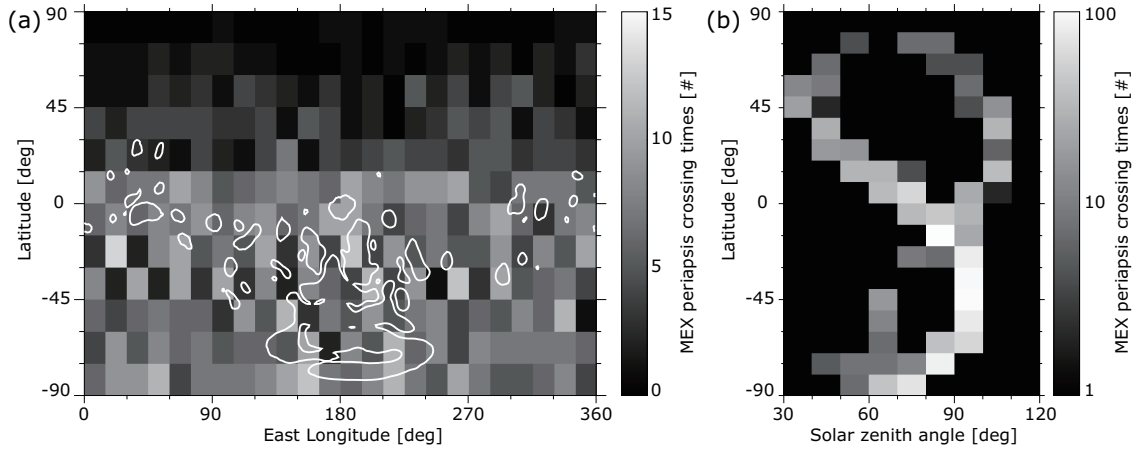


Figure 4.4: Data coverage for MEX periapsis measurements between July 2007 (Orbit # 4480) and September 2009 (Orbit # 7265). Color code shows occurrence of MEX periapsis location in (a) the geographical coordinate system; and (b) the latitude-solar zenith angle map. The crustal magnetic field contours for 20 nT magnitude are overlaid as white solid lines in panel (a).

precipitating PHIs. We can thus identify 59 precipitating PHI events. Figure 4.5a represents a geographic location distribution for the 59 identified events. Precipitating PHIs are observed both northern and southern hemispheres. Although a part of the events are observed in the vicinity of the crustal magnetic field, PHI precipitation events are not frequently observed in the southern hemisphere with the latitude between 30° and 60° , where the crustal magnetic fields are primarily concentrated. Figure 4.5b shows the SZA dependence of precipitating PHIs. This result shows that PHI precipitations are more frequently observed in the low SZA region rather than in the high SZA region. The relationship between the SZA and the crustal magnetic field magnitude are shown in Figure 4.6. The PHI precipitation events are mostly observed in the region where the modeled crustal magnetic field magnitude is small (< 25 nT at 400 km) in all SZA.

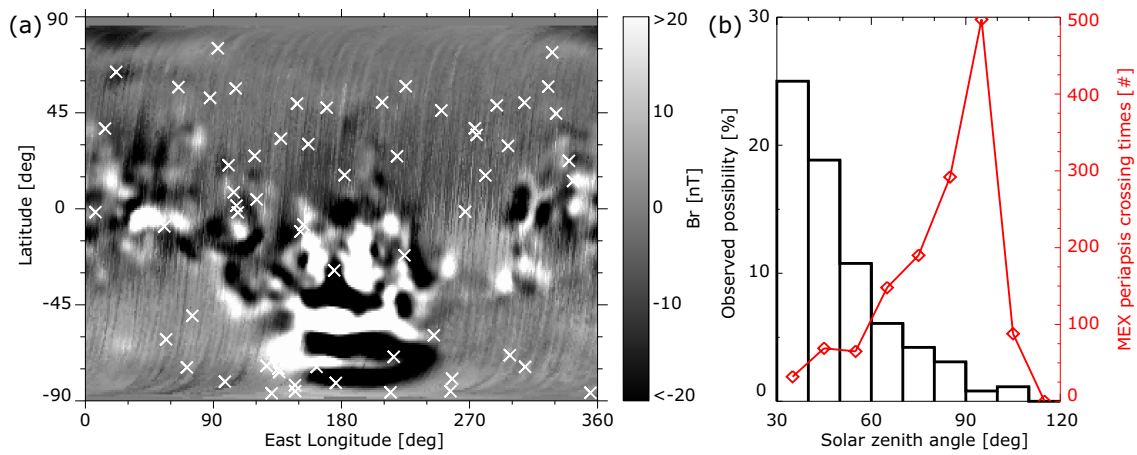


Figure 4.5: (a) Distribution of foot points of the planetary heavy-ion precipitation events observed by MEX/IMA. The grayscale background indicates the modeled radial component of the crustal magnetic field at an altitude of approximately 400 km above the Martian surface [Connerney *et al.*, 2001]. (b) Histograms of the frequency at which precipitating planetary heavy ions are observed (black) and line plot of the MEX periapsis crossing times for all the analyzed orbits (red) as a function of the solar zenith angle.

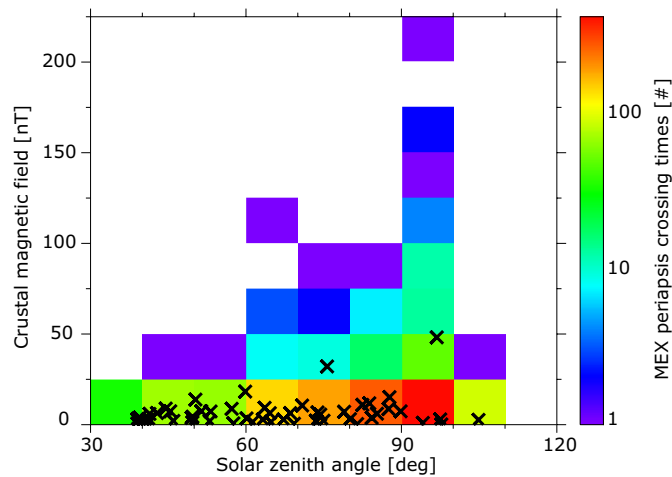


Figure 4.6: MEX periapsis location of planetary heavy-ion precipitation events (black crosses) as a function of the solar zenith angle and crustal magnetic field strength. Color code is the data density of the MEX periapsis location for all the analyzed orbits. The crustal magnetic field magnitude are derived from Connerney *et al.* [2001]. MEX observation were not available for the white area.

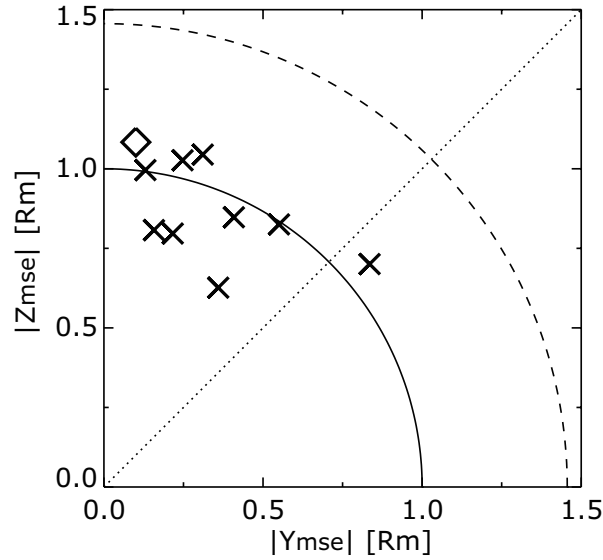


Figure 4.7: MEX positions for the 10 planetary heavy ion precipitation events for which we successfully derived the IMF orientation. The $|Y_{\text{mse}}|-|Z_{\text{mse}}|$ projection is used. The location shown as a diamond is for the orbit # 4767 (Section 4.2). The dotted diagonal line is the reference line that separates the region where observed planetary heavy ion precipitation is subject to the solar wind electric field.

Among the 59 precipitation events, we then select the events in which the ring ion population is observed within one MEX orbit. There are 10 events (including orbit #4767; Subsection 4.2.2) that satisfy this criterion, for which we estimated the IMF orientation from our method described above in Section 4.2. The estimated IMF orientations except the polarities are summarized in Table 4.1. Figure 4.7 shows the locations of these 10 precipitating PHI events in the Mars-centered, solar electrical (MSE) coordinate system, where the X_{mse} axis points toward the Sun, the Z_{mse} axis coaligns with the solar wind convective electric field, $\mathbf{E} = -\mathbf{V}_{\text{sw}} \times \mathbf{B}$ is inferred from the estimated IMF orientation and Y_{mse} completes the right-handed system. It should be noted that Figure 4.7 is displayed in the $|Y_{\text{mse}}|-|Z_{\text{mse}}|$ projection, because we cannot find the polarity of the IMF. Figure 4.7 indicates that PHI precipitation events are more somewhat aligned to the solar wind electric field (upper left) side rather than the solar wind magnetic field (lower right) side.

Table 4.1: A summary of ring ion observations and IMF orientation estimation.

Date	Time interval (UT)	IMF orientation ^a	Orbit number	Periapsis timing ^b
07 Jul. 2007	14:42:49 – 14:46:01	0.458, 0.887, 0.057	4503	13:49:53
08 Jul. 2007	10:41:51 – 10:54:39	-0.058, 0.998, 0.036	4506	09:59:26
18 Jul. 2007	19:08:41 – 19:15:05	-0.180, 0.970, 0.165	4543	18:37:32
04 Aug. 2007	10:06:32 – 10:16:08	-0.025, 0.939, -0.342	4602	07:06:10
11 Aug. 2007	21:00:12 – 21:16:12	-0.275, 0.961, -0.035	4629	20:32:42
19 Sep. 2007	12:28:57 – 12:32:09	-0.266, 0.963, -0.038	4767	11:55:26
26 Mar. 2008	06:59:36 – 07:22:00	-0.029, 1.000, -0.010	5434	06:14:30
28 Oct. 2008	10:28:02 – 10:44:02	0.522, 0.386, -0.760	6192	09:42:25
01 Feb. 2009	09:37:43 – 09:50:31	0.156, 0.986, 0.052	6528	09:12:57
25 Mar. 2009	09:35:44 – 09:38:56	-0.285, 0.447, 0.848	6709	09:06:42

^a Estimated IMF orientations without a polarity are described in the MSO coordinate system.

^b The precipitating PHI flux is calculated by using one scanning MEX/IMA data including the periapsis timing.

4.4 IMF Polarity Assessment based on Test Particle Simulation

4.4.1 Statistical Trajectory Tracings of Picked-up Exospheric Protons

One obvious question related to the Figure 4.7 is the IMF polarity. *Yamauchi et al.* [2008] suggested that estimating the IMF polarity from the MEX/IMA data might be possible for special conditions. Here we conducted a test particle simulation of picked-up protons in order to define the IMF polarity. We first calculate the trajectories of more than one million picked-up protons of exospheric origin under static and uniform solar wind conditions for two IMF possible polarities (away/toward). We then predict how the pickup ions are observed by MEX/IMA, and compare these two predictions with the MEX/IMA observation.

We employ the solar wind velocity from the MEX/IMA observations. The IMF strength is assumed to be normal (3 nT). Indeed, the results of the simulations do not

vary significantly by employing different IMF strengths. We also assumed the production rate of the pickup ions is proportional to the isotropically distributed hydrogen exosphere between the edge of the Martian bow shock and an altitude of 15,000 km from the surface with a temperature of 1,000 K [Nagy *et al.*, 1990]. Exospheric protons are produced through various processes, including photoionization, impact ionization by solar wind electrons, and charge exchange reactions with solar wind ions in the extended neutral hydrogen corona [e.g., Shizgal and Arkos, 1996].

We launch in total more than one million test particles to simulate the newly ionized hydrogen atoms of exospheric origin outside the Martian bow shock. The initial velocity of each test particle is taken to be equal to the thermal velocity of 1,000 K (~ 4 km/sec) with an isotropically distributed direction. Then we let these test particles evolve under static and uniform electromagnetic field using a fourth-order Runge-Kutta integrator until they exit through the outer boundaries ($\pm 5.5R_m$, where R_m is the Martian radius) or encounter the Martian bow shock [Edberg *et al.*, 2008]. Collisions of picked-up protons with ambient neutral particles are neglected.

We then calculate the velocity distribution function and number density (ρ) of exospheric-origin protons in each spatial bins with a spatial resolution of $\Delta x = 0.05R_m$:

$$\rho = \sum_i (F_i t_i) / \Delta x^3, \quad (4.1)$$

where Δx^3 is the volume of each cell, and F_i and t_i are mass loading rate per cell and duration spent inside the cell of the i 'th particle [e.g., Delcourt *et al.*, 2003; Yagi *et al.*, 2010]. This methodology is the same as Delcourt *et al.* [2003]; Yagi *et al.* [2010].

Figure 4.8 shows the spatial distribution of the number density of picked-up exospheric protons derived from the statistical trajectory tracing. In Figure 4.8, the IMF orientation is assumed to correspond to the vector $\hat{\mathbf{b}} = [-0.266, 0.963, -0.038]$ obtained from the MEX/IMA measurements in Subsection 4.2.2 in the MSO coordinate system. Exospheric protons picked-up by the IMF in the solar wind around Mars are accelerated by the solar wind electric field. The resultant spatial distribution is asymmetric with respect to the solar wind electric field as shown in Figure 4.8b. The hemispheric asymmetry along the Z_{mso} axis is consistent with several previous studies

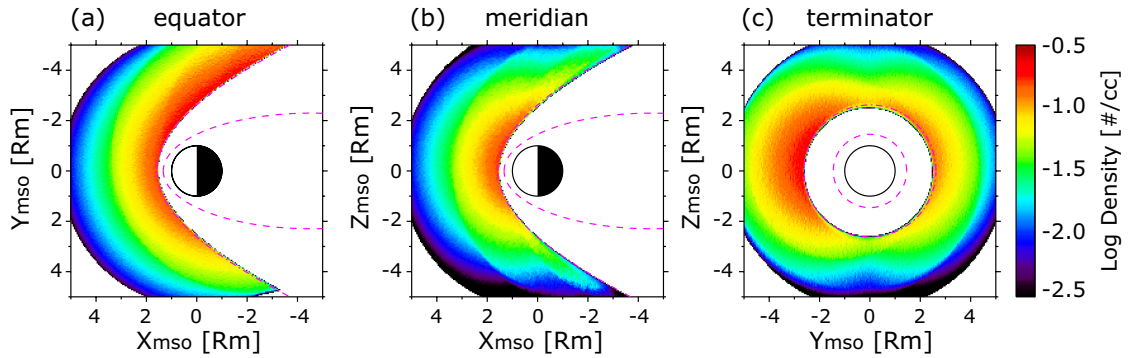


Figure 4.8: Spatial distribution of the exospheric proton number density derived from the statistical trajectory tracing under the solar wind conditions estimated for MEX orbit #4767 in Section 4.2. The each panels correspond to the (a) equator, (b) meridian and (c) terminator. The magenta dash-dotted (dashed) lines show the locations of the bow shock (the magnetic pileup boundary) following *Edberg et al.* [2008].

based on the spacecraft observations [e.g., *Barabash et al.*, 2007a; *Dubinin et al.*, 2008] and numerical simulations [e.g., *Modolo et al.*, 2005; *Fang et al.*, 2010a]. An asymmetry is also observed in the dawn-dusk direction in Figure 4.8a because the produced exospheric protons gyrate preferentially toward the dawnside because of $\mathbf{E} \times \mathbf{B}$ drift motion. The picked-up exospheric protons are therefore more likely to encounter the bow shock in the dawn sector than in the dusk sector under these conditions.

4.4.2 Comparisons of Velocity Distribution Functions between Simulated Test Particles and Observed Ring Ions

We then compare the velocity distribution functions of the simulated test particles and observed ring ions at the observation position of the ring ions by MEX/IMA. Two possible polarities (away/toward) are compared to the observation. If polarity change significantly affects the degree of agreement, we can take the polarity that results in the better agreement. As an example, the result from the event described in the Subsection 4.2.2 is shown in Figure 4.9. In this event, the location where ring ions are observed by MEX/IMA is $[1.10, -1.41, -0.03]R_m$ in the MSO coordinate system. The observed velocity distribution functions are shown in Figures 4.9a and 4.9c and

prediction by the test particle simulation are shown in Figures 4.9b and 4.9d. Figure 4.9 are projected into the $\mathbf{V}_C - \mathbf{V}_E$ plane in the SWB coordinate system. Figures 4.9a and 4.9b correspond to one polarity of the IMF (away), whereas Figures 4.9c and 4.9d correspond to the other polarity (toward). In producing Figures 4.9b and 4.9d, we took into consideration of the actual IMA FOV that is limited by the finite elevation scan angle and blockage by the spacecraft structure [e.g., *Barabash et al.*, 2006; *Futaana et al.*, 2010; *Yamauchi et al.*, 2011]. We also took into consideration of the limited proton energy range of IMA; IMA cannot detect protons with energies $\lesssim 700$ eV, and these protons are therefore also eliminated. Because of these two limitations, Figures 4.9b and 4.9d show only a partial ring instead of the full ring. Indeed, the gap seen in the partial ring is due to the blockage by the spacecraft.

If we assume the away polarity, the phase where ring ions are most densely found will be located in the first quadrant of the figures for both the MEX/IMA observation (Figure 4.9a) and the test particle simulation result (Figure 4.9b). However, these favorable phases are different for the toward polarity: the MEX/IMA observation shows the densest distribution in the fourth quadrant (Figure 4.9c) while the test particle simulation predicts the densest distribution in the first quadrant (Figure 4.9d), respectively. Thus, the away polarity (Figures 4.9a and 4.9b) reproduces the observation significantly better than the toward polarity, and therefore, we can conclude that the IMF polarity is most likely away rather than toward. The result also supports the intuitive guess of the IMF polarity suggested by *Yamauchi et al.* [2008].

If the IMF polarity is directed away, the solar wind electric field is directed from south to north. Then the precipitating location is the downward electric field hemisphere ($-Z$ in the MSE coordinate system). Indeed, the downward electric field hemisphere is a preferential hemisphere for the precipitating planetary heavy ions (PHIs) [e.g., *Luhmann and Kozyra*, 1991; *Chaufray et al.*, 2007]. However, in most events, we cannot define the IMF polarity using the test particle simulation approach, because there is no significant difference between the similarities in the velocity distribution functions for away and toward cases.

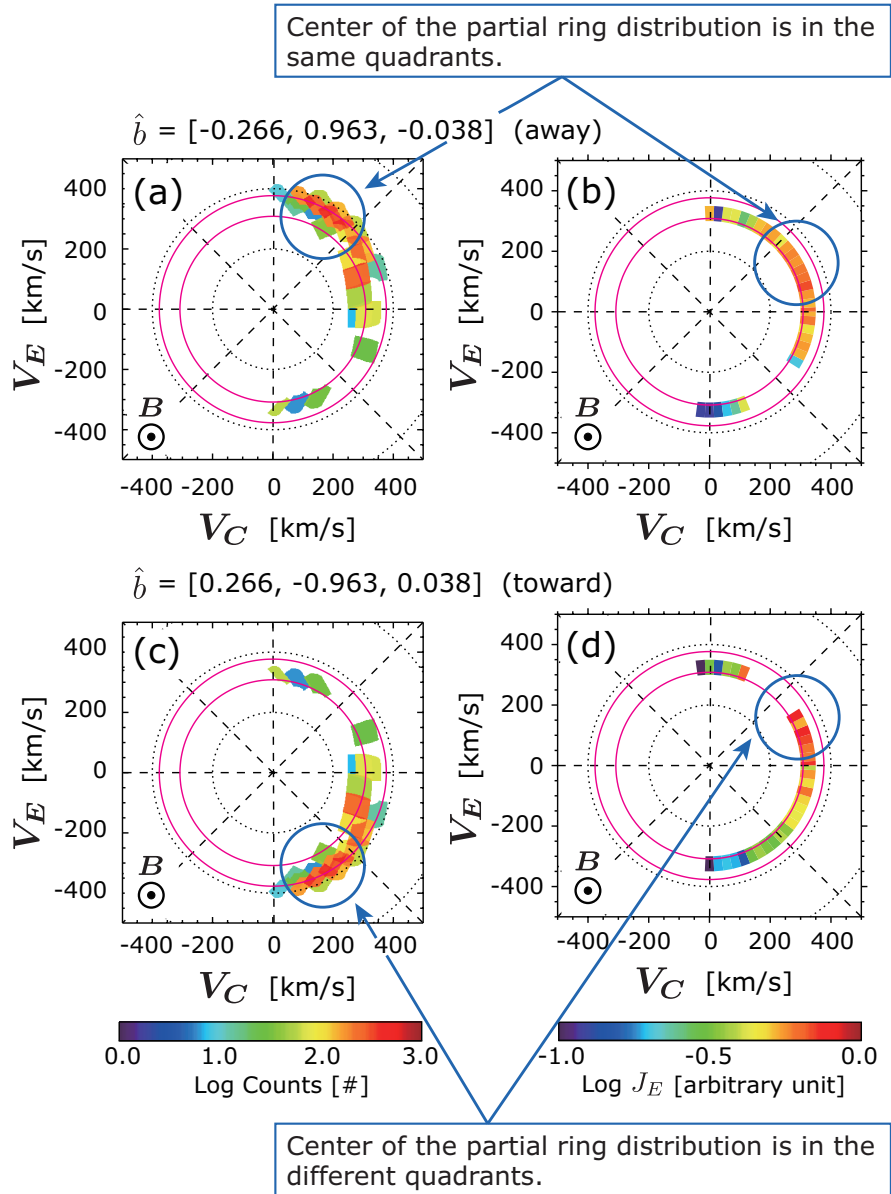


Figure 4.9: Comparison of the velocity distribution functions between the ring ion observations by MEX/IMA for panels (a) and (c) and results from test particle simulation of exospheric protons in panels (b) and (d) for the orbit # 4767. The polarities of the estimated IMF are away for panels (a) and (b) and toward for (c) and (d). The color codes for the MEX observations and the test particle simulation represent the ion counts and the energy flux, respectively. Panel (a) is identical to that in Figure 4.3b.

4.5 Discussion of Possible Ion Precipitation Mechanism

Hara et al. [2011] suggested that picked-up Martian PHIs may precipitate toward the Martian upper atmosphere during CIR passages because the gyro radius of these ions becomes comparable to the planetary size of Mars ($\simeq 3397$ km) as a result of an increase in the IMF strength. In such a condition, the spatial distribution of precipitating picked-up ions can be highly asymmetrical with respect to the convective electric field [e.g, *Luhmann and Kozyra*, 1991; *Chaufray et al.*, 2007]. *Chaufray et al.* [2007] estimated the spatial distribution of the precipitating flux of picked-up O^+ ions using their three-dimensional hybrid simulation. They found that O^+ ions with energies of a few tens of eV can only precipitate near the dayside subsolar region (Figures 3.5a and 3.5b), while precipitation flux of high energy (≥ 500 eV) O^+ ions in the downward electric field hemisphere is much larger than that in the upward electric field hemisphere, where the solar wind electric field is pointing away from Mars (Figures 3.5c and 3.5d). *Li et al.* [2011] also investigated the precipitation patterns of picked-up O^+ ions by using the test particle scheme of *Fang et al.* [2008] under an electromagnetic field from the result of the magneto-hydrodynamic (MHD) simulations of *Ma et al.* [2004]. They also demonstrated that the precipitation characteristics obtained by *Chaufray et al.* [2007] are similar between low-energy and high-energy picked-up O^+ ions. In our observation, the precipitating PHIs are frequently observed at the low SZA region (Figure 4.5b). The observed precipitating flux is also at the same order of magnitude as the predictions of *Li et al.* [2011]. These are consistent with the predictions by *Chaufray et al.* [2007] and *Li et al.* [2011]. Our obtained feature in terms of the precipitating location in the MSE coordinate system shown in Figure 4.7 might also support such previous numerical predictions.

The energy of PHI precipitations provides a clue of their origin. The observed energy is between less than 100 eV to a few keV in the vicinity of the Martian ionosphere (near the green line in Figure 4.2b). This characteristic energy is typically lower than that of the observed picked-up protons (ring ions) although O^+ is 16 times heavier

than the proton. Indeed, the maximum energy of the precipitating PHIs among all the events did not reach 10 keV. The picked-up PHIs beyond the Martian bow shock should be precipitating with energies of up to several tens of keV, corresponding to the maximum energy of the picked-up ions $((1/2)m_i(2 \cdot V_{\text{sw}})^2)$, where m_i is the mass of the PHIs. Therefore, the observed precipitating PHIs are most likely picked up from a region relatively close to the observation point such that they are accelerated only up to a few keV by the solar wind electric field. A plausible source of the observed precipitating PHIs may be the Martian magnetosheath, as illustrated in Figure 4.10.

There is a discrepancy in the occurrence of PHI precipitations between the MEX/IMA observations and numerical simulation results. Precipitation of PHIs are expected even under the normal solar wind conditions in the hybrid simulation by *Chaufray et al.* [2007]. However, we could identify only 59 events among 1381 MEX periapsis crossings during the surveyed time period. One possible factor to control the precipitating PHIs is the Martian crustal magnetic field. Because the crustal magnetic field affects the motions of the ions, the crustal magnetic field may potentially either enhance or reduce the PHI precipitation. *Li et al.* [2011] investigated the influence of the crustal magnetic field on the spatial distribution and energy deposition of precipitating picked up oxygen ions. According to their simulation, the crustal magnetic field modifies the spatial distribution of the precipitating ions, but to significantly increase the O^+ ion precipitation. Moreover, it enhances the energy deposition on the Martian nightside. Their simulation also predicted an enhancement of the ion sputtering by a factor of ~ 2 .

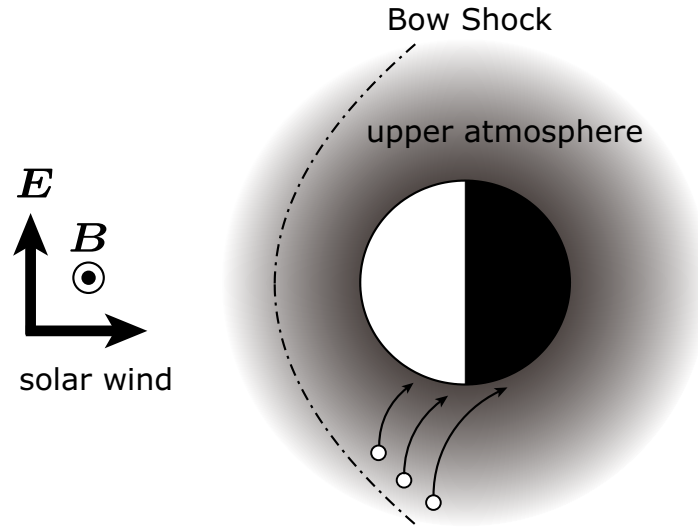


Figure 4.10: Schematic illustration of a possible scenario of planetary heavy ion precipitation events. The directions of the solar wind flow and electromagnetic (\mathbf{E} and \mathbf{B}) fields are indicated by the black solid arrows on the left side. The dash-dotted line indicates the bow shock boundary. The white circles indicate planetary heavy ions, and the trajectories of those ions are shown as black solid lines.

The story becomes opposite if the local mini-magnetosphere is formed in front of the crustal magnetic field [e.g., *Mitchell et al.*, 2001; *Lundin et al.*, 2011a]. This is not impossible because the magnetic pressure around the crustal magnetic field is sufficient to stand-off the solar wind dynamic pressure. If the mini-magnetosphere is formed, the existence of crustal magnetic field reduces the PHI precipitation around the southern hemisphere. Indeed, this scenario agrees with the low occurrence of precipitation in the southern hemisphere with the latitude between 30° and 60° (Figure 4.5a) as well as relatively high occurrence of the precipitation events where the crustal magnetic field magnitude is relatively small, such as the northern hemisphere with the latitude of $\sim 15^\circ$ (Figure 4.6). Here we should note the bias by the MEX orbit because the MEX periapsis around southern mid latitudes are mostly located on the nightside (Figure 4.4b). As shown in Figure 3.5, precipitation flux on the nightside is much smaller than that on the dayside [*Chaufray et al.*, 2007]. Therefore the lack of the event in the southern hemisphere at the latitude range between 30° and 60° might be

just caused by a biased orbital coverage.

Another possible factor that should control the behavior of the pickup ions is the IMF strength. *Hara et al.* [2011] reports that heavy-ion precipitation events often coincide with the CIR which accompanies a compressed IMF structure in front of the CIR. The enhanced IMF increases the solar wind electric field, and may effectively accelerate the picked-up PHIs, leading to more frequent detection. However, we are unable to investigate the effect of the IMF strength because of the lack of magnetic field observations by MEX. We leave the solar wind dependence and the discrepancy between the observation frequencies from the MEX/IMA measurements and numerical simulations as an open issue for future studies by the upcoming MAVEN mission or global (MHD or hybrid) numerical simulation around Mars.

The uncertainty of the estimated IMF orientation is about the half-width of the azimuth angular resolution of MEX/IMA, i.e., about 10° [*Yamauchi et al.*, 2006]. It should be noticed that the IMF estimation is made when MEX is located just outside the bow shock, and there are some time gap as well as the distortion of the IMF orientation across the bow shock. However, the distortion across the bow shock does not alter the electric field direction very much. For the temporal variability of the IMF orientation, we just refer the previous similar studies [*Yamauchi et al.*, 2011, 2012], where they estimated the IMF orientation from the ring ions for every elevation scan (192 seconds) of MEX/IMA during approximately 20–30 minutes either right after the outbound from the bow shock or right before the inbound to the bow shock. The change of the IMF orientation during these traversals were less than 20° [*Yamauchi et al.*, 2011, 2012]. Including all these uncertainties, our result of Figure 4.7 cannot be the artifact of the uncertainty of estimation of the electric field orientation.

4.6 Summary

Using the ion data from MEX/IMA, we statistically investigated the effects of the IMF orientation on planetary heavy ions (PHIs) precipitating into the Martian ionosphere. Because MEX does not carry a magnetometer, we estimated the IMF orientation from the velocity distribution function of the exospheric-origin ring-like

distributed pickup protons observed in the solar wind. The normal unit vector of the gyration plane of these protons corresponds to the direction parallel or anti-parallel to the IMF orientation. We found 59 precipitating PHI events between July 2007 and September 2009. In 10 events out of the 59 events, ring ions are also observed during the same MEX orbit. For these 10 events, we estimated the IMF orientation. These 10 events show that the precipitation of PHIs tends to be observed parallel or anti-parallel to the solar wind electric field direction (Figure 4.7). The tendency is consistent with the predictions by previous simulations [e.g., *Luhmann and Kozyra, 1991; Chaufray et al., 2007*], in which the precipitating PHIs are concentrated in the downward electric field hemisphere, where is corresponding to anti-parallel to the solar wind electric field direction.

We also tried to determine the IMF polarity for one event by comparing the ion velocity distribution functions between the MEX/IMA observation and test particle simulations that assumed both polarities. The estimated IMF polarity indicates that the PHI precipitation for that event was likely on the downward electric field hemisphere, supporting the previous numerical predictions [e.g., *Luhmann and Kozyra, 1991; Chaufray et al., 2007; Li et al., 2011*]. These results indicate that the solar wind electric field (or IMF) orientation might be estimated from the hemisphere where PHIs precipitations are observed, even though the ring ions to estimate the IMF orientation in this study are not detected. The PHI precipitation events onto the Martian upper atmosphere is less frequent above the crustal magnetic field, but this could be due to the artifact by the MEX orbit and we cannot conclude anything at moment. The observed energy of the precipitating PHIs is rather low (up to a few keV), compared to the energy of picked-up O^+ ions accelerated up to the typical solar wind velocity. These results might indicate that precipitating PHIs have been picked up in the magnetosheath rather than in the upstream solar wind outside the bow shock as summarized in Figure 4.10 [*Hara et al., 2013*].

Chapter 5

The spatial structure of Martian magnetic flux ropes recovered by the Grad-Shafranov reconstruction technique

5.1 Introduction

Although Mars lacks a global intrinsic magnetic field, it possesses strong localized crustal magnetic fields primarily located in the southern hemisphere [e.g., *Acuña et al.*, 1998, 1999] as shown in Section 1.2. Since the interplanetary magnetic field (IMF) embedded in the shocked solar wind interacts with the Martian crustal magnetic fields, the electromagnetic environment around Mars is known to be highly complicated and dynamic structure depending on space and time.

As mentioned in Section 1.5, it is thought that Martian crustal magnetic fields may influence atmospheric escape in a few different ways, based on spacecraft measurements and numerical simulations. For example, ionospheric plasma can be removed via aurora-like plasma acceleration in the vicinity of the open field line areas above the crustal magnetic fields, analogous to the Earth's polar cusp regions [e.g., *Brain et al.*, 2006b; *Lundin et al.*, 2006a; *Nilsson et al.*, 2006]. Current sheet structures ob-

served near Mars are also apparently affected by crustal magnetic fields [e.g., *Halekas et al.*, 2006, 2008; *Halekas and Brain*, 2010]. The magnetic tension force associated with current sheets is capable of accelerating ionospheric plasma away from Mars [*Dubinin et al.*, 1993]. Magnetic reconnection between crustal magnetic fields and the IMF draped around the conducting Martian ionosphere may also be responsible for ripping Martian ionospheric plasma away to space. Mars Global Surveyor (MGS) measurements found Hall magnetic field signatures associated with magnetic reconnection [*Eastwood et al.*, 2008; *Halekas et al.*, 2009]. Magnetic flux ropes and plasma clouds strongly correlated with magnetic reconnection are key phenomena, because these magnetic structures may confine large amounts of ionospheric plasma, which is then removed from the planet [e.g., *Vignes et al.*, 2004; *Brain et al.*, 2010a; *Briggs et al.*, 2011]. However, crustal magnetic fields may also prevent ionospheric plasma from escaping to space due to the formation of ‘mini-magnetospheres’ [e.g., *Mitchell et al.*, 2001; *Lundin et al.*, 2011a]. Therefore, we have not had definite conclusions of the role of the crustal magnetic fields in atmospheric escape from Mars yet.

Flux ropes are characteristic twisted magnetic field structures. The magnetic field near the center of the flux rope is strong and aligned axially, and it becomes gradually weaker and more azimuthally with distance from the center as shown in Figure 1.7 [*Russell and Elphic*, 1979]. These magnetic flux ropes have been observed throughout the solar system, e.g., at the Sun [e.g., *Okamoto et al.*, 2008; *Shiota et al.*, 2010], in interplanetary space [e.g., *Hu et al.*, 2004; *Qiu et al.*, 2007], and at the terrestrial magnetosphere [e.g., *Hasegawa et al.*, 2006]. Flux ropes have been also detected at planets, such as at Venus and Mars [e.g., *Russell and Elphic*, 1979; *Vignes et al.*, 2004], which do not possess a global intrinsic magnetic field. Moreover, *Brain et al.* [2010a] reported large-scale isolated flux ropes filled with Martian ionospheric plasma located downstream from strong crustal magnetic fields, based on vector magnetic field and suprathermal electron measurements from MGS. *Morgan et al.* [2011] reported on the longevity of similar events based on a combination of MGS data and field magnitudes derived from the ionospheric radar sounding experiment (MARSIS) onboard Mars Express (MEX). These flux ropes could intermittently carry significant large amounts of atmosphere away from Mars via a bulk removal process such as mag-

netic reconnection between the IMF and crustal magnetic fields. *Brain et al.* [2010a] proposed that this process might account for as much as 10 % of the total present-day ion escape from Mars. However, it is difficult to evaluate an atmospheric escape rate due to the Martian flux ropes from single spacecraft data, because there is ambiguity in estimation of the shape and size of the observed flux ropes.

There have been attempts to estimate the shape and size of flux ropes detected using from single spacecraft data by solving the Grad-Shafranov (GS) equation. This technique enables the reconstruction of the magneto-hydrostatic spatial structure from the particle and field data, under the assumption that the structure is two-dimensional and time-independent [e.g., *Sturrock*, 1994; *Sonnerup and Guo*, 1996]. The Grad-Shafranov reconstruction (GSR) technique has been used to recover various magneto-hydrostatic structures, such as the Earth’s magnetopause [e.g., *Hau and Sonnerup*, 1999; *Hasegawa et al.*, 2004, 2005], flux ropes observed in interplanetary space (often known as magnetic clouds) as shown in Figure 5.1 [e.g., *Hau and Sonnerup*, 1999; *Hu and Sonnerup*, 2002], as well as flux ropes observed in Earth’s magnetosphere (often called a flux transfer event) as shown in Figure 5.2 [e.g., *Sonnerup et al.*, 2004; *Hasegawa et al.*, 2006].

In this chapter, we applied the GSR technique to Martian flux ropes observed by MGS in order to estimate their shape and size. Using their reconstructed spatial structures, we then impose constraints on their shape and size to assess the escape rate associated with removal of ions via magnetic flux ropes propagating away from the planet. The assumptions used in applying the GSR technique are shown in Section 5.2. Results for a typical magnetic flux rope event are presented in Subsection 5.3.2. A statistical analysis of 135 Martian magnetic flux ropes is shown in Section 5.4. In Section 5.5, we estimate the ionospheric plasma content inside the reconstructed flux rope structures. Finally in Section 5.6, we summarize the results, and discuss the potential effects of the flux ropes on the atmospheric escape from Mars.

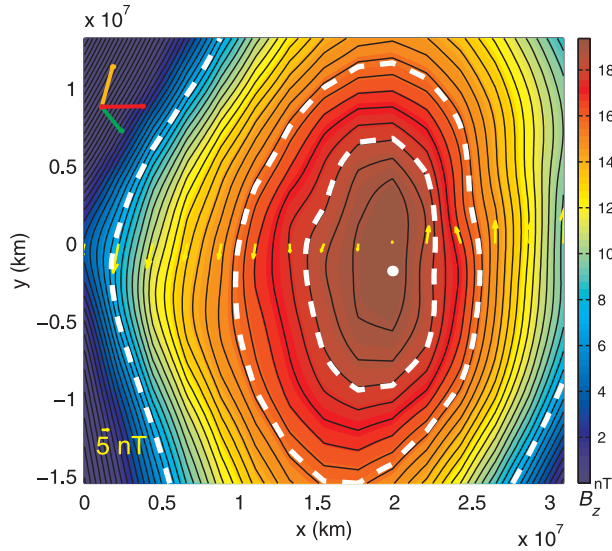


Figure 5.1: GSR results of two-dimensional axial (B_z) magnetic field map of the magnetic cloud event measured by WIND satellite on October 18, 1995 [Hu and Sonnerup, 2002]. WIND satellite placed around the L1 Lagrange point, upstream of Earth to monitor the solar wind properties around Earth. Yellow arrows at points along $y = 0$ are measured transverse magnetic field vectors. The white dot in the center denotes the point where the axial field B_z is a maximum, that is, is the center of the magnetic cloud. The white dashed contour lines surrounding the center of the magnetic cloud are reference lines of the magnetic cloud boundary (See Hu and Sonnerup [2002] for methodology to define these boundaries). Line segments in the upper left corner are projection of GSE (Geocentric Solar Ecliptic) unit vectors: X (red), Y (green), and Z (yellow), onto the $x - y$ plane. This is reproduced from Figure 9c in Hu and Sonnerup [2002].

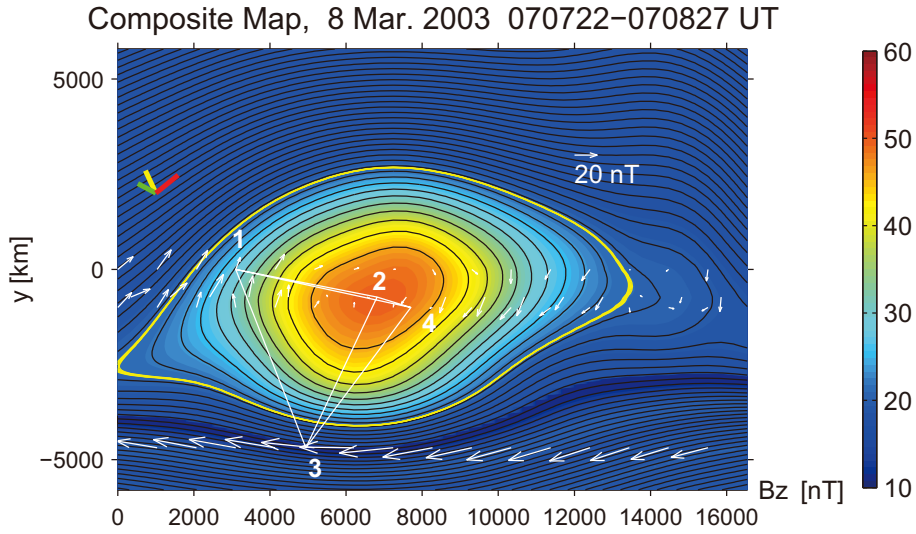


Figure 5.2: GSR results of two-dimensional axial (B_z) magnetic field map of the flux transfer event measured by Cluster spacecraft near the Earth northern cusp region on March 8, 2003 [Hasegawa *et al.*, 2006]. Cluster spacecraft are orbiting around Earth in a tetrahedral formation to survey Earth’s magnetosphere. The figure format is mostly same to Figure 5.1. Cluster tetrahedron and measured transverse magnetic field, $\mathbf{B}_t = (B_x, B_y)$, are shown in white. This is reproduced from top panel of Figure 3 in Hasegawa *et al.* [2006].

5.2 Grad-Shafranov Reconstruction (GSR)

5.2.1 Assumptions

The Grad-Shafranov reconstruction (GSR) technique can be applied under the following conditions: (i) The structure is approximately in magneto-hydrostatic equilibrium, i.e., inertial effects are negligible; (ii) The structure is two-dimensional, i.e., there is a so called invariant axis z , along which spatial gradient of the structure is much smaller than in the other directions, x and y , perpendicular to the z direction. This assumption is equivalent to $\partial/\partial z \ll \partial/\partial x, \partial/\partial y$; (iii) The structure is approximately time-independent.

Plasma moment (e.g., density, velocity vector, temperature) and magnetic field data are necessary to recover the two-dimensional magneto-hydrostatic spatial configuration of the observed flux ropes. Because MGS lacked ion measurements, a few

additional assumptions must therefore be provided. A typical plasma density and temperature of the Martian ionosphere at the spacecraft altitude (~ 400 km) [Fox, 2009] are assumed in order to calculate the input thermal pressure for the model. It is also assumed that the observed flux ropes are approximately stationary, which means that the spacecraft velocity, \mathbf{V}_{sc} , is the dominant component causing apparent movement of the flux rope relative to the MGS spacecraft. This assumption is supported by results of *Morgan et al.* [2011] and of *Beharrell and Wild* [2012]. Considering a typical duration of the flux ropes and \mathbf{V}_{sc} , the curvature of the spacecraft trajectory is small and is ignored in this study.

We tested the sensitivity assumptions described above, and found no significant influence of the plasma density and temperature on the results, within ordinary conditions. If the flux ropes are moving anti-sunward with velocity of 5–15 km/sec, as assumed by *Brain et al.* [2010a], their estimated volumes will depend on the angle that the spacecraft trajectory makes with the flux rope axis. Our results presented in the following sections are not significantly influenced by this assumption as long as we only discuss an order estimation, because their volumes do not vary by as much as an order of magnitude.

5.2.2 Application Procedures

In the GSR technique, we assume the following force balance in the MHD framework:

$$\mathbf{j} \times \mathbf{B} = \nabla p, \quad (5.1)$$

where \mathbf{j} is the current density, \mathbf{B} is the magnetic field, and p is the plasma thermal pressure. This equation describes the condition that the magnetic tension is balanced with the force from the total pressure gradient. The GS equation in the Cartesian coordinate system (x, y, z) can be described as follows [see, e.g., *Sturrock*, 1994; *Hau and Sonnerup*, 1999]:

$$\frac{\partial^2 A}{\partial x^2} + \frac{\partial^2 A}{\partial y^2} = -\mu_0 \frac{dP_t}{dA}, \quad (5.2)$$

where the vector A is the magnetic vector potential, such that $A(x, y)$, and P_t is the transverse pressure defined as $P_t = (p + B_z^2/2\mu_0)$, which is the sum of the plasma

thermal and axial field pressures. The magnetic field vector can be expressed by using the magnetic vector potential A ,

$$\mathbf{B} = \left[\frac{\partial A}{\partial y}, -\frac{\partial A}{\partial x}, B_z(A) \right]. \quad (5.3)$$

The axial magnetic field B_z as well as the plasma pressure p , are functions of A alone. Therefore the transverse pressure P_t and the axial current density, which is given by $j_z = dP_t(A)/dA$, are also uniquely determined as a function of A . The values of A along the x axis, which is the projection of the spacecraft trajectory onto the $x - y$ plane, can be calculated from the observed magnetic field component, B_y via the spatial integration,

$$A(x, 0) = \int_0^x \frac{\partial A}{\partial \xi} d\xi = - \int_0^x B_y(\xi, 0) d\xi. \quad (5.4)$$

Since we assume the observed flux ropes are stationary in this study, the spatial integration $d\xi$ can be transformed into the time integration via the following relation, $d\xi = \mathbf{V}_{sc} \cdot \hat{\mathbf{x}} dt$, where $\hat{\mathbf{x}}$ is the unit vector along the projection of \mathbf{V}_{sc} onto the plane perpendicular to the invariant axis $\hat{\mathbf{z}}$.

The invariant axis direction $\hat{\mathbf{z}}$ is determined by trial and error on the basis of the requirements that $P_t(A)$ and $B_z(A)$ should be single-valued functions of A . Once we can calculate the values of $A(x, 0)$ from the equation (5.4), the transverse pressures along the spacecraft trajectory, $P_t(x, 0)$, can also be obtained. A residue as defined by *Hu and Sonnerup* [2002] evaluates the deviation of $P_t(x, 0)$ versus $A(x, 0)$ from a single-valued function. As a result, the z axis is singled out as the direction for which the residue is minimum among all calculated values associated with all possible trial directions. We calculate the right-hand side of the GS equation (5.2) using the single-valued function in all regions of the $x - y$ plane threaded by field lines crossing the trajectory. In terms of other parts of the $x - y$ plane, the field should be recovered via suitable extrapolations of the function $P_t(A)$.

Once the function $P_t(A)$ has been determined, the integration of the GS equation (5.2) is conducted as follows: observed magnetic field components, B_x and B_y at each point along the spacecraft trajectory are used as initial values. New A and B_x values at grid points away from the x axis by small steps, $\pm\Delta y$, are calculated via

the GS equation (5.2). The integration is performed to complete a two-dimensional magnetic vector potential map of $A(x, y)$. The details of the integration procedures are extensively described in previous studies [e.g., *Hau and Sonnerup, 1999; Hu and Sonnerup, 2002*].

5.3 Application to Martian Flux Ropes

5.3.1 Identification of Magnetic Flux Ropes in MGS data

We selected large magnetic flux ropes from MGS MAG data during the mapping phase between 1999 and 2006 to apply the GSR technique. We chose candidate events in which the observed magnetic field strength exceeded the value expected from a crustal magnetic field model [*Cain et al., 2003*] by 70 nT or more. We then selected as flux ropes the events for which hodograms obtained from minimum variance analysis (MVA) of the observations show a partial rotation in the plane perpendicular to the minimum variance axis for which the eigenvalue ratio between the intermediate and minimum variance directions exceeded 5. It is because the observed magnetic field vectors rotate along the spacecraft trajectory on the MVA coordinates system as illustrated in Figure 5.3 [e.g., *Russell and Elphic, 1979; Elphic et al., 1980*]. We identified 135 clear magnetic flux rope events from the MGS data, similar to the result of the event search mentioned in *Brain et al. [2010a]*.

5.3.2 September 24, 1999 Event

Figure 5.4 shows an overview of magnetic field observations recorded by MGS on September 24, 1999. An enhancement of the magnetic field strength was observed during 03:21:55–03:34:55UT (between two magenta vertical lines in Figure 5.4a). The magnetic field strength reached a peak of approximately 120 nT at 03:30:25UT. The crustal magnetic field model [*Cain et al., 2003*] is shown by the red solid line in Figure 5.4a. It indicates that the expected crustal field strength is much smaller (less than 10 nT) than the observed field strength. The hodograms for this event (Figure 5.5) in the MVA coordinate system clearly show that the vector magnetic

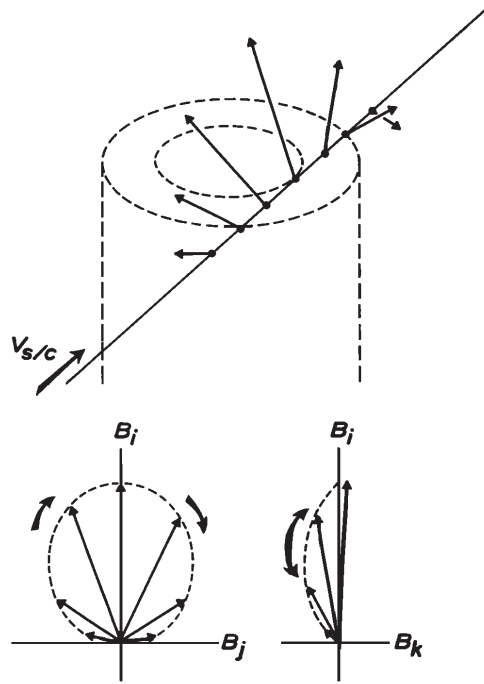


Figure 5.3: Schematic illustration of magnetic field rotation sampled by spacecraft passing through a flux rope and its hodograms in the MVA coordinate system, where B_i , B_j , and B_k component refer to the maximum, intermediate, and minimum variance axis, respectively. Reproduced from *Elphic et al.* [1980].

field rotates in a circular manner in the plane perpendicular to the minimum variance axis during the enhancement of observed field strength. This vector magnetic field rotation as described in Figure 5.5a is a feature of the magnetic flux rope, which are similar to Figure 5.3. The intermediate to minimum eigenvalue ratio is 26.05, which is much larger than our event selection criterion. We thus infer that this magnetic field enhancement is due to a magnetic flux rope.

The spatial structure of the magnetic flux rope is estimated by the GSR technique described in Section 5.2, using the observed vector magnetic field during the event. An optimal invariant z axis is determined to be $[-0.94, -0.15, -0.30]$ in the Mars-centered, Solar Orbital (MSO) coordinate system. The MSO coordinate system is defined with the X_{mso} axis toward the Sun, the Z_{mso} axis perpendicular to the ecliptic pointing to the northern hemisphere, and the Y_{mso} axis completing the right-hand system. Figures 5.6a and 5.6b show the transverse pressure P_t and axial magnetic field B_z as a function

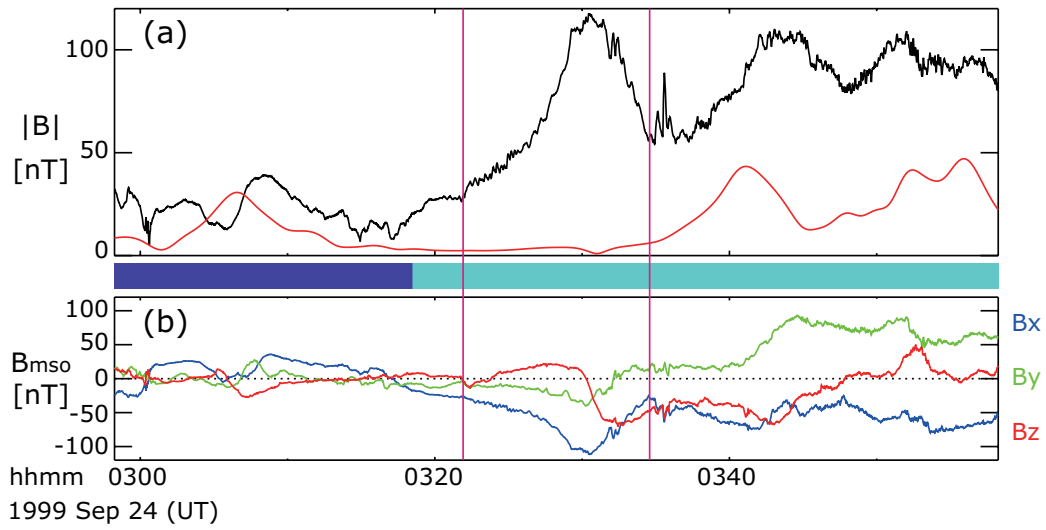


Figure 5.4: Time series plots of (a) magnetic field magnitude and (b) vector magnetic field, in the Mars-centered Solar Orbital (MSO) coordinate system, as observed by MGS on September 24, 1999. Expected crustal magnetic field magnitude is shown by the red solid line in Figure 5.4a. Color bar between Figures 5.4a and 5.4b indicates whether MGS was illuminated (light blue) or in eclipse (dark blue). MGS observed a magnetic flux rope during the time interval between two magenta vertical lines.

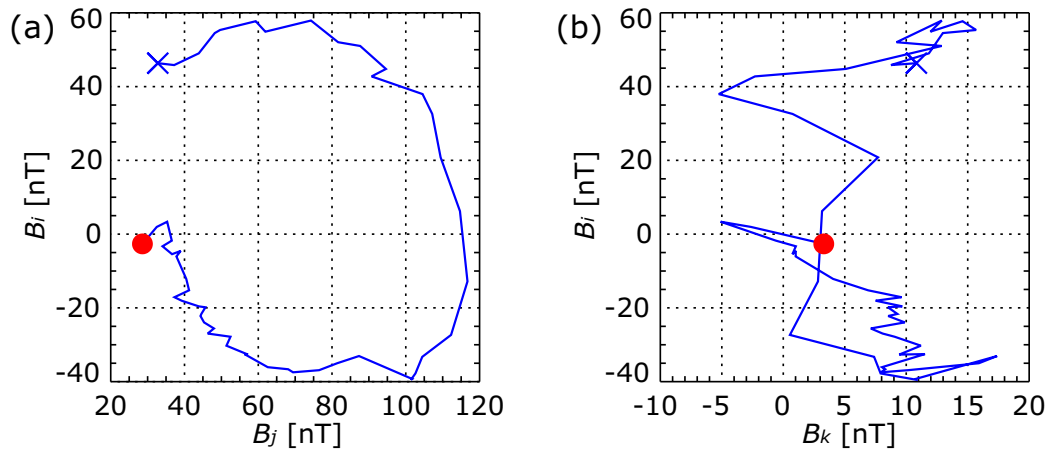


Figure 5.5: Hodograms of the magnetic flux rope event observed by MGS between 03:21:55–03:34:34 UT on September 24, 1999 in the MVA coordinate system. The format is mostly same to lower panels of Figure 5.3. Red circles (blue crosses) are start (stop) points, respectively.

of magnetic vector potential A . The observed structure turns out to be approximately two-dimensional, because the observed data points (solid circles) are well-fit by single curves (solid curves) as described in Subsection 5.2.2. The right parts of the Figures 5.6a and 5.6b, where the fitted curves have only one branch and the vector potential is large, correspond to the core part of the magnetic flux rope. In contrast, the left parts correspond to the regions away from the core part of the magnetic flux rope. The slope of the fitted curves, $dP_t(A)/dA$, characterizes the spatial structure of the reconstructed magnetic flux rope, because it reflects the axial current, $j_z(A)$. The line on the left side of the panel is simply taken to be horizontal, which means that there is no axial current; this assumption has no significant influence on the reconstructed structure [Hasegawa *et al.*, 2006]. Figure 5.6c shows the optimal magnetic field map in which magnetic field lines in the $x - y$ plane are shown by black curves and the axial (z) magnetic field component is colored. The MGS spacecraft was travelling along the x direction from left to right at $y = 0$. The reconstructed spatial structure is not circular, but somewhat elliptic elongated to the direction roughly perpendicular to the MGS spacecraft trajectory. The overlaid magenta dashed curve on Figure 5.6c is our determined boundary to estimate the volume of the magnetic flux rope. The definition of the magnetic flux rope boundary in this study is described later in Section 5.5.

5.4 Statistical Properties of Magnetic Flux Ropes

We applied the Grad-Shafranov reconstruction (GSR) technique to the 135 magnetic flux rope events selected in Subsection 5.3.1. Among the 135 events, we could uniquely and clearly determine the invariant axis for 70 events, and reconstruct the spatial structure of the magnetic flux ropes.

Figure 5.7 represents relations between the duration of the magnetic flux ropes and the solar zenith angle (SZA) for all the 135 events. The color shows the averaged upstream crustal magnetic field strength derived from *Connerney et al.* [2001]. The upstream crustal magnetic field strength is calculated as the averaged value of the crustal magnetic field model from the observed location to the subsolar point along

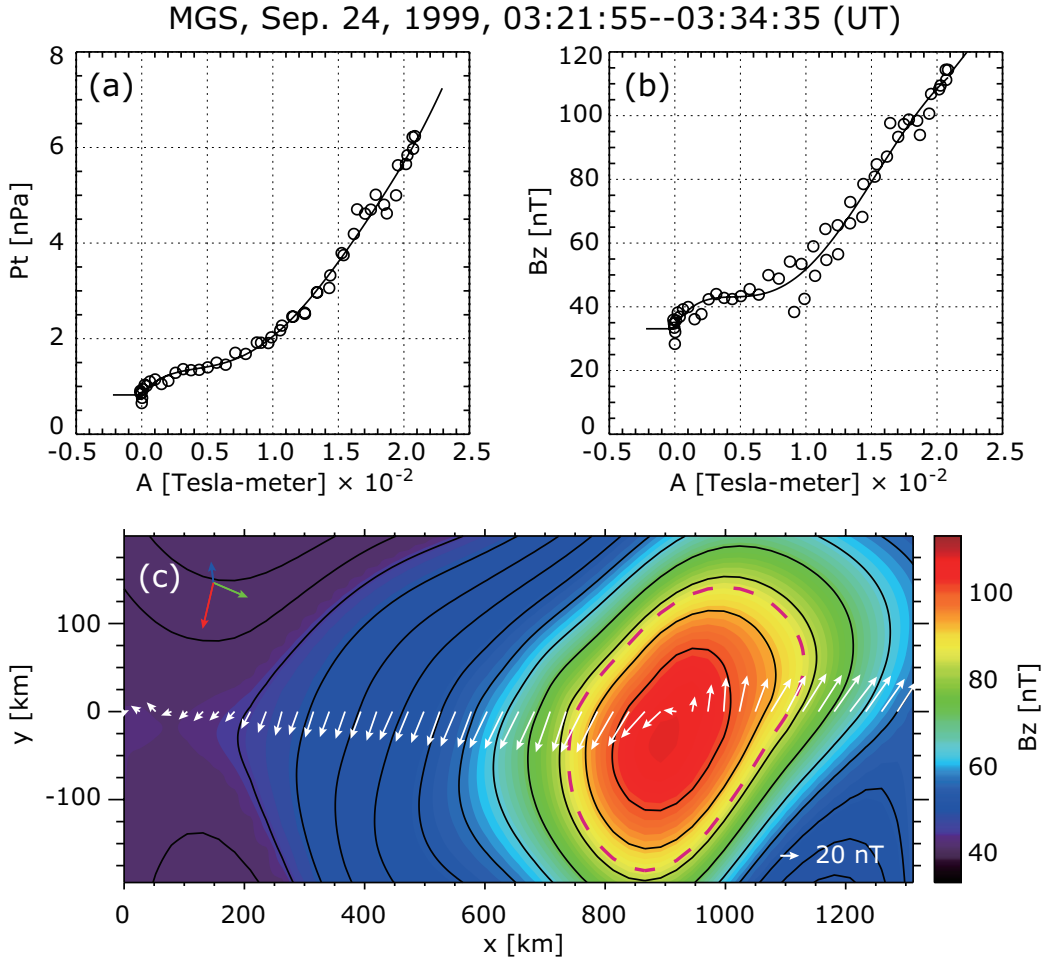


Figure 5.6: Results from the Grad-Shafranov reconstruction using MGS data. (a) Transverse pressure ($P_t = p + B_z^2/2\mu_0$) and (b) axial magnetic field B_z , plotted as a function of the partial magnetic vector potential A . Open circles are the MGS observations and thick solid curves denote the fitted polynomials. (c) The reconstructed transverse field lines with B_z in color. The MGS spacecraft was traveling (time progressed) from left to right along the line $y = 0$. White arrows represent the transverse magnetic field components measured by MGS. The blue, green, and red arrows are the projections of the MSO axes, respectively.

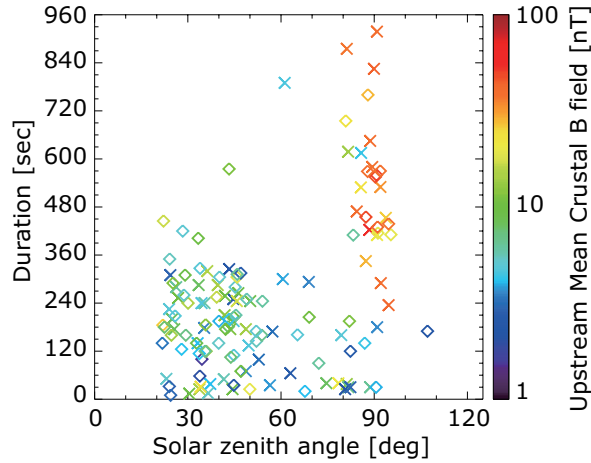


Figure 5.7: Scatter plot of the duration versus solar zenith angle of the observed magnetic flux ropes for all the 135 selected events. Symbols are colored by the averaged upstream crustal magnetic field strengths calculated based on the results of *Connerney et al.* [2001]. The symbol of diamonds (crosses) indicates the events in which their spatial structures could (could not) be estimated from the Grad-Shafranov reconstruction.

the typical plasma streamline. Because MGS made no ion measurements, the typical plasma streamline is defined as the shortest route flowing from the subsolar point to the nightside. The flow direction is obtained as follows: If the MGS spacecraft position is given by \mathbf{R} in the MSO coordinate system, the unit vector of flow direction $\hat{\mathbf{f}}$ is given by

$$\hat{\mathbf{f}} \equiv \left(\frac{\hat{\mathbf{X}}_{\text{mso}} \times \mathbf{R}}{|\hat{\mathbf{X}}_{\text{mso}} \times \mathbf{R}|} \right) \times \left(\frac{\mathbf{R}}{|\mathbf{R}|} \right), \quad (5.5)$$

where $\hat{\mathbf{X}}_{\text{mso}}$ is the unit vector along the X_{mso} axis, that is, along the Mars-Sun direction. The flow direction $\hat{\mathbf{f}}$ is assumed to be symmetrical with respect to the subsolar point, and has no radial component except at the subsolar point. This assumption of the flow direction $\hat{\mathbf{f}}$ is also employed by *Strangeway and Russell* [1996]. It is clearly shown in Figure 5.7 that the expected upstream crustal magnetic field strength is relatively large for the events in which the SZA is high ($> 75^\circ$) and the duration is long (> 240 sec).

Figure 5.8 is a scatter plot similar to Figure 5.7, however represents the GSR results

for the 70 events in which we could recover their spatial structures. Figure 5.8a shows that the axes of magnetic flux ropes are mostly horizontal to the Martian surface. This tendency of their magnetic flux rope axis estimated from the GSR technique is similar to the results of magnetic flux ropes previously seen in the dayside Venus ionosphere above ~ 200 km altitude from the surface [Elphic and Russell, 1983a]. Figure 5.8b shows that the angle of the magnetic flux rope axes with respect to the typical plasma streamline is rather randomly distributed.

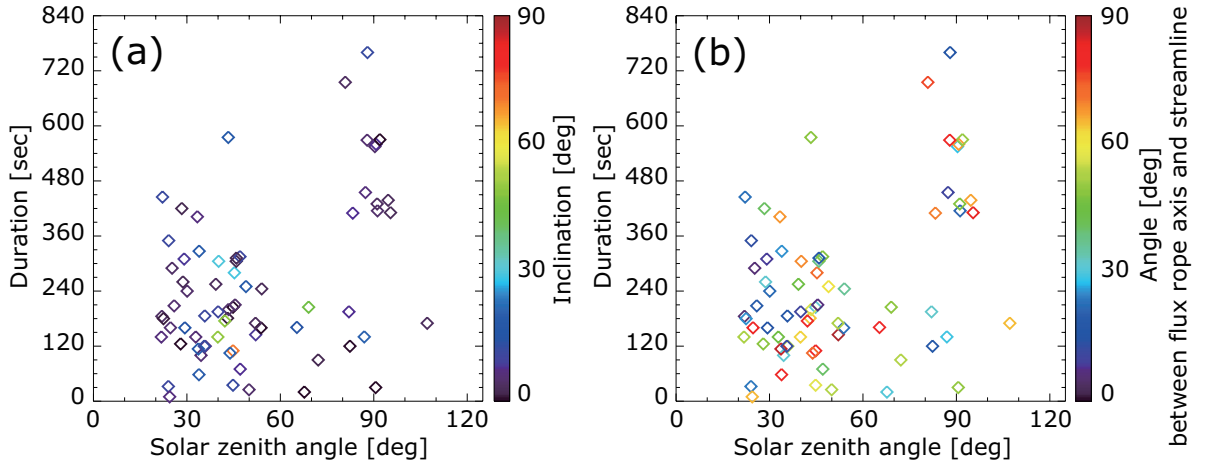


Figure 5.8: Scatter plots of the magnetic flux rope events in which their spatial structures could be recovered by the Grad-Shafranov reconstruction technique. The format is the same as in Figure 5.7. Symbols are colored by the values of (a) the inclination of the magnetic flux rope axis relative to the Martian surface: 0° (90°) is horizontal (vertical) to the Martian surface at the foot point of MGS, and (b) the angle between the flux rope axis and the typical plasma convection streamline. The definition of the direction of the typical plasma convection streamline is given in the text.

The spatial structure could be recovered for 12 events which are observed at SZA larger than 75° with duration longer than 240 sec. These 12 events are mostly observed in the region where the upstream crustal magnetic field strength is relatively large (Figure 5.7). The geographic distribution for those 12 events is shown in Figure 5.9. These large magnetic flux ropes are mostly observed downstream from the strong crustal magnetic field in the southern hemisphere, similar to the previous reported

large-scale isolated magnetic flux ropes [Brain *et al.*, 2010a; Morgan *et al.*, 2011; Beharrell and Wild, 2012]. One exception is the event in which the averaged upstream crustal magnetic field strength is the weakest among these 12 events. We hereafter categorize the remaining 11 events in which the observed locations are clustered downstream from the strong crustal magnetic field into ‘Event category A’ throughout in this chapter. On the other hand, the rest of events whose spatial structures could be recovered from the GS reconstruction technique, regardless of their location or duration, are referred to as ‘Event category B’.

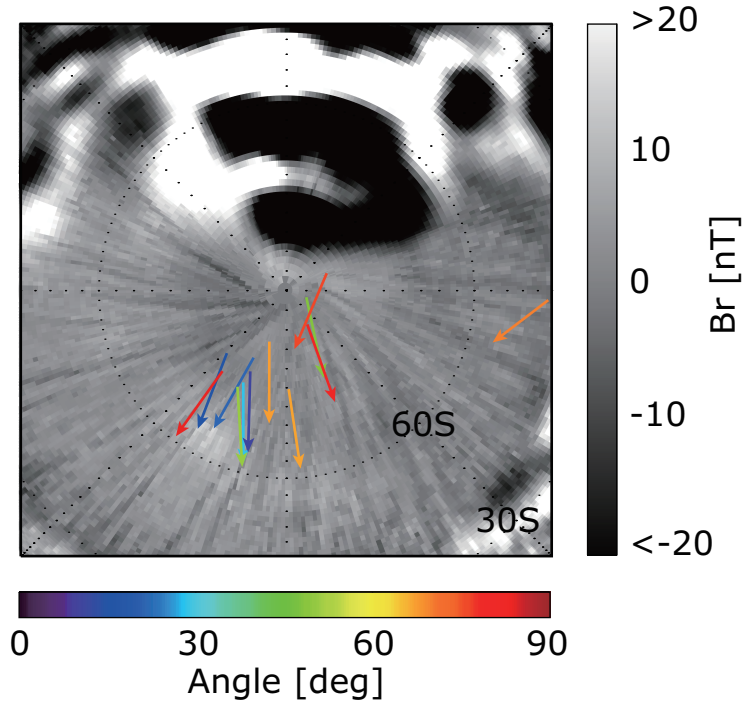


Figure 5.9: The geographic location, viewed from above the south pole in the geographic coordinate system of the long duration and high solar zenith angle events for which the spatial structure of the magnetic flux ropes was successfully recovered. Grayscale background indicates the radial component B_r of crustal magnetic fields expected at the altitude of about 400 km from the Martian surface [Connerney *et al.*, 2001]. Arrows show the direction of the typical plasma convection streamline derived from Equation (5.5). The arrow colors represent the angle of the recovered magnetic flux rope axes relative to the direction of the typical plasma convection streamline.

5.5 Magnetic Flux Rope Size Estimation

In this section, we estimate the shape and size of the magnetic flux rope, based on their spatial structures estimated from the Grad-Shafranov reconstruction (GSR) technique. In this study, we defined a flux rope boundary via transforming the two-dimensional axial (B_z) magnetic field data of Figure 5.6c into Figure 5.10 in the following steps:

- (1) The axial magnetic field strength at the center of the magnetic flux rope is generally strongest. Hence, the reconstructed two-dimensional axial (B_z) magnetic field data of Figure 5.6c is uniformly shifted so that the axial magnetic field strength of the data bin furthest from the center of the magnetic flux rope is zero, i.e., the magnetic field strength at the center of the reconstructed magnetic flux rope is shifted to be strongest.
- (2) Normalization is performed for the shifted two-dimensional axial (B_z) magnetic field so that the magnetic field strength at the center of the magnetic flux rope is one.
- (3) The boundary of the recovered magnetic flux rope is defined as a flux surface where the shifted two-dimensional axial (B_z) magnetic field strength normalized at the center of the magnetic flux rope is 66 %.

An example of the boundary determination is shown with the magenta dashed curve in Figures 5.6c and 5.10. This boundary definition might underestimate the flux rope size. However, our defined boundary is completely within the reconstructed two-dimensional axial magnetic field map for 48 events among the 70 events in which their spatial structures can be estimated from the GSR technique. Therefore, we could at least assess lower limits of the volume of the observed magnetic flux ropes based on this boundary determination.

We also investigated the probability of observing photoelectrons when MGS traversed the interior of the reconstructed magnetic flux ropes. Photoelectrons are a good proxy for whether the observed magnetic flux ropes contain Martian ionospheric

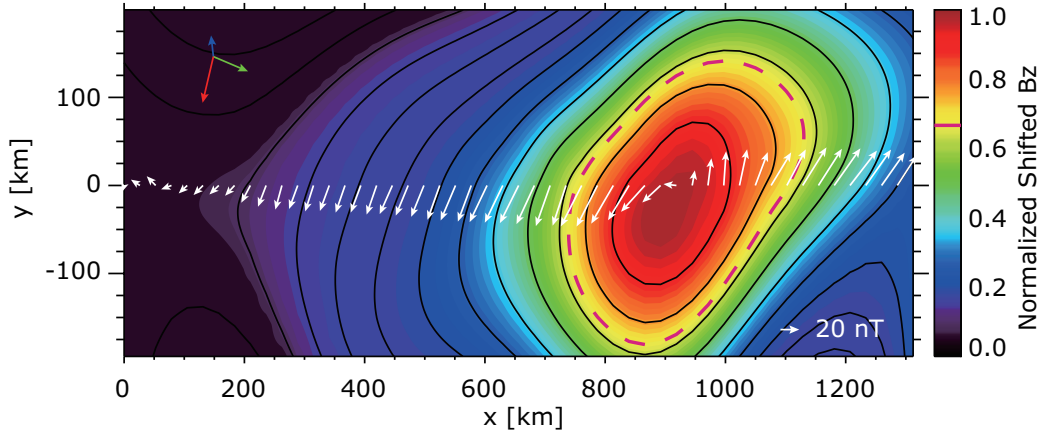


Figure 5.10: The map of the reconstructed axial magnetic field B_z , shifted and normalized in the following way. The format is mostly same as in Figure 5.6c. Here, two-dimensional axial magnetic field data are shifted so that the axial magnetic field value is zero on a field line furthest from the center of flux rope, and then the shifted values are normalized by the shifted axial field value at the center of magnetic flux rope. The dashed magenta line is the boundary of the flux rope, defined as a surface where the shifted axial magnetic field strength is 66 % of the core field value.

plasma. Photoelectrons have been detected by the ER experiment onboard MGS with energies of about 20 eV [e.g., *Mitchell et al.*, 2001] and ~ 500 eV (oxygen auger electrons) [*Mitchell et al.*, 2000]. In this study, we only surveyed the 53 events (including 11 Event category A and 42 Event category B) in which MGS stayed inside our defined boundary for a time interval long enough to sample at least one electron energy spectrum. The resulting photoelectron observation probability is 90.9 % and 58.0 % for Event categories A and B, respectively. This result indicates that photoelectrons are more frequently observed for Event category A than for Event category B, even though Event category A is observed at relatively larger SZA regions than Event category B, as seen in Figures 5.7 and 5.8. High solar zenith angles could correspond to lower photoelectron production, and therefore lower rates of observation. We infer that Event category A consists of flux ropes filled with ionospheric plasma.

We then estimate the cross section of the recovered magnetic flux ropes for the 53 recovered events mentioned above. The equivalent radius is derived from the

estimated cross section, under the assumption that the shape of each flux rope is strictly circular. It ranges from ~ 30 – 341 km and ~ 19 – 670 km in Event categories A and B. The estimated equivalent radii vary by a factor of 10 among the 53 recovered events. The length along the flux rope axis is estimated from the MGS flight distance. We assume that the reconstructed spatial structure is maintained at least over the time interval when MGS was inside the magnetic flux rope. The axial length is in the range ~ 31 – 575 km for Event category A and ~ 3 – 456 km for Event category B, respectively.

Table 5.1: A summary of an equivalent radius and a stretched length of the reconstructed magnetic flux ropes and photoelectron observation probability for Event categories A and B.

Event Category	A	B
Photoelectron observation probability [%]	90.9 ± 17.5	58.0 ± 44.4
Equivalent radius [km]	149.2 ± 115.0	134.0 ± 115.3
Stretched length [km]	212.4 ± 145.7	110.6 ± 94.0

The averaged values for flux rope shape and photoelectron observation probability for Event categories A and B are summarized in Table 5.1. We note again that our defined boundary for a recovered magnetic flux rope might be partially beyond the reconstructed two-dimensional frame. Hence, the estimated values of the equivalent radius and axial strength are underestimated in some of the events.

Once lower limits of their volume are calculated, we can estimate lower limits on the ionospheric plasma content contained inside the flux ropes. The radar sounder MARSIS onboard the Mars Express (MEX) spacecraft provides us with the local electron density profile in the Martian ionosphere [e.g., *Gurnett et al.*, 2005]. The electron density derived from the MARSIS instrument around the MGS altitude (~ 400 km from the surface) is expected to be typically between 10^2 – 10^4 cm^{-3} depending on the observed SZA between 30° – 120° [e.g., *Gurnett et al.*, 2008; *Morgan et al.*, 2008]. In this study, we adopt the typical ionospheric plasma density to be 10^3 cm^{-3} . The resultant lower limits on the ionospheric plasma content inside the magnetic flux ropes

range between 1.7×10^{23} – 4.8×10^{25} (6.7×10^{24} on average) ions and between 1.9×10^{22} – 4.5×10^{25} (2.9×10^{24} on average) ions in Event categories A and B, respectively.

5.6 Summary and Discussion

In this chapter, we investigated the spatial structure of Martian magnetic flux ropes observed by MGS by applying the Grad-Shafranov reconstruction (GSR) technique. We succeeded in recovering their spatial structures for 70 obvious magnetic flux rope events. The results indicated that the magnetic flux rope axes are mostly oriented horizontal to the Martian surface (Figure 5.8a), and are rather randomly distributed with respect to the typical plasma streamline (Figure 5.8b). We found that the events observed at SZA larger than 75° with duration longer than 240 sec are mostly seen in the region where the upstream crustal magnetic field strength is large (Figure 5.7). This is because the observed geographic location corresponds to the region downstream from the strong crustal magnetic field in the southern hemisphere, as shown in Figure 5.9. In this thesis, we defined these characteristic events as Event category A. We calculated lower limits on the volume of the recovered flux ropes, based on the shape and size obtained from the GSR technique. The estimated volumes vary by 2–3 orders of magnitude among the recovered events.

If we assume that the ionospheric plasma inside the flux ropes is completely removed from the Martian upper atmosphere within the duration that MGS samples each structure, ion escape rates can be estimated by dividing the ionospheric plasma content inside the flux rope by the duration of the events. The estimated escape rates are on the order of 10^{22} – 10^{23} ions/sec for Event category A, because the observed durations are typically a few minutes. This escape rate is approximately 10 % of the global average ion escape rate (integrating all escape processes) during solar minimum [e.g., *Barabash et al.*, 2007a; *Lundin et al.*, 2008a]. Our estimates are approximately comparable to the results of *Brain et al.* [2010a], even though our estimation of the flux rope length is shorter than that of *Brain et al.* [2010a]. However, *Brain et al.* [2010a] assumed that the magnetic flux rope is moving with the 5–15 km/s plasma flow velocity relative to the MGS spacecraft.

As mentioned in Section 5.4, we could reconstruct the spatial structure of 70 magnetic flux ropes among the identified 135 events, i.e., we could not reliably determine the invariant axis for 65 events. It might indicate that some of the assumptions used in the GSR technique are invalid for these 65 events. Possible candidates include spatial structures that are not two-dimensional but three-dimensional, or structures that were evolving in time. Interestingly, we could not uniquely determine the invariant axis in the event reported by *Brain et al.* [2010a].

In this study, the typical plasma streamline derived via Equation (5.5) is simply assumed to be the shortest route flowing from the subsolar point to the nightside, because MGS lacks ion measurements. However, *Lundin et al.* [2011a] reported that flow directions of planetary oxygen ions (O^+) in the vicinity of the Martian ionosphere around the south pole show complicated patterns, based on their statistical study of the MEX ion observations. Hence, simultaneous spacecraft observations of vector magnetic field as well as ionospheric ion flow directions are important to investigate the actual relationship between the flux rope axis obtained from the GS reconstruction and the local plasma streamline.

The association of large-scale magnetic flux ropes with the region downstream from strong crustal magnetic fields indicates that crustal magnetic fields play a role in their formation. *Brain et al.* [2010a] inferred from the observed time variations of the electron pitch angle distribution that the upstream crustal magnetic field had been stretched tailward from the dayside via interaction with the solar wind, and had been detached (Figure 5.11). In the meanwhile, *Beharrell and Wild* [2012] reported that MGS frequently detected magnetic field enhancements associated with magnetic flux ropes in the terminator region in the Martian southern hemisphere, when the strong crustal magnetic fields are distributed upstream. They pointed out that the flux rope can be formed by internal reconnections between neighboring crustal magnetic field lines, whereby field lines are stretched and overlay neighboring crustal magnetic field lines (Figure 5.12). The resultant flux rope remains attached to the crust [*Beharrell and Wild*, 2012]. In both *Brain et al.* [2010a] and *Beharrell and Wild* [2012], the flux rope axes should be approximately either parallel or anti-parallel to the polarity inversion line between crustal magnetic fields. This tendency is partially consistent

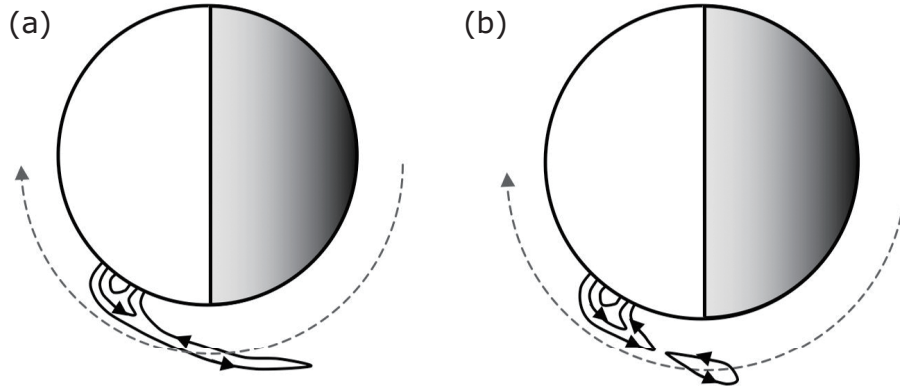


Figure 5.11: Cartoon of possible field line geometries for the magnetic flux rope reported by *Brain et al.* [2010a]. The Sun is to the left, and the MGS orbital trajectory is shown as a dashed gray line, with the spacecraft moving from right to left. (a) Crustal magnetic field lines are still attached to the surface, and have been stretched tailward long distances by the solar wind. (b) Magnetic closed loop can be formed by magnetic reconnection between crustal magnetic field lines. It can detached from the surface, carrying ionospheric plasma away from Mars. Reproduced from *Brain et al.* [2010a].

with our GS reconstruction results (warm colored arrows for Event category A in Figure 5.9). However, our GS reconstruction results have some exceptions, suggesting that there may be multiple flux rope formation mechanisms associated with the crustal magnetic fields. Another factor potentially responsible for flux rope formation is magnetic reconnection between the interplanetary magnetic field (IMF) draping around Mars and the crustal magnetic field as suggested by *Brain et al.* [2010a]. Investigation of IMF effects on the flux rope formation thus should be important to understand their formations [*Hara et al.*, 2014].

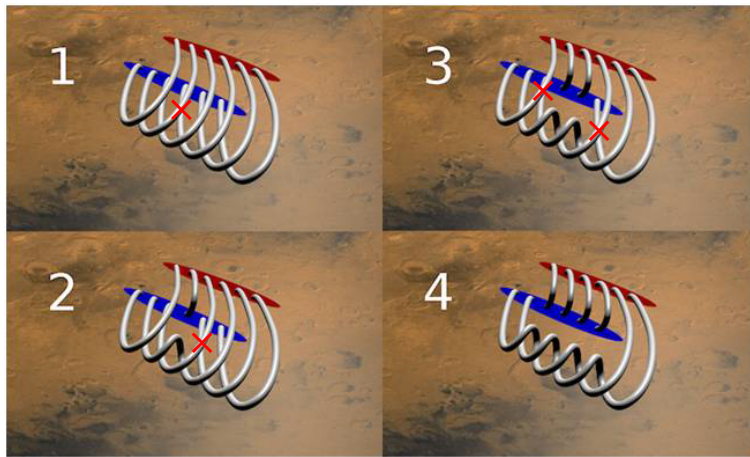


Figure 5.12: Schematic illustration of the possible formation scenario of the magnetic flux rope proposed by *Beharrell and Wild* [2012]. It can be formed via magnetic reconnection between neighboring crustal magnetic field lines. Reproduced from *Beharrell and Wild* [2012].

Chapter 6

Formation processes of Martian flux ropes downstream from crustal magnetic fields deduced from Grad-Shafranov reconstruction

6.1 Introduction

As mentioned in Chapter 5, magnetic flux ropes are characteristic twisted helical magnetic field structures, which have been observed throughout the solar system, including at the Earth's magnetosphere [e.g., *Sonnerup et al.*, 2004; *Hasegawa et al.*, 2006], in interplanetary space [e.g., *Hu et al.*, 2004; *Qiu et al.*, 2007], and at the Sun [e.g., *Okamoto et al.*, 2008; *Shiota et al.*, 2010]. Flux ropes have been also detected at the other terrestrial planets, such as at Venus [e.g., *Russell and Elphic*, 1979], Mars [e.g., *Vignes et al.*, 2004], and recently at Mercury [*Slavin et al.*, 2009].

Statistical properties of flux ropes detected at unmagnetized planets have been extensively investigated based on the PVO measurements for Venus [e.g., *Luhmann and Cravens*, 1991, and references therein]. A large number of flux ropes had been ubiquitously observed in the dayside Venus ionosphere [e.g., *Russell and Elphic*, 1979; *Elphic and Russell*, 1983b,a]. Flux ropes in the dayside Venus ionosphere were de-

tected during approximately 70 % of the PVO orbits [*Elphic and Russell*, 1983a]. PVO measurements provided several possible formation processes of flux ropes seen in the Venus ionosphere. For example, *Wolff et al.* [1980] proposed viscous-type plasma instabilities like the Kelvin-Helmholtz (KH) instability as the origin of Venus flux ropes observed at the interface between the solar wind flow and ionosphere in the moderate and/or high solar zenith angle region, because a part of draped magnetic field lines sank from the magnetosheath, and twisted in the ionosphere owing to the KH instability. *Elphic and Russell* [1983c] pointed out that a helical kink instability which coiled flux ropes themselves could be responsible for their random axis orientations derived from the results of *Elphic and Russell* [1983a]. *Luhmann and Elphic* [1985] suggested that flux ropes are the result of a kinematic dynamo process acting on weak seed fields in the Venus ionosphere. However, there is no direct evidence to demonstrate those proposed possible formation scenarios for the observed flux ropes at the dayside Venus ionosphere. No matter which proposed possible formation processes are responsible for the origin of the Venus flux ropes, they are originated by the interplanetary magnetic field (IMF) and an associated draped magnetic field lines around Venus.

In the case of Mars, the IMF and associated draped magnetic field lines may not be the only origin of Martian magnetic flux ropes, because Mars possesses strong localized crustal magnetic field [e.g., *Acuña et al.*, 1998]. The existence of crustal magnetic fields and their spatial distribution were extensively investigated by the magnetometer onboard Mars Global Surveyor (MGS) [e.g., *Acuña et al.*, 1999; *Connerney et al.*, 2005]. The electromagnetic environment around Mars is thus expected to be more complicated than Venus, since the solar wind plasma and IMF interact with the Martian upper atmosphere as well as localized crustal magnetic fields. Magnetic flux ropes in the Martian upper atmosphere had been also discovered by MGS [e.g., *Cloutier et al.*, 1999; *Vignes et al.*, 2004]. Flux ropes similar in spatial scale to those observed at Venus are reported at Mars [e.g., *Vignes et al.*, 2004; *Briggs et al.*, 2011], though they are less frequently observed than at Venus [*Vignes et al.*, 2004]. Furthermore, large-scale isolated flux ropes associated with crustal magnetic fields are also found in the downstream of strong crustal magnetic fields [e.g., *Brain et al.*, 2010a;

Morgan et al., 2011]. *Beharrell and Wild* [2012] statistically investigated the spatial distribution of those large-scale magnetic flux ropes based on an automated detection method of the flux ropes from MGS data. They found that the enhancements of magnetic field amplitude mostly associated with flux rope signatures were concentrated at solar zenith angles (SZAs) between 90° and 100° in the southern hemisphere. Moreover, such events are repeatedly detected, when the strong crustal magnetic fields are located on the dayside, upstream of the southern pole region [*Beharrell and Wild*, 2012].

As described in Section 5.6, the possible formation processes of these large-scale magnetic flux ropes associated with strong crustal magnetic fields have been proposed by several authors. *Brain et al.* [2010a] proposed based on the observed time variations of the electron pitch angle distribution that the upstream crustal magnetic field is stretched tailward from the dayside via interaction with the solar wind, and may detach, similar to plasmoids in Earth’s magnetotail. *Beharrell and Wild* [2012] pointed out that the flux rope can be formed by internal reconnections between neighboring crustal magnetic field lines, whereby field lines are stretched and overlay neighboring crustal magnetic field lines.

If the flux ropes detach, they could intermittently carry significant large amounts of atmosphere away from Mars via a bulk removal process such as magnetic reconnection between the IMF and/or crustal magnetic fields. Therefore, the flux ropes detached from the unmagnetized planets are expected to play an important role in ion escape. *Brain et al.* [2010a] proposed that this process might account for as much as 10 % of the total present-day ion escape from Mars. In the previous chapter, we estimate lower limits on the potential ion escape rate due to these large-scale magnetic flux ropes by using the Grad-Shafranov reconstruction (GSR) technique, which is capable of reconstructing the two-dimensional magneto-hydrostatic structure from single spacecraft data [e.g., *Sturrock*, 1994; *Hu and Sonnerup*, 2002; *Hasegawa et al.*, 2006]. The estimated lower limit on the ionospheric plasma content inside 70 large-scale magnetic flux rope events turns out to be between 1.7×10^{23} – 4.8×10^{25} ions [*Hara et al.*, 2014]. Since the observed durations that MGS samples each flux rope structure are typically a few minutes, *Hara et al.* [2014] estimated escape rates to be

on the order of 10^{22} – 10^{23} ions/sec, which is also approximately 10 % of the global average ion escape rate during solar minimum. The GSR results provide us with various spatial characteristics, including their shape (lower limits of their radii and lengths), axial orientation, and chirality (handedness) of the flux rope magnetic fields.

In this chapter, we focus on investigating possible formation scenarios of large-scale magnetic flux ropes observed downstream from the strong crustal magnetic fields in the Martian southern hemisphere, based on the GSR results. In Section 6.2, we show the method for identifying the large-scale magnetic flux ropes observed downstream from the strong crustal magnetic fields between April 1999 and November 2006. In Section 6.3, the GSR technique is applied to the identified magnetic flux rope candidates derived from the selected orbits in Section 6.2. We conduct a statistical study, categorizing the identified large-scale magnetic flux ropes into 4 types according to the characteristics of their axial orientation estimated from the GSR in Section 6.4. We also investigate dependencies of such magnetic flux ropes on the external conditions, such as solar wind dynamic pressure and the local external draped magnetic field direction. In Section 6.5, we examine the previously proposed formation scenarios and propose a new formation scenario based on the GSR results. Finally in Section 6.6, we summarize indications from the obtained results and discuss the potential ion escape rate due to these large-scale magnetic flux ropes.

6.2 Identification of Magnetic Flux Ropes Candidates from MGS Data

We also utilize data obtained from the magnetometer and electron reflectometer (MAG/ER) onboard Mars Global Surveyor (MGS) during the mapping phase in order to identify Martian magnetic flux ropes. Since the MGS orbital periods were approximately 2 hours, MGS rotated around Mars $\sim 34,200$ times in total during the mapping phase. In this study, we surveyed magnetic flux ropes identified in MGS magnetic field data between April 1999 and November 2006.

Beharrell and Wild [2012] reported that MGS had repeatedly detected the enhancements of magnetic field strength mostly associated with flux rope signatures around the South Pole downstream from the strong crustal magnetic fields, based on their automated method. We defined criteria to select candidate MGS orbits in terms of the geographic locations and the solar zenith angle to systematically search for magnetic flux ropes associated with crustal magnetic fields: When MGS was near the terminator at the solar zenith angles between 85° and 95° , we selected for the following conditions:

- (i) MGS was located between -120° and 60° East longitude, and $70^\circ - -90^\circ$ South latitude.
- (ii) Upstream average crustal magnetic field along the typical plasma streamline is larger than 15 nT.
- (iii) Magnetic field data were available.

The typical plasma streamline is assumed to be the shortest route flowing from the subsolar point to the nightside, as defined by several previous authors [*Hara et al.*, 2014; *Strangeway and Russell*, 1996]. Based on Equation (5.5), the upstream crustal magnetic field strength is calculated as the averaged value of the crustal magnetic field model from the observed location to the subsolar point along the typical plasma streamline, which is also identical to the method of *Hara et al.* [2014].

Through the selection criteria, we selected 3,007 candidate orbits to survey magnetic flux ropes. Figure 6.1 shows the average direction of the typical plasma streamline for each orbit, binned and averaged as seen from the Martian southern pole. Figure 6.1 indicates that our criteria single out the appropriate orbits to investigate magnetic flux ropes downstream from the strong crustal magnetic fields. It should be noted that the typical plasma streamline (arrows of Figure 6.1) mostly directs from the subsolar point to the nightside. This is why the local time of geographic map, viewed from above the south pole as Figure 6.1, is corresponding to the dayside around 180° , the nightside around 0° , the dawnside around 90° , and the duskside around 270° of the east longitude, respectively.

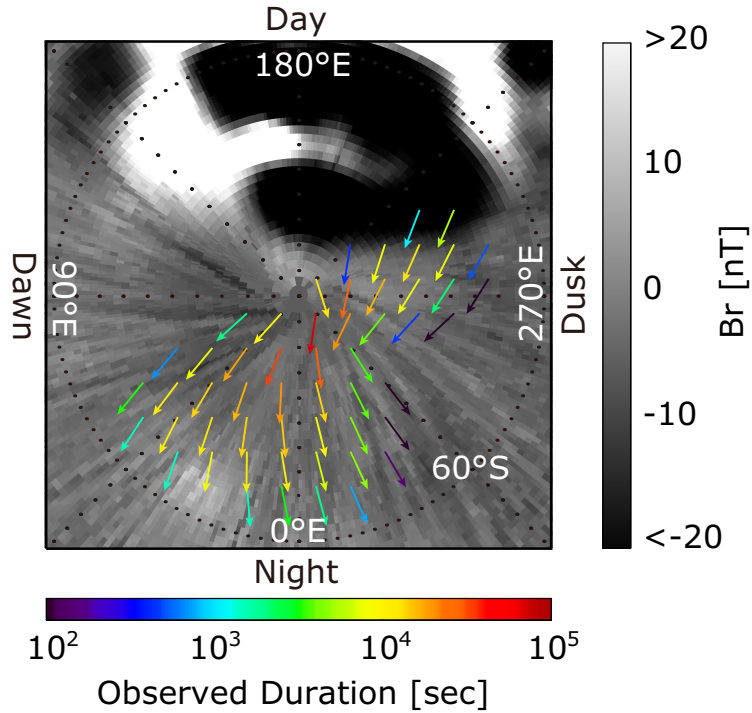


Figure 6.1: The average direction of the plasma streamline of the 3,007 orbits utilized so as to conduct our statistical study of magnetic flux ropes, viewed from above the south pole. Grayscale background indicates the radial component B_r of crustal magnetic fields expected at the altitude of about 400 km from the Martian surface [Connerney *et al.*, 2001]. The arrow colors represent the total duration of observation accumulated over 3,007 orbits. The definition of the direction of the typical plasma streamline is given in the text.

We then surveyed whether large magnetic flux ropes were recorded in MGS MAG data among the selected orbits. The time interval surveyed corresponds to between ± 10 minutes from when the orbit selection criteria were fulfilled. We first chose candidate events in which the observed magnetic field strength was enhanced by 20 nT over the value expected from a crustal magnetic field model [Cain *et al.*, 2003]. We then selected flux rope events in which magnetic field hodograms obtained from minimum variance analysis (MVA) show a partial rotation in the plane perpendicular to the minimum variance axis as well as in which the eigenvalue ratio of the intermediate to minimum variance directions exceeded 5 to ensure an approximate planar configuration. By the selection method, we identified 682 magnetic flux ropes from the MGS

data in the selected 3,007 orbits.

6.3 Application of Grad-Shafranov Reconstruction to Magnetic Flux Rope

We estimated the flux rope axial orientation and the spatial structure of the identified 682 magnetic flux ropes, based on the Grad-Shafranov reconstruction (GSR) technique, assuming that their structures are two-dimensional and magneto-hydrostatic. Since their structures are assumed to be two-dimensional, we are able to determine the invariant axis along which spatial gradient of the structure is much smaller than in the other directions. The invariant axis is parallel to the flux rope axis for the structure [e.g., *Hau and Sonnerup, 1999; Hu and Sonnerup, 2002*]. The detailed methodology to determine the invariant axis and to apply the GS reconstruction technique to Martian magnetic flux ropes observed by MGS is completely identical as described in Section 5.2. It should be noticed again that the definition of the invariant axis as the z axis of the GSR coordinate system. The direction of the invariant (GSR z) axis is defined so that transverse magnetic field rotation (in GSR $x - y$ plane) perpendicular to the flux rope axis (z) obeys the right-handed screw rule in this study. The GSR x axis is defined to be parallel to the projection of the spacecraft velocity, \mathbf{V}_{sc} , onto the GSR $x - y$ plane. The GSR y axis completes the right-handed orthogonal system. Hence, the GSR x axis (at $y = 0$) represents the projection of the spacecraft trajectory onto the GSR $x - y$ plane.

Among the selected 682 magnetic flux ropes in the previous section, we were able to uniquely and clearly determine the invariant axis for 297 events and reconstruct the spatial structure of the magnetic flux ropes. Hereafter, we utilize these 297 events in order to further investigate the formation processes of magnetic flux ropes observed downstream from the strong crustal magnetic field. Figure 6.2 represents the geographic distribution of 297 magnetic flux rope events, viewed from above the Martian south pole. Observed magnetic flux ropes are concentrated between 0° and 45° East longitude.

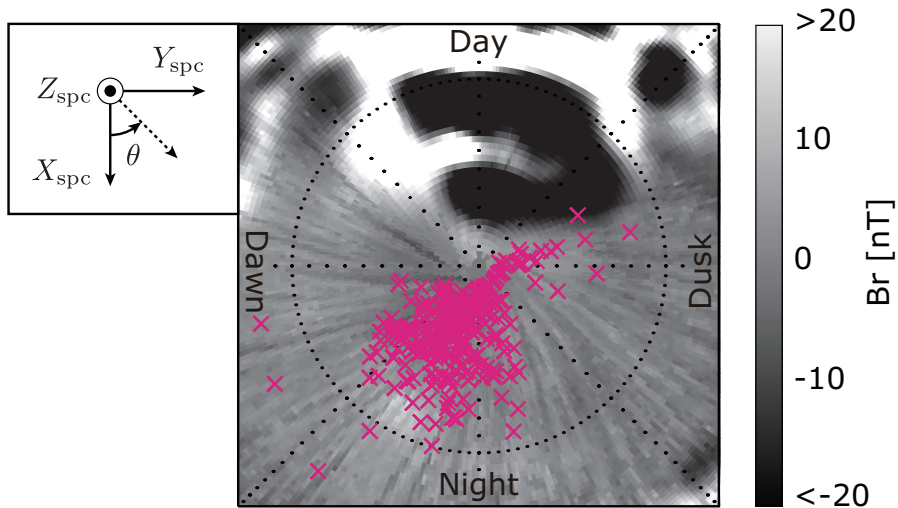


Figure 6.2: Geographic distribution of the 297 identified magnetic flux ropes events, viewed from above the south pole. Magenta crosses are their observed locations. The format of the background crustal magnetic field map is mostly the same as that of Figure 6.1, however the displayed background field is more extensive than Figure 6.1. The definition of the south pole directed, planetocentric (SPC) coordinate system and θ as shown in the upper left side corner are given in the text.

Here is defined another coordinate system used in this paper hereafter. This is referred as the south pole directed, planetocentric (SPC) coordinate system. The SPC coordinate system is fixed with respect to the Martian body, Z_{spc} axis points to vertically upward from the south pole. X_{spc} axis points to the east longitude of 0° and latitude of 0° . Y_{spc} axis completes the right-handed orthogonal system, that is, Y_{spc} axis points to the east longitude of 270° and latitude of 0° . The SPC coordinate system is shown in the upper left side of Figure 6.2.

Figure 6.3 shows an example of the result obtained from the GSR technique for flux rope event observed downstream from the strong crustal magnetic fields on March, 21 2005. The plot format in Figure 6.3 is the same as that in Figures 5.4, and 5.6c. A magnetic flux rope is observed by MGS during 19:19:58–19:27:46 UT (between two magenta vertical lines in Figures 6.3a and 6.3b). Hodograms for this event (not shown here) in the MVA coordinate system clearly show that the vector magnetic field rotates in a circular manner, which is an expected feature of magnetic flux ropes.

Figure 6.3c represents the invariant axial (B_z) magnetic field map in which magnetic field lines in the $x - y$ plane are shown by black curves and the axial magnetic field component is color coded. MGS was travelling in the x direction from left to right at $y = 0$ in the GSR coordinate system. The transverse magnetic field components at $y = 0$ are overplotted as white arrows, which satisfy the right-handed screw rule as mentioned above. The overlaid magenta dashed curve on Figure 6.3c is the boundary used to estimate the volume of the magnetic flux rope. The detailed methodology to determine this boundary is also the same as described in Section 5.5.

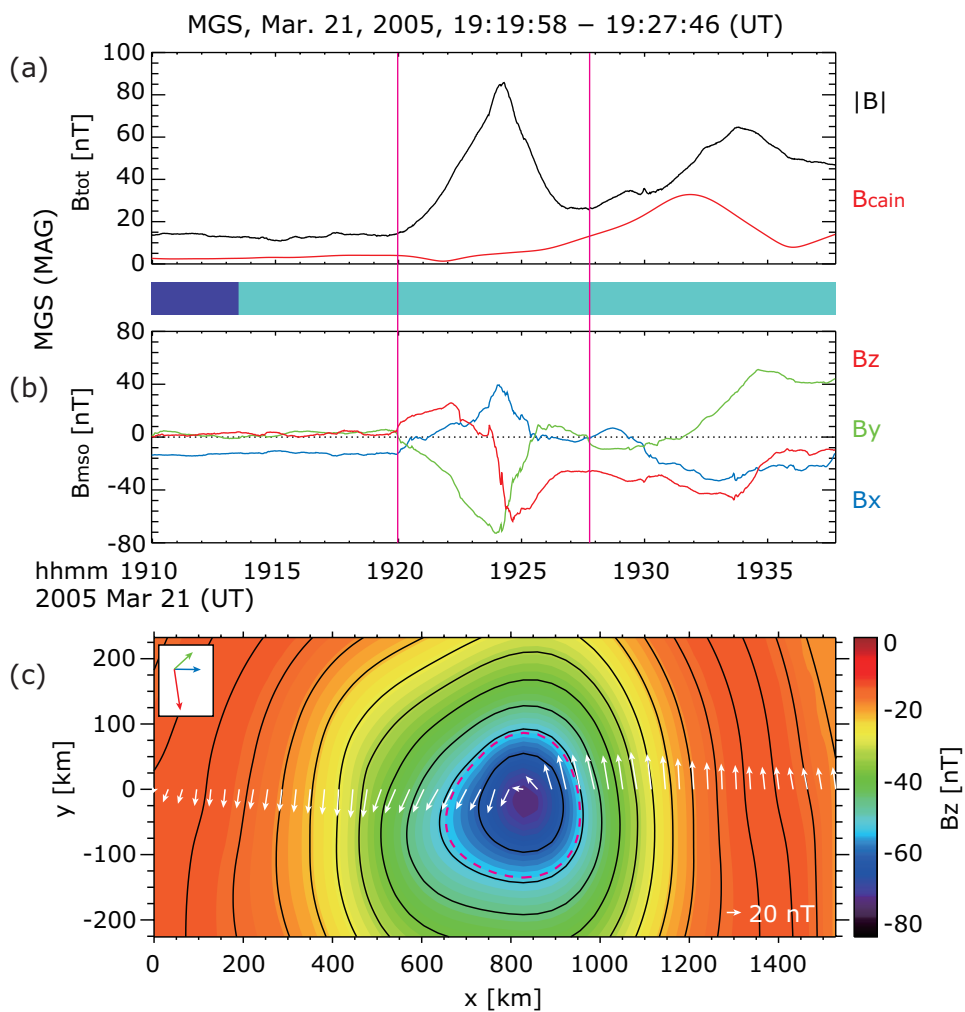


Figure 6.3: An example of the GSR results for the large-scale Martian magnetic flux rope observed downstream from the crustal magnetic fields on March 21, 2005. The format is completely identical to Figures 5.4, and 5.6c.

Figure 6.4 represents an overview of the magnetic flux rope event in the geographic coordinate system, viewed from above the south pole. External fields, which should be dominated by draped IMF, are described as whisker length in Figure 6.4. External field is deduced by subtracting the crustal magnetic field model [Cain *et al.*, 2003] from the observed magnetic fields. External field is mostly stable, which is mostly oriented from dayside to nightside, namely, along the typical plasma streamline shown as a dashed arrow in Figure 6.4. However, magnetic field vectors are rotated during the magnetic flux rope observations, which corresponds to the segment between two magenta crosses in Figure 6.4.

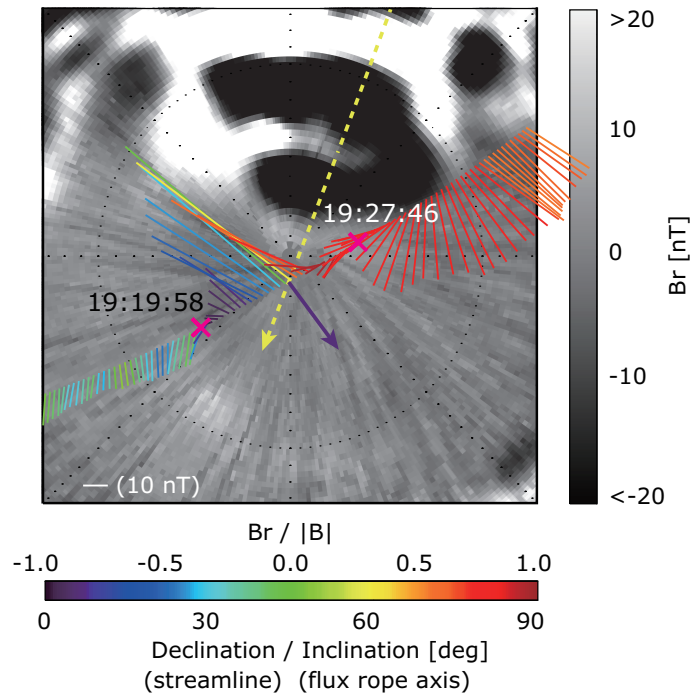


Figure 6.4: External field viewed from above the south pole, with tangential components represented by whisker length and direction originating from orbital track, and the ratio of radial component to the field amplitude indicated by whisker color, as shown by color bar in bottom. Bold solid (dashed) arrows at the location of the flux rope center are the directions of the flux rope axis (typical plasma streamline), with the axial inclination and declination relative to the typical plasma streamline represented by arrow color, respectively. The locations of two magenta crosses correspond to the times of two magenta vertical lines in Figures 6.3a and 6.3b.

The flux rope axis of this event derived from the GSR technique is $[0.80, 0.59, 0.07]$ in the SPC coordinate system. We then define an axial orientation, θ , as the angle between the flux rope axis and the X_{spc} axis in the $X - Y$ plane of the SPC coordinate system shown in Figure 6.2. The X_{spc} axis corresponds to 0° East, roughly parallel to the anti-sunward direction for these events. The axial orientation θ is thus estimated to be approximately 36.4° from the GSR technique. The magnetic flux rope axis deduced from the GSR technique is directed quasi-perpendicular to the spacecraft trajectory, shown as the solid arrow in Figure 6.4.

6.4 Properties of Reconstructed Magnetic Flux Ropes

6.4.1 Axial Orientation

Figure 6.5 shows the measured distribution of axial orientation θ for the 297 flux rope events in the SPC coordinate system. The definition of the magnetic flux rope axial orientation θ was mentioned in the previous section, and was illustrated in Figure 6.2. Figure 6.5 shows that MGS frequently detected the magnetic flux ropes with axial orientation θ between 90° and 135° , which correspond to point to duskward and perpendicular to the $+X_{\text{spc}}$ axis. On the other hand, the magnetic flux ropes with axial orientation θ between -135° and -45° , which corresponds to the axis pointing to dawnward and perpendicular to the $+X_{\text{spc}}$, are quite rare events. Here we categorized the 297 magnetic flux rope events into 4 types according to their axial orientation θ : duskward ($45^\circ \leq \theta \leq 135^\circ$), sunward ($|\theta| \geq 135^\circ$), dawnward ($-135^\circ \leq \theta \leq -45^\circ$), and anti-sunward ($|\theta| \leq 45^\circ$) types relative to the $+X_{\text{spc}}$ axis, respectively.

Figure 6.6 shows the observed geographic distribution for each of the 4 event types. As shown in Figure 6.1, all plasma streamline are typically flown from top to bottom on Figure 6.6, viewed from above the south pole in the geographic coordinate system. Duskward flux ropes (Figure 6.6a) are the most frequently observed ($\sim 61\%$) among the 4 types, and are widely distributed in longitude. In contrast, sunward flux ropes (Figure 6.6b) are mostly observed within 30° of 0° East. The anti-sunward flux ropes in Figure 6.6d are concentrated at longitudes larger than 0° . Moreover, anti-sunward

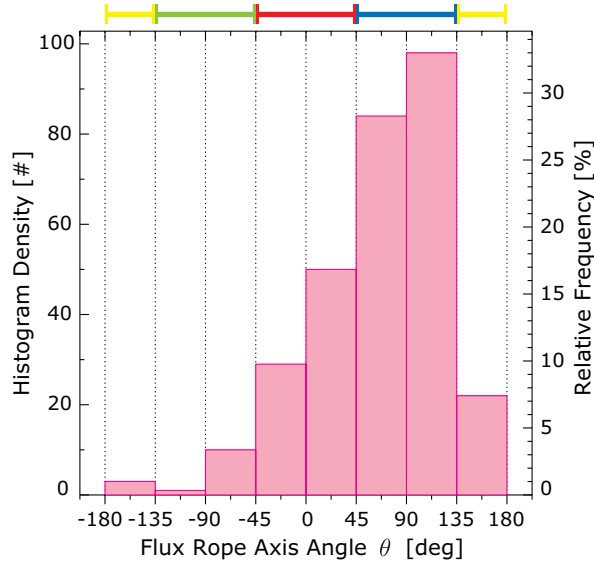


Figure 6.5: Histogram of the 297 identified magnetic flux rope events as a function of the rope axis orientation θ in the south pole directed, planetocentric (SPC) coordinate system. These flux rope axes are based on the results from the Grad-Shafranov reconstruction. Horizontal left (right) side axis is the event numbers (relative frequencies) of these events, respectively. The blue, yellow, green, and red bars correspond to the 4 event types categorized according to the estimated flux rope axial orientation θ .

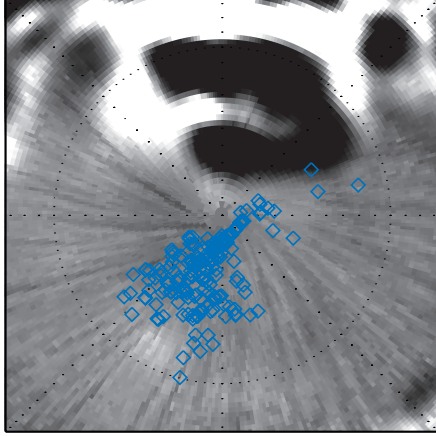
flux ropes are often located over the crustal magnetic field region labeled “B” in Figure 6.7. The region has field lines oriented roughly perpendicular to the region labeled “A” in Figure 6.7. In other words, they are often observed downstream from the crustal magnetic field region labeled “B”.

6.4.2 Dependence on Solar Wind Conditions

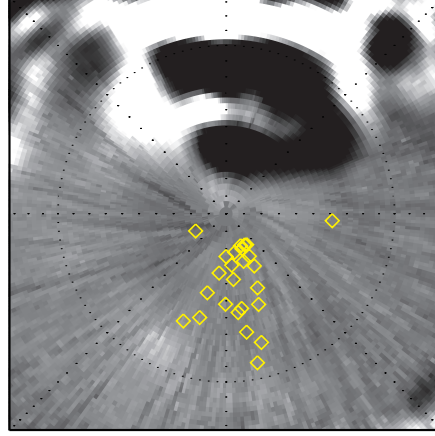
In this subsection, we statistically investigate the dependence of the flux rope occurrence on solar wind conditions. Because MGS observed at ~ 400 km altitude, the solar wind properties cannot be obtained from the MGS observations. However, the solar wind proxies, such as dynamic pressure (P_{sw}) as well as IMF draping direction can be inferred once per orbit from the magnetic field data [*Brain et al.*, 2005, 2006a].

The solar wind dynamic pressure proxy is calculated as the subsolar magnetic field strength at about 400 km altitude, because magnetic pressure is the dominant pressure

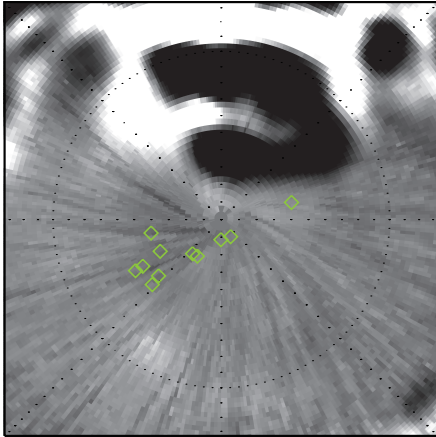
(a) Duskward Type :
 $45^\circ \leq \theta \leq 135^\circ$, 182 Events



(b) Sunward Type :
 $|\theta| \geq 135^\circ$, 25 Events



(c) Dawnward Type :
 $-135^\circ \leq \theta \leq -45^\circ$, 11 Events



(d) Anti-Sunward Type :
 $|\theta| \leq 45^\circ$, 79 Events

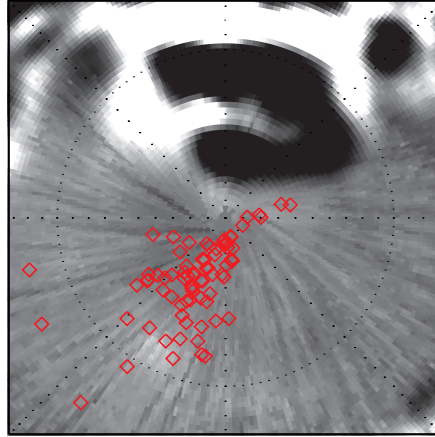


Figure 6.6: The observed geographic location of the 297 magnetic flux rope events divided into 4 categories: (a) duskward, (b) sunward, (c) dawnward, and (d) anti-sunward types, based on the GSR estimated flux rope axial orientation θ relative to the X_{spc} axis direction. The format of background crustal magnetic field map is the same as that of Figure 6.2. All the plasma streamlines at the observed location are approximately flowing from top (dayside) to bottom (nightside) on each panel.

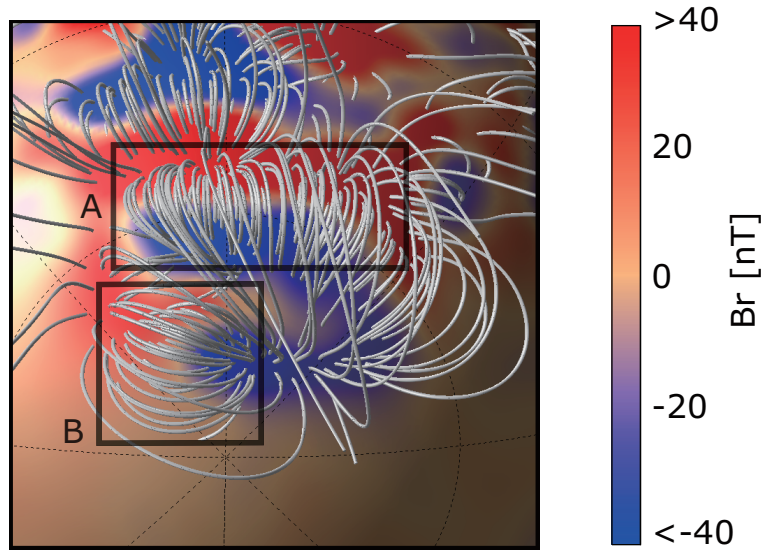


Figure 6.7: Three-dimensional visualization of the Martian crustal magnetic field lines, viewed from above the south pole in the geographic coordinate system, based on the Martian crustal magnetic field model [Cain *et al.*, 2003]. Magnetic field lines are only traced from strong crustal magnetic field region with the altitude of ~ 400 km from the Martian surface by using forth-order Runge-Kutta integrator. The density of magnetic field lines is roughly proportional to the crustal magnetic field strength. Red (blue) colored crustal magnetic field regions have positive (negative) magnetic field polarities. The crustal magnetic field regions labeled “A” and “B” are utilized to discuss the formation processes of magnetic flux ropes associated with the strong crustal magnetic fields in Section 6.5.

term inside the induced magnetosphere of Mars, and is approximately balanced with the solar wind dynamic pressure [Crider *et al.*, 2003; Brain *et al.*, 2005]. Figure 6.8 represents distribution of the solar wind dynamic pressure P_{sw} proxy for the 297 identified events and their observational probability relative to the 3,007 orbits for the statistical study. It is clearly shown that the observation probability of those flux ropes increases with the solar wind dynamic pressure proxy up to ~ 100 nT. On the other hand, the events are seldom observed during very high solar wind dynamic pressure periods (larger than ~ 100 nT), although the events during these periods might not have enough statistics. There is no clear difference in the solar wind pressure for each of the 4 event types discussed above (not shown). Although the averaged solar

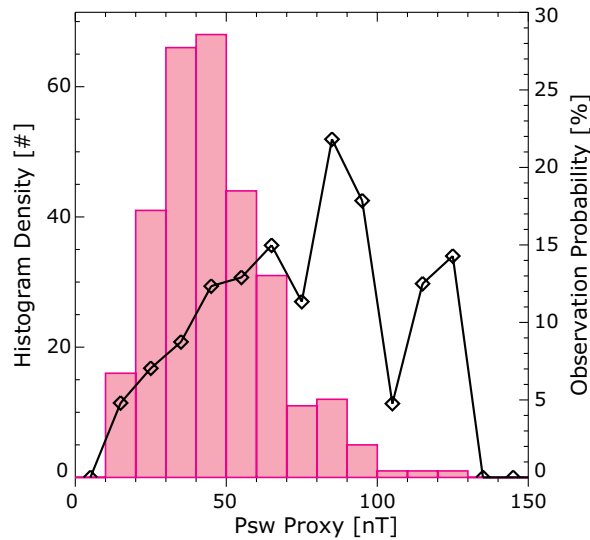


Figure 6.8: Histogram of the 297 identified magnetic flux rope events as a function of solar wind dynamic pressure P_{sw} proxy. Black diamonds with a black solid line represent the observation probability of the 297 magnetic flux rope events normalized to the 3,007 orbits, systematically selected for the statistical survey to search magnetic flux roes as mentioned in Section 6.2.

wind dynamic pressure during sunward (Figure 6.6b) and downward (Figure 6.6c) flux rope events are slightly larger than the others by about 10 nT, the average solar wind dynamic pressure with the standard deviation turn out to be 46.0 ± 19.3 nT during the 297 events.

The draped IMF field lines in an induced magnetosphere tend to be aligned along the plasma streamline at the high magnetic latitudes because of the velocity shear across the ionopause, as suggested by spacecraft observations [e.g., *Law and Cloutier, 1995; Strangeway and Russell, 1996; Brain et al., 2006a*], as well as numerical simulations [e.g., *Ma et al., 2013*]. We here investigated the dependence of the local external draped field direction derived from the method as mentioned in Section 6.3 (displayed in Figure 6.4). Figure 6.9 illustrates the observation frequency with respect to the local external draped magnetic field direction in the SPC coordinate system for the 4 magnetic flux rope types categorized in Subsection 6.4.1. We only used the vector magnetic field data acquired by MGS during the time interval 5 – 10 minutes before

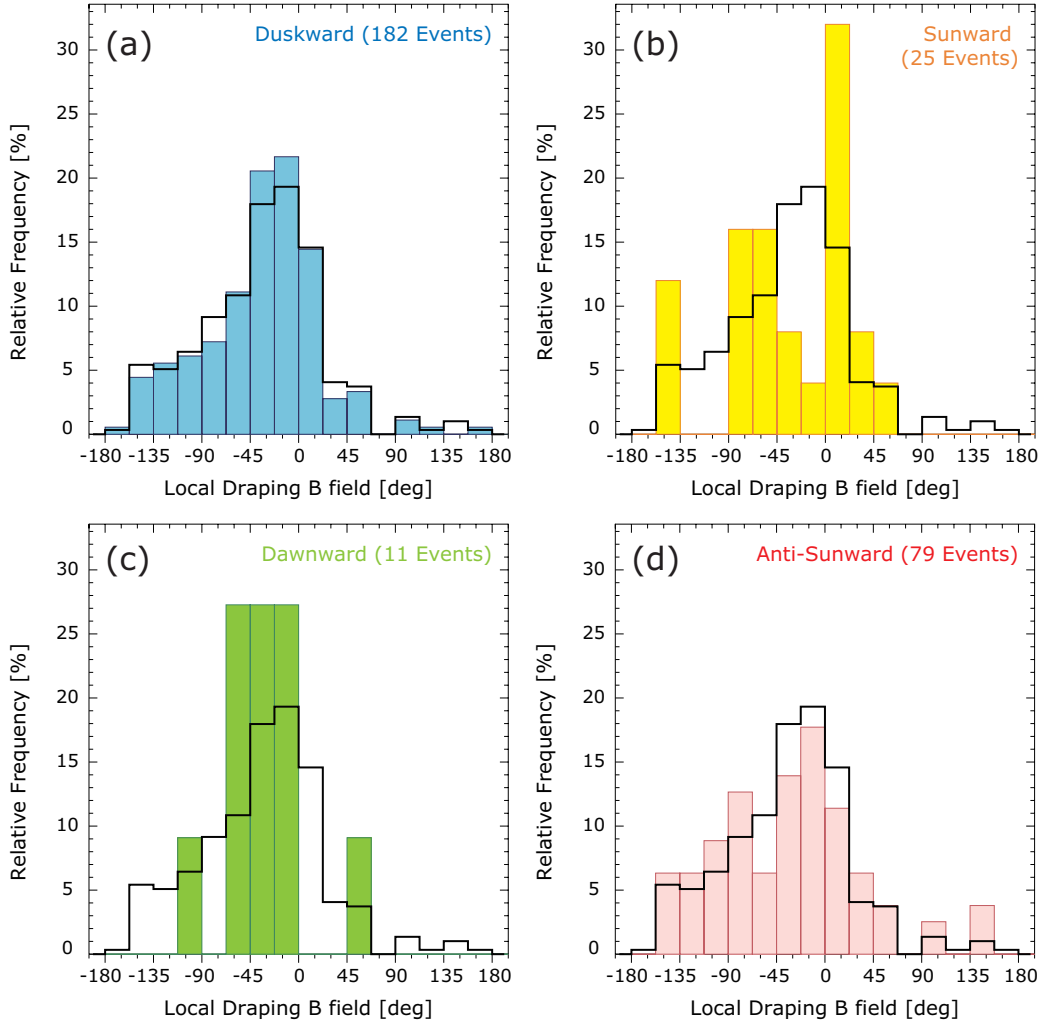


Figure 6.9: Histogram of the 297 identified magnetic flux rope events as a function of the local external draped magnetic field orientation in the south pole directed, planetocentric (SPC) coordinate system divided into 4 categories: (a) duskward, (b) sunward, (c) dawnward, and (d) anti-sunward types relative to the X_{SPC} axis. Black solid lines represent the histogram for all the 297 magnetic flux rope events.

each event, so as to avoid distortion from the crustal magnetic field. This local external draped magnetic field orientation, which is the abscissa of Figure 6.9, is defined in SPC coordinates. Figure 6.9 indicates that there is no significant difference in the distribution between duskward (6.9a) and anti-sunward (6.9d) types of the flux ropes. However, the sunward type in Figure 6.9b shows a relatively different pattern, compared with the distribution for all the 297 identified magnetic flux ropes shown as an overlaid bold black solid lines. The local external draped magnetic field orientation including all types tends to be draped in the directional range between -60° and 0° (-32.1° in average) in the SPC coordinate system, and this direction roughly corresponds between dawnward and anti-sunward.

6.4.3 Flux Rope Size

Table 6.1 summarizes the statistical averaged GSR results. The methodology for deriving flux rope radius and length as well as flux rope boundary is completely the same as mentioned in Section 5.5. It should be noticed again that the rope radius and length might be underestimated, because our boundary of a recovered magnetic flux rope might be strictly defined, or be sometimes partially beyond the reconstructed two-dimensional frame. Hence, these estimated values are lower limits.

Table 6.1: A summary of lower limits on the averaged magnetic flux rope spatial properties for the four types categorized according to axial orientation based on the Grad-Shafranov reconstruction (GSR) technique.

Category	Duskward	Sunward	Dawnward	Anti-Sunward	All
Events [#] (Ratio [%])	182 (61.3)	25 (8.4)	11 (3.7)	79 (26.6)	297
Events for Volume Calculation	164	23	11	59	257
Equivalent Rope Radius [km]	104.1	88.1	43.9	78.0	94.1
Rope Length [km]	187.1	252.5	255.9	127.3	182.1
Rope Volume [cm ³]	1.12×10^{22}	1.29×10^{22}	2.31×10^{21}	3.42×10^{21}	9.16×10^{21}
P_{sw} Proxy [nT]	45.2	52.2	58.7	44.2	46.0

In this study, the events in which MGS traveled inside our defined boundary

at least are utilized for their volume calculation. One of remarkable results shown in Table 6.1 is that the lower limits of the volume of the duskward and sunward magnetic flux ropes are larger by a factor of approximately 3–5 than those of the dawnward and anti-sunward ones. The lower limits on the flux rope volume when all types are considered is between 10^{21} and 10^{22} cm³. Therefore, if we assume the local ionospheric plasma number density Ni , we are able to assess the lower limits on the plasma content inside the recovered magnetic flux ropes, multiplying the flux rope volume by Ni , such that to be $9.16 \times 10^{21} \times Ni$ for the 297 events average. Assuming that $Ni = 10^3$ ions/cm³, which is the typical values at the altitude of about 400 km based on the MEX/MARSIS observations [e.g., *Gurnett et al.*, 2008; *Morgan et al.*, 2008], the estimated flux rope plasma content ranges between 10^{24} and 10^{25} ions.

6.5 Discussion

6.5.1 Formation Scenarios

Brain et al. [2010a] proposed that the observed large-scale magnetic flux rope downstream from the strong crustal magnetic fields can be formed by magnetic reconnection between the upstream crustal magnetic fields that had been stretched tailward, analogous to plasmoids in Earth’s magnetotail (Figure 5.11). If the magnetic flux ropes are formed via the scenario proposed by *Brain et al.* [2010a] at the crustal magnetic field region labeled “A” in Figure 6.7, the resultant magnetic flux rope axial orientation should be quasi-perpendicular to the typical plasma streamline in this situation. Moreover, transverse magnetic field lines perpendicular to the flux rope axis on the side closest to the planet should be directed toward $-X_{\text{spc}}$, which is approximately opposite to typical crustal magnetic field lines in region “A”. *Beharrell and Wild* [2012] suggested that flux ropes can be formed by internal reconnection, whereby crustal field lines are stretched and overlay neighboring crustal magnetic field lines (Figure 5.12). If the magnetic flux ropes are formed in the region “A” through *Beharrell and Wild* [2012]’s scenario, the axial orientation and transverse magnetic field lines should be qualitatively similar to those formed via the mechanism proposed

by *Brain et al.* [2010a].

Furthermore, if we take into account that the resultant magnetic flux ropes have significant guide fields, they should remain attached to the Martian surface without a significant ionospheric tailward flow sufficient to overcome the magnetic tension force of the magnetic flux rope, even though they are formed via the scenario proposed by *Brain et al.* [2010a]. This is why there should be one more step so as to detach the flux ropes formed via magnetic reconnection between neighboring crustal field lines from the surface. Hence, we hereafter refer to the possible formation scenario that magnetic flux ropes are formed via magnetic reconnection between neighboring crustal magnetic field lines as the ‘internal reconnection’ scenario. In this subsection, we examine whether the magnetic flux ropes used in this statistical study can be explained by internal reconnection based on two aspects of the GSR results: (i) the flux rope axial orientation (ii) transverse field direction in the magnetic flux rope on the side closest to the planet in the SPC coordinate system.

Duskward Type

Duskward magnetic flux ropes are the most common among the 4 types. They are widely distributed in the east longitude as shown in Figure 6.6a. They have no significant dependence on the solar wind dynamic pressure as well as the external draped magnetic field direction in Figure 6.9a, compared with other magnetic flux rope types. Their axes are approximately oriented toward the $+Y_{\text{SPC}}$ axis, duskward and perpendicular to the typical plasma streamline.

It should be also noted again that the transverse magnetic field rotation perpendicular to the flux rope axis must be right-handed. Hence, the transverse magnetic field direction on the side closest to the planet should be approximately parallel to the $-X_{\text{SPC}}$ axis. If duskward magnetic flux ropes are formed at the crustal magnetic field region “A”, the transverse field lines on the side closest to the planet are thus opposite to the local crustal magnetic field lines in region “A”. Therefore, the characteristics of the magnetic field configuration, namely, both the flux rope axial orientation and transverse field direction are consistent with the internal reconnection.

Sunward Type

Sunward flux ropes have axes that point approximately anti-parallel to the typical plasma streamline. They are only detected when the solar wind dynamic pressure is relatively larger than usual by about 10 nT, and the distribution of the external draped direction shows the most different pattern from the average distribution for all the identified 297 events (Figure 6.9b). The direction of the transverse magnetic field in their magnetic flux ropes on the side closest to the planet, derived from the right-handed screw rule, is approximately oriented to the $-Y_{\text{spc}}$ axis.

If magnetic flux ropes are assumed to be formed around the region “B” via the internal reconnection, their axes should be oriented approximately parallel to the $-X_{\text{spc}}$ axis, and the $-Y_{\text{spc}}$ axis should be their transverse magnetic field direction on the side closest to the planet. These magnetic configurations are consistent with the sunward ones. Therefore, the sunward magnetic flux ropes can be explained by the internal reconnection driven at the crustal magnetic field region “B”.

Dawnward Type

Dawnward magnetic flux ropes are the rarest ($\sim 3.7\%$) among the identified 297 events. The axial orientation θ is directed between -135° and -45° in the $x-y$ plane of the SPC coordinate system (Figure 6.5), which is roughly along the $-Y_{\text{spc}}$ axis. The transverse magnetic field direction of their magnetic flux ropes on the side closest to the planet is approximately along the $+X_{\text{spc}}$ axis. This orientation is aligned to the typical plasma streamline as well as the local crustal magnetic field direction at the region “A”, and is roughly perpendicular to the local crustal magnetic field direction at the region “B”. Therefore, the dawnward magnetic flux ropes cannot be explained by internal reconnection.

Figure 6.10a illustrates a possible formation process. We assume that their magnetic flux ropes are formed by crustal magnetic fields at region “A”, because the crustal magnetic field region “A” is the largest part in the vicinity of the upstream crustal magnetic fields. The dawnward magnetic flux ropes can be formed via the following scenario shown in Figure 6.10a:

- i) There are crustal magnetic field lines at the region as labeled “A” in Figure 6.7.
- ii) The local external magnetic field (black dashed arrows) overlays the crustal magnetic fields lines in region “A”, consistent with the observations of the external magnetic field as shown in Figure 6.9.
- iii) Multiple magnetic reconnections are simultaneously driven between the original crustal magnetic fields (black solid arrows) and the overlaid local external draped magnetic fields (black dashed arrows) at the red crosses.
- iv) A magnetic flux rope forms (helical black bold arrow) via multiple magnetic reconnections. The axial orientation of the resultant magnetic flux ropes (green bold arrow) is directed downward and perpendicular to the typical plasma streamline.

We hereafter refer to magnetic flux ropes formed via multiple magnetic reconnections between crustal and overlaid draping magnetic field lines as formed in an ‘external reconnection’ scenario. One consideration for the external reconnection case is the shear angle between crustal and overlaid draping magnetic field lines. Dawnward magnetic flux ropes are often under low shear angle conditions: crustal magnetic field lines in region “A” are approximately $\theta = 0^\circ$ ($+X_{\text{spc}}$) and the local external draped direction is mostly approximately $-60^\circ < \theta < 0^\circ$ in Figure 6.9c. *Swisdak et al.* [2003, 2010] suggested that the magnetic reconnection occurrence depends on $\Delta\beta$ (the difference of plasma β on two sides of the current sheet) as well as magnetic shear angle. In other words, magnetic reconnection can occur even under the low shear angle during low $\Delta\beta$ ($\simeq 1 - 2$) conditions [*Swisdak et al.*, 2010; *Phan et al.*, 2013]. This is why the dawnward magnetic flux ropes might be the most rare events among the 4 types, because the low $\Delta\beta$ condition must be fulfilled to drive magnetic reconnection between crustal and overlaid draping magnetic field lines under the low shear angle.

Anti-Sunward Type

The anti-Sunward magnetic flux ropes are the second most common ($\sim 26.6\%$) among the identified 297 events. The axial orientation θ is directed less than 45° in

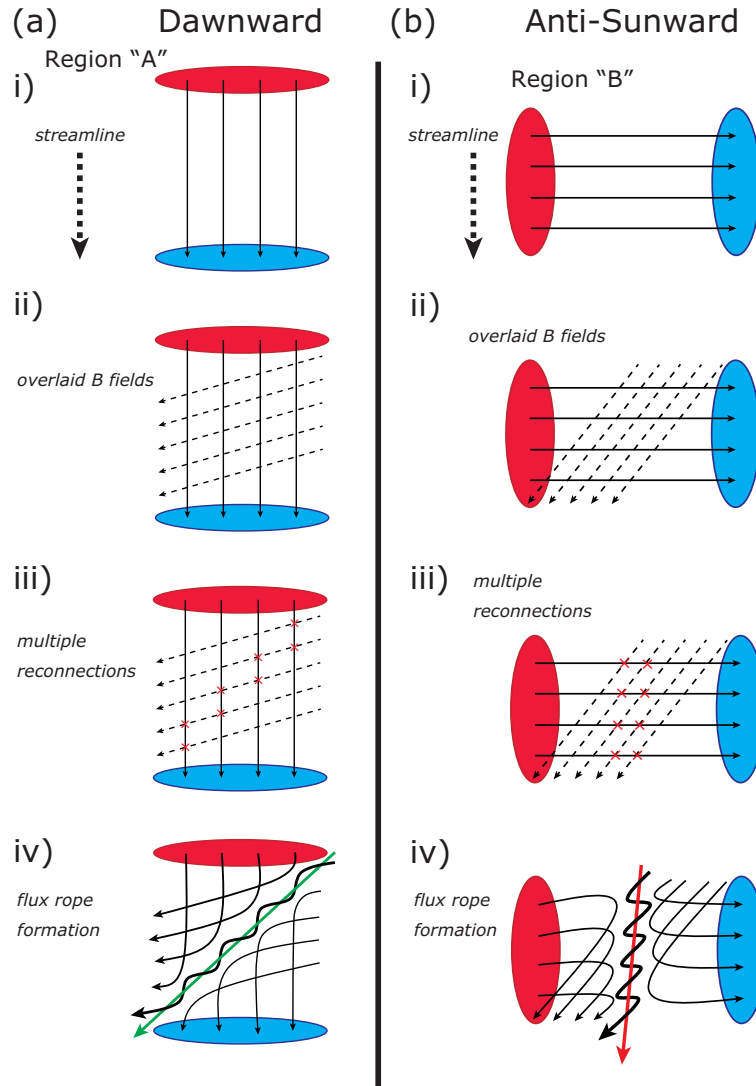


Figure 6.10: Schematic illustration of new possible scenarios for (a) downward, and (b) anti-sunward types to form large-scale magnetic flux ropes observed downstream from the strong crustal magnetic fields. Scenes are evolved from i) to iv) to form the magnetic flux ropes. These schematic illustrations are viewed from above the south pole in the $x - y$ plane in the SPC coordinate system, similar to Figures 6.1, 6.2, 6.4, 6.6, and 6.7. Red and blue colored regions are depicted to be positive and negative polarity crustal magnetic field regions, respectively, similar to Figure 6.7. Black solid arrows are described magnetic field lines. Black dashed arrows shown in scenes ii) and iii) are overlaid magnetic field lines, assumed to be the local external draped magnetic fields. Multiple magnetic reconnection points are shown as the red crosses in scene iii). Helical black bold arrows are resultant magnetic flux ropes. Green and red bold arrows are resultant magnetic flux rope axis.

the $x - y$ plane of the SPC coordinate system (Figure 6.5), which is approximately parallel to the typical plasma streamline ($+X_{\text{spc}}$ axis). Their event distribution with respect to the external conditions is similar to the average. The transverse magnetic field direction in their magnetic flux ropes on the side closest to the planet is along approximately the $+Y_{\text{spc}}$ axis. This orientation is quasi-perpendicular to the local crustal magnetic field direction in region “A”, however, aligned to that in region “B”. Therefore, the anti-sunward magnetic flux ropes can be also explained by neither plasmoid nor internal reconnection. It should be noted that Figure 6.6d indicates the typical plasma streamline of the anti-sunward magnetic flux ropes is often along the crustal magnetic field region labeled “B” in Figure 6.7. Hence, we also propose a possible scenario to form the anti-sunward type of magnetic flux ropes originating from region “B”, similar to that of the dawnward type illustrated in Figure 6.10b.

The axial orientation of the resultant magnetic flux rope (red bold arrow in Figure 6.10b) is directed to the $+X_{\text{spc}}$, which is quasi-parallel to the typical plasma streamline. The transverse magnetic field direction in the resultant magnetic flux ropes (helical black bold arrow in Figure 6.10b) on the side closest to the planet is aligned to the local crustal magnetic field direction at region “B”, which is along approximately the $+Y_{\text{spc}}$ axis. Therefore, we suggested that the anti-sunward magnetic flux ropes can be explained by external reconnection case at region “B”, that is, they might be formed via multiple reconnections between crustal magnetic fields at region “B” and the overlaid local external draped magnetic fields (black dashed arrows in Figure 6.10b).

As mentioned above, the magnetic reconnection rates can depend on the shear angle between crustal and overlaid magnetic field lines [Swisdak *et al.*, 2010; Phan *et al.*, 2013]. The anti-sunward magnetic flux ropes are often observed under relatively larger shear angle than the dawnward ones, because crustal magnetic field lines in region “B” are directed approximately $\theta = 90^\circ$ ($+Y_{\text{spc}}$) and the local external draped direction is mostly in the range $-90^\circ < \theta < 0^\circ$ in the $x - y$ plane in the SPC coordinate system (Figure 6.9d). Hence, the difference in the shear angle might reflect the numbers of event between the anti-sunward and dawnward magnetic flux ropes in the external reconnection scenario.

One of the controversies seen in the GSR statistical results is the observation probabilities between the internal and external magnetic flux rope cases. The GSR statistical results show that internal reconnection (duskward + sunward: 207 events) cases are observed more frequently than external reconnection (dawnward + anti-sunward: 90 events) ones. One possible interpretation is that the altitude to form the flux ropes for the external reconnection case might be higher than those for the internal reconnection case, because overlaid draping magnetic fields are necessary for their formation. This interpretation leads to another possibility that the magnetic flux ropes for the external reconnection case might be formed more frequently than MGS can observe at an altitude of 400 km.

6.5.2 Contribution to Ion Escape from Mars

As described in Subsection 6.4.3, Table 6.1 shows that the lower limits of the spatial scale of the duskward and sunward magnetic flux ropes (internal reconnection cases) are larger by a factor of approximately 3–5 than those of the dawnward and anti-sunward ones (external reconnection cases). The GSR statistical results suggest that the internal reconnection cases can be formed via magnetic reconnections between neighboring crustal magnetic field lines, and should remain attached to the crust without a significant ionospheric tailward flow sufficient to overcome the magnetic tension force of the flux ropes. Hence, those flux ropes of the internal reconnection case do not contribute so much to the ion escape from Mars unless additional reconnection detaches the flux ropes from the crust. On the other hand, the external reconnection cases can be easily detached from the surface, because they are formed via multiple magnetic reconnections between crustal and overlaid draping magnetic field lines connected to the IMF.

We estimate the ion escape rates assuming that ionospheric plasma inside the flux ropes is completely removed from the Martian upper atmosphere within the interval of MGS sampling each structure. The potential ion escape rates due the dawnward and anti-sunward magnetic flux ropes (external reconnection cases) are estimated to be approximately 10^{22} ions/sec, because the durations of the recovered magnetic flux

ropes are typically within a few minutes. MEX observations confirmed that global average ion escape rates during the solar minimum are approximately 10^{24} ions/sec [e.g., *Barabash et al.*, 2007a; *Lundin et al.*, 2008a]. These results indicate that ion escape due to the detached magnetic flux rope downstream from the strong crustal magnetic fields can instantaneously contribute to approximately 1 % of the global average ion escape rates during the solar minimum. Therefore, the ion escape rates due to the magnetic flux ropes do not significantly contribute to atmospheric ion escape from Mars.

6.6 Summary

In this chapter, we investigated possible formation scenarios of Martian magnetic flux ropes observed in the vicinity of the Martian south pole and downstream from strong crustal magnetic fields, based on the Grad-Shafranov reconstruction (GSR) technique. We performed a statistical study on the 682 magnetic flux rope candidates observed by Mars Global Surveyor (MGS) between April, 1999 and November, 2006. We were able to uniquely estimate their axial orientation and spatial structures by the GSR technique for 297 magnetic flux rope events (Figure 6.2). The statistical results are summarized as follows:

1. The observed frequency of magnetic flux ropes increases with the solar wind dynamic pressure P_{sw} proxy [*Brain et al.*, 2005] up to ~ 100 nT (Figure 6.8). Local external draped magnetic fields are typically oriented between -60° and 0° in the south pole directed, planetocentric (SPC) coordinate system as the precondition during the large-scale magnetic flux rope events (Figure 6.9).
2. The 297 magnetic flux rope events can be categorized into 4 types according to axial orientation θ in the $x - y$ plane of the SPC coordinate system: what we call duskward, sunward, duskward, and anti-sunward magnetic flux ropes, respectively (Figure 6.5).
3. Based on the characteristics of the identified 297 magnetic flux rope events, such as their axial orientation and transverse magnetic field direction on the side

closest to the planet, we could infer formation scenarios of Martian magnetic flux rope downstream from the strong crustal magnetic fields.

4. Duskward and sunward magnetic flux ropes (Figures 6.6a and 6.6b) can be explained by ‘internal reconnection’ scenario, in which they are formed via magnetic reconnections between neighboring crustal magnetic field lines at the crustal magnetic field regions. Such formation scenarios were previously proposed by *Brain et al.* [2010a] and *Beharrell and Wild* [2012].
5. Dawnward and anti-sunward magnetic flux ropes (Figures 6.6c and 6.6d) cannot be explained by magnetic reconnections between only neighboring crustal magnetic field lines. Overlaid magnetic field lines above the ambient crustal magnetic field lines could be essential for their formation, because they can be formed by multiple magnetic reconnections between crustal and overlaid draping magnetic field lines as summarized in Figure 6.10. The most plausible candidate of those overlaid magnetic field lines can be local external draped magnetic field lines.
6. Internal reconnection cases should remain attached to the crust. Hence, those flux ropes of internal reconnection case do not make a large contribution to the ion escape from Mars unless an additional reconnection occurs that can detach them from the crust. On the other hand, external reconnection cases should be detached from the surface, because they are formed via multiple magnetic reconnections between crustal and overlaid draping magnetic field lines connected to the IMF.
7. The estimated lower limits of the volume of duskward and sunward magnetic flux ropes (internal reconnection cases) are larger by a factor of approximately 3–5 than those of dawnward and anti-sunward ones (external reconnection cases) as summarized in Table 6.1. The potential ion escape rates due the dawnward and anti-sunward magnetic flux ropes (external reconnection cases) are estimated to be approximately 10^{22} ions/sec. This results indicate that ion escape rates due to the detached magnetic flux rope downstream from the strong crustal magnetic

fields can instantaneously contribute to approximately 1 % of the global average ion escape rates during the solar minimum [e.g., *Barabash et al.*, 2007a; *Lundin et al.*, 2008a]. Therefore, the ion escape rates due to the magnetic flux ropes may not significantly contribute to atmospheric escape from Mars.

As mentioned in Section 5.2, we had to impose additional assumptions for an application of the GSR technique due to the lack of the ion observation by MGS. If Martian ionospheric plasma properties, such as number density, bulk velocity vector, and temperature, are simultaneously available during magnetic flux rope observations, we could estimate their spatial structure more accurately. Moreover, we could better evaluate possible ion escape rates owing to the magnetic flux ropes, if the ionospheric ion density inside the magnetic flux rope were available. Therefore, comprehensive in-situ plasma and magnetic field observations are essential in order to understand ion escape rates and formation scenarios of Martian magnetic flux ropes. The MAVEN (Mars Atmosphere and Volatile Evolution) spacecraft was successfully launched on November 18, 2013, and is scheduled to arrive at Mars on September, 2014. MAVEN carries a suite of atmospheric and plasma instruments which are capable of investigating the role of the magnetic flux ropes in atmospheric escape from Mars. Hence, MAVEN will provide us with numerous helpful data to better understand possible formation scenarios of magnetic flux ropes observed over a wide range of local time, latitude, and altitude.

Chapter 7

General Conclusions and Future Perspective

As summarized in Chapter 1, several candidates of atmospheric escape processes that occur on an unmagnetized planet such as Mars through the direct interaction of the solar wind with the upper atmosphere have been proposed based on in-situ spacecraft observations [e.g., *Chassefière and Leblanc, 2004; Lundin et al., 2007*, and reference therein] and numerical simulations [e.g., *Kallio et al., 2011*]. Past and present in-situ spacecraft observations have provided certain clues of those candidate atmospheric escape processes [reviewed in *Lundin, 2011; Dubinin et al., 2011*]. The Mars missions Mars Global Surveyor (MGS) and Mars Express (MEX) have played important roles in the overall advances in the field of solar wind interaction with the Martian upper atmosphere. However, comprehensive and continuous plasma and field observations of Mars have never been achieved, which prevents the determination of atmospheric escape phenomena, which are shown in Table 1.2. Therefore, we do not fully understand the dependence that each candidate atmospheric escape process has on the solar wind variations and effects of crustal magnetic fields [e.g., *Lundin et al., 2008b; Edberg et al., 2010; Brain et al., 2010a; Fang et al., 2010b*]. In this study, which is based on the MEX and MGS observations, I focused on ion sputtering and magnetic flux ropes, whose properties are as yet unclear and should be included among the candidate atmospheric escape processes.

A neutral escape resulting from ion sputtering has never been directly measured by spacecraft. Therefore, the level of dependence that ion sputtering has on the solar wind and crustal magnetic field orientation is not fully understood. Numerous magnetic flux ropes have been detected by MGS around Mars [e.g., *Vignes et al.*, 2004; *Briggs et al.*, 2011]. In addition, *Brain et al.* [2010a] found a large-scale isolated magnetic flux rope associated with the strong crustal magnetic fields, which might significantly contribute to the atmospheric escape from Mars. However, the question of their quantitative contribution among candidate atmospheric escape processes remains because of ambiguities that arise from the estimation of their shape and size from single spacecraft measurements.

Solar Wind (SW) Dependence

Previous numerical simulations predicted that the precipitation of PHIs, which can cause ion sputtering, onto Mars always occurs, even under typically moderate solar wind conditions [e.g., *Luhmann and Kozyra*, 1991; *Chaufray et al.*, 2007]. However, this thesis showed from the MEX ion observations that PHI precipitation is not always observed and is primarily coincidental with CIR passages. This result indicates that the influence of ion sputtering on atmospheric escape from Mars can be highly variable depending on the solar wind conditions arriving at Mars, as shown in Chapter 3 [*Hara et al.*, 2011]. I also investigated the effects of the solar wind electric fields \mathbf{E}_{sw} on precipitating PHIs, because \mathbf{E}_{sw} can be important for determining the picked-up PHIs precipitation toward the Martian upper atmosphere. To estimate the IMF orientation without a magnetometer, the velocity distribution of exospheric-origin pickup protons (so-called ‘ring ions’) was utilized. The dependence of the estimated IMF orientation on the precipitation of PHIs showed that they tend to be observed on the solar wind electric field side rather than the interplanetary magnetic field side (Figure 4.7). This study also showed that PHI precipitation is likely to be observed in the downward electric field hemisphere of one event and was derived from the comparison of the velocity distribution function between MEX observations and test-particle simulations. The observed precipitation feature of the solar wind electric field

is consistent with previous numerical simulations [e.g., *Luhmann and Kozyra*, 1991; *Chaufray et al.*, 2007], as shown in Chapter 4.

Briggs et al. [2011] reported that magnetic flux ropes are more likely to be observed by MGS during low solar wind dynamic pressure (P_{sw}) periods. This observed tendency was also indicated in previous studies [e.g., *Russell and Elphic*, 1979; *Vignes et al.*, 2004]. However, those magnetic flux ropes were not so strongly associated with crustal magnetic fields, and the isolated large-scale magnetic flux rope event observed downstream from the crustal magnetic field around the south pole was observed when P_{sw} was approximately 4 times larger than its median value; thus the IMF orientation might rotate by $\sim 180^\circ$ [*Brain et al.*, 2010a]. Chapters 5 and 6 of this thesis statistically investigated these large-scale flux rope events associated with strong crustal magnetic fields, and the results indicated that their observation is likely increased when the P_{sw} proxy [*Brain et al.*, 2005] increases up to approximately 100 nT and that they are seldom observed during higher P_{sw} periods (> 100 nT). The solar wind dependence observed in the large-scale flux rope events associated with crustal magnetic fields is consistent with that found by *Brain et al.* [2010a].

Effects of Crustal B Fields

The observed locations of precipitating PHIs indicated that they are frequently observed in the region where the expected crustal magnetic fields are rather small in Figures 4.5 and 4.6. This result suggested that precipitating PHIs might also be controlled by crustal magnetic fields. However, the MEX periapsis around the southern mid latitude where the crustal magnetic fields are primarily distributed is mostly located on the nightside (Figure 4.4b) because of the MEX orbital configuration. *Chaufray et al.* [2007] confirmed that the precipitation flux on the nightside is much smaller than that on the dayside, which was predicted by their hybrid simulation. The lack of a PHI precipitation event in the southern mid latitude might be caused by a biased orbital coverage, which is why the effect of the crustal magnetic fields on precipitating PHIs is controversial.

Based on the MGS data analyses for 70 obvious magnetic flux rope events, this

thesis found that the events observed at solar zenith angle (SZA) larger than 75° with a duration longer than 240 sec are mostly observed downstream from the strong crustal magnetic field in the southern hemisphere (Figures 5.7 and 5.9). I revealed that the estimated spatial scales, obtained from the Grad-Shafranov reconstruction (GSR) technique vary by 2–3 orders of magnitude among the recovered events and that their potential escape rates are estimated to be on the order of 10^{22} – 10^{23} ions/sec [Hara *et al.*, 2014]. This escape rate is approximately 10% of the global average ion escape rate (integrating all escape processes) during the solar minimum [e.g., Barabash *et al.*, 2007a; Lundin *et al.*, 2008a], as shown in Chapter 5. This thesis also evaluated possible formation scenarios of the magnetic flux rope events observed downstream from the crustal magnetic fields based on the GSR results in Chapter 6. I found that two-thirds of the events can be explained by previously proposed scenarios in which they are only formed by magnetic reconnection between neighboring crustal magnetic field lines [Brain *et al.*, 2010a; Beharrell and Wild, 2012]. However, the remaining events cannot be explained, but they might be formed by multiple magnetic reconnections between crustal and overlaid draping magnetic field lines (Figure 6.10). These resultant flux ropes should not be attached to the surface because the origin of such flux ropes is partially to the result of overlaid draping magnetic field lines connecting the IMF. A summary of the results obtained in this thesis is shown in Table 7.1.

In this thesis, I investigated the statistical properties of precipitating PHIs observed by MEX to determine the dependence of ion sputtering on the solar wind variations. As mentioned in Subsection 1.3.4, ion sputtering is a neutral escape process that induces the escape of the energized neutral atoms produced by precipitating PHIs. However, neutral atoms sputtered by precipitating picked-up PHIs have never been directly observed by conventional in-situ spacecraft plasma measurements around Mars. To definitively determine the causes of the ion sputtering phenomena, upcoming spacecraft missions must directly detect such sputtered neutral atoms. MAVEN might be able to simultaneously observe sputtered neutral particles along with precipitating picked-up PHIs.

As mentioned in Subsection 5.2.1, when the GSR technique was applied to the

Table 7.1: Summary of results obtained in this thesis.

Effects	Atmospheric Escape Processes	
	Ion sputtering (PHI Precipitation)	Magnetic flux rope
SW variations	Precipitating PHIs are not always observed, but mostly coincide with CIR passage. Their spatial distribution depends on the solar wind electric field \mathbf{E}_{sw} (IMF orientation).	Flux ropes observed downstream from the crustal magnetic fields are more frequently observed as P_{sw} proxy increases (up to about 100 nT).
Crustal \mathbf{B} fields	Precipitating PHIs are frequently observed where crustal \mathbf{B} field strength is small.	Large-scale flux ropes are observed downstream from strong crustal \mathbf{B} fields. About 1/3 events can be detached from the surface. Ion escape rates due to the flux ropes are estimated to be 1–10 % of the total escape during solar minimum.

magnetic flux ropes, additional assumptions had to be made in terms of ionospheric plasma properties (number density, bulk velocity, and temperature) at the MGS altitude to overcome the lack of ion observation by MGS. If the ionospheric plasma properties are available during the magnetic flux rope observations, we will be able to estimate its spatial structure without such additional assumptions. Furthermore, if the ionospheric plasma density can be deduced inside the magnetic flux rope, we will then be able to more quantitatively evaluate the contribution of ion escape rates resulting from the observed magnetic flux rope. To this end, the comprehensive plasma and magnetic field packages on board MAVEN would be helpful. In addition, we could

only investigate characteristics of the magnetic flux ropes observed at the specific altitude and local time, because the MGS orbit had a fixed local time of 2am/2pm and its altitude was approximately 400 km from the surface during the mapping phase. The magnetic flux ropes must be investigated at different and extensive altitudes and local times to determine the contribution of magnetic flux ropes to the atmospheric escape in the Martian plasma environment. The MAVEN observations could be suitable for such a determination because MAVEN is scheduled in an elliptical orbit (inclination: 75°) with a periapsis (apoapsis) of approximately 150 (6,200) km from the surface.

Finally, continuous solar wind monitoring is required to further understand the solar wind dependence of candidate atmospheric escape processes operating on Mars. MEX will continue its plasma measurements around Mars, even after MAVEN arrives at Mars. Simultaneous multi-point observations by MEX and MAVEN will be achieved after September 2014. MEX is scheduled to dedicate its ion observation mode to the solar wind observations after the MAVEN orbit insertion despite MEX being unable to observe the magnetic field. The method implemented in Chapter 4 of this thesis to infer the IMF orientation from the MEX velocity distribution of exospheric picked-up protons will be useful for investigating the solar wind dependence of candidate atmospheric escape processes from Mars.

References

- Acuña, M. H., et al. (1992), Mars Observer magnetic fields investigation, *J. Geophys. Res.*, *97*(E5), 7799–7814, doi:10.1029/92JE00344.
- Acuña, M. H., et al. (1998), Magnetic field and plasma observations at Mars: Initial results of the Mars Global Surveyor mission, *Science*, *279*, 1676–1680, doi:10.1126/science.279.5357.1676.
- Acuña, M. H., et al. (1999), Global Distribution of Crustal Magnetization Discovered by the Mars Global Surveyor MAG/ER Experiment, *Science*, *284*, 790–793, doi:10.1126/science.284.5415.790.
- Albee, A. L., R. E. Arvidson, F. Palluconi, and T. Thorpe (2001), Overview of the Mars Global Surveyor mission, *J. Geophys. Res.*, *106*(E12), 23,291–23,316, doi:10.1029/2000JE001306.
- Barabash, S., and R. Lundin (2006), Introduction ASPERA-3 on Mars Express, *Icarus*, *182*, 301–307, doi:10.1016/j.icarus.2006.02.015.
- Barabash, S., E. Dubinin, N. Pisarenko, R. Lundin, and C. T. Russell (1991), Picked-up protons near Mars: Phobos observations, *Geophys. Res. Lett.*, *18*, 1805–1808, doi:10.1029/91GL02082.
- Barabash, S., et al. (2006), The analyzer of space plasmas and energetic atoms (ASPERA-3) for the Mars Express mission, *Space Sci. Rev.*, *126*, 113–164, doi:10.1007/s11214-006-9124-8.
- Barabash, S., A. Fedorov, R. Lundin, and J.-A. Sauvaud (2007a), Martian atmospheric erosion rates, *Science*, *315*, 501–503, doi:10.1126/science.1134358.

- Barabash, S., et al. (2007b), The loss of ions from Venus through the plasma wake, *Nature*, *450*, 650–653, doi:10.1038/nature06434.
- Beharrell, M. J., and J. A. Wild (2012), Stationary flux ropes at the southern terminator of Mars, *J. Geophys. Res.*, *117*(A16), A12212, doi:10.1029/2012JA017738.
- Bertaux, J.-L., F. Leblanc, O. Witasse, E. Quemerais, J. Lilensten, S. A. Stern, B. Sandel, and O. Korabely (2005), Discovery of an aurora on Mars, *Nature*, *435*, 790–794, doi:10.1038/nature03603.
- Bibring, J.-P., et al. (2004), Perennial water ice identified in the south polar cap of Mars, *Nature*, *428*, 627–630, doi:10.1038/nature02461.
- Böswetter, A., T. Bagdonat, U. Motschmann, and K. Sauer (2004), Plasma boundaries at Mars: a 3-D simulation study, *Ann. Geophys.*, *22*, 4363–4379, doi:10.5194/angeo-22-4363-2004.
- Brain, D. A. (2006), Mars Global Surveyor Measurements of the Martian Solar Wind Interaction, *Space Sci. Rev.*, *126*, 77–112, doi:10.1007/s11214-006-9122-x.
- Brain, D. A., J. S. Halekas, R. Lillis, D. L. Mitchell, R. P. Lin, and D. H. Crider (2005), Variability of the altitude of the Martian sheath, *Geophys. Res. Lett.*, *32*, L18203, doi:10.1029/2005GL023126.
- Brain, D. A., D. L. Mitchell, and J. S. Halekas (2006a), The magnetic field draping direction at Mars from April 1999 through August 2004, *Icarus*, *182*, 464–473, doi:10.1016/j.icarus.2005.09.023.
- Brain, D. A., et al. (2006b), On the origin of aurorae on Mars, *Geophys. Res. Lett.*, *33*, L01201, doi:10.1029/2005GL024782.
- Brain, D. A., A. H. Baker, J. Briggs, J. P. Eastwood, J. S. Halekas, and T.-D. Phan (2010a), Episodic detachment of Martian crustal magnetic fields leading to bulk atmospheric plasma escape, *Geophys. Res. Lett.*, *37*, L14108, doi:10.1029/2010GL043916.

- Brain, D. A., et al. (2010b), A comparison of global models for the solar wind interaction with Mars, *Icarus*, *206*, 139–151, doi:10.1016/j.icarus.2009.06.030.
- Briggs, J. A., D. A. Brain, M. L. Cartwright, J. P. Eastwood, and J. S. Halekas (2011), A statistical study of flux ropes in the Martian magnetosphere, *Planet. Space Sci.*, *59*, 1498–1505, doi:10.1016/j.pss.2011.06.010.
- Cain, J. C., B. B. Ferguson, and D. Mozzoni (2003), An $n = 90$ internal potential function of the Martian crustal magnetic field, *J. Geophys. Res.*, *108*, 5008, doi:10.1029/2000JE001487.
- Carlsson, E., et al. (2006), Mass composition of the escaping plasma at Mars, *Icarus*, *182*, 320–328, doi:10.1016/j.icarus.2005.09.020.
- Carr, M. H. (1996), *Water on Mars*, Oxford University Press, New York.
- Chassefière, E., and F. Leblanc (2004), Mars atmospheric escape and evolution; interaction with the solar wind, *Planet. Space Sci.*, *52*, 1039–1058, doi:10.1016/j.pss.2004.07.002.
- Chaufray, J. Y., R. Modolo, F. Leblanc, G. Chanteur, R. E. Johnson, and J. G. Luhmann (2007), Mars solar wind interaction: Formation of the Martian corona and atmospheric loss to space, *J. Geophys. Res.*, *112*(E11), E09009, doi:10.1029/2007JE002915.
- Chicarro, A., P. Martin, and R. Trautner (2004), The Mars Express mission: An overview, in *Mars Express: A European Mission to the Red Planet*, *European Space Agency Special Publication*, vol. ESA SP-1240, edited by A. Wilson and A. Chicarro, pp. 3–16, ESA Publications Division, ESTEC, Noordwijk, The Netherlands.
- Cloutier, P. A., et al. (1999), Venus-like interaction of the solar wind with Mars, *Geophys. Res. Lett.*, *26*(17), 2685–2688, doi:10.1029/1999GL900591.
- Connerney, J. E. P., M. H. Acuña, P. J. Wasilewski, G. Kletetschka, N. F. Ness, H. Rème, R. P. Lin, and D. L. Mitchell (2001), The Global Magnetic Field of

- Mars and Implications for Crustal Evolution, *Geophys. Res. Lett.*, *28*, 4015–4018, doi:10.1029/2001GL013619.
- Connerney, J. E. P., M. H. Acuña, N. F. Ness, G. Kletetschka, D. L. Mitchell, R. P. Lin, and H. Reñe (2005), Tectonic implications of Mars crustal magnetism, *Proc. Nat. Acad. Sci.*, *102*, 14,970–14,975, doi:10.1073/pnas.0507469102.
- Crider, D. H., D. Vignes, A. M. Krymskii, T. K. Breus, N. F. Ness, D. L. Mitchell, J. A. Slavin, and M. H. Acuña (2003), A proxy for determining solar wind dynamic pressure at Mars using Mars Global Surveyor data, *J. Geophys. Res.*, *108*(A12), 1461, doi:10.1029/2003JA009875.
- Delcourt, D. C., S. Grimald, F. Leblanc, J.-J. Berthelier, A. Millilo, A. Mura, S. Orsini, and T. E. Moore (2003), A quantitative model of the planetary Na⁺ contribution to Mercury's magnetosphere, *Ann. Geophys.*, *21*, 1723–1736, doi:10.5194/angeo-21-1723-2003.
- Dubinin, E., R. Lundin, O. Norberg, and N. Pissarenko (1993), Ion acceleration in the Martian tail: Phobos observations, *J. Geophys. Res.*, *98*, 3991–3997, doi:10.1029/92JA02233.
- Dubinin, E., M. Fränz, J. Woch, S. Barabash, R. Lundin, and M. Yamauchi (2006), Hydrogen exosphere at Mars: Pickup protons and their acceleration at the bow shock, *Geophys. Res. Lett.*, *33*, L22103, doi:10.1029/2006GL027799.
- Dubinin, E., G. Chanteur, M. Fränz, R. Modolo, J. Woch, E. Roussos, S. Barabash, R. Lundin, and J. D. Winningham (2008), Asymmetry of plasma fluxes at Mars. ASPERA-3 observations and hybrid simulations, *Planet. Space Sci.*, *56*, 832–835, doi:10.1016/j.pss.2007.12.006.
- Dubinin, E., M. Fränz, J. Woch, F. Duru, D. Gurnett, R. Modolo, S. Barabash, and R. Lundin (2009), Ionospheric storms on Mars: Impact of the corotating interaction region, *Geophys. Res. Lett.*, *36*, L01105, doi:10.1029/2008GL036559.

- Dubinin, E., M. Fraenz, A. Fedorov, R. Lundin, N. Edberg, F. Duru, and O. Vaisberg (2011), Ion Energization and Escape on Mars and Venus, *Space Sci. Rev.*, *162*, 173–211, doi:10.1007/s11214-011-9831-7.
- Eastwood, J. P., D. A. Brain, J. S. Halekas, J. F. Drake, T. D. Phan, M. Øieroset, D. L. Mitchell, R. P. Lin, and M. Acuña (2008), Evidence for collisionless magnetic reconnection at Mars, *Geophys. Res. Lett.*, *35*, L02106, doi:10.1029/2007GL032289.
- Edberg, N. J. T., M. Lester, S. W. H. Cowley, and A. I. Eriksson (2008), Statistical analysis of the location of the Martian magnetic pileup boundary and bow shock and the influence of crustal magnetic fields, *J. Geophys. Res.*, *113*(A12), A08206, doi:10.1029/2008JA013096.
- Edberg, N. J. T., H. Nilsson, A. O. Williams, M. Lester, S. E. Milan, S. W. H. Cowley, M. Fränz, S. Barabash, and Y. Futaana (2010), Pumping out the atmosphere of Mars through solar wind pressure pulses, *Geophys. Res. Lett.*, *37*, L03107, doi:10.1029/2009GL041814.
- Edberg, N. J. T., et al. (2011), Atmospheric erosion of Venus during stormy space weather, *J. Geophys. Res.*, *116*, A09308, doi:10.1029/2011JA016749.
- Elphic, R. C., and C. T. Russell (1983a), Global characteristics of magnetic flux ropes in the Venus ionosphere, *J. Geophys. Res.*, *88*, 2993–3003, doi:10.1029/JA088iA04p02993.
- Elphic, R. C., and C. T. Russell (1983b), Magnetic flux ropes in the Venus ionosphere - Observations and models, *J. Geophys. Res.*, *88*, 58–72, doi:10.1029/JA088iA01p00058.
- Elphic, R. C., and C. T. Russell (1983c), Evidence for helical kink instability in the Venus magnetic flux ropes, *Geophys. Res. Lett.*, *10*, 459–462, doi:10.1029/GL010i006p00459.
- Elphic, R. C., C. T. Russell, J. A. Slavin, and L. H. Brace (1980), Observations of the dayside ionopause and ionosphere of Venus, *J. Geophys. Res.*, *85*, 7679–7696, doi:10.1029/JA085iA13p07679.

- Ergun, R. E., L. Andersson, W. K. Peterson, D. Brain, G. T. Delory, D. L. Mitchell, R. P. Lin, and A. W. Yau (2006), Role of plasma waves in Mars' atmospheric loss, *Geophys. Res. Lett.*, *33*, L14103, doi:10.1029/2006GL025785.
- Fang, X., M. W. Liemohn, A. F. Nagy, Y. Ma, D. L. De Zeeuw, J. U. Kozyra, and T. H. Zurbuchen (2008), Pickup oxygen ion velocity space and spatial distribution around Mars, *J. Geophys. Res.*, *113*(A12), A02210, doi:10.1029/2007JA012736.
- Fang, X., M. W. Liemohn, A. F. Nagy, J. G. Luhmann, and Y. Ma (2010a), Escape probability of Martian atmospheric ions: Controlling effects of the electromagnetic fields, *J. Geophys. Res.*, *115*(A14), A04308, doi:10.1029/2009JA014929.
- Fang, X., M. W. Liemohn, A. F. Nagy, J. G. Luhmann, and Y. Ma (2010b), On the effect of the martian crustal magnetic field on atmospheric erosion, *Icarus*, *206*, 130–138, doi:10.1016/j.icarus.2009.01.012.
- Fedorov, A., et al. (2006), Structure of the martian wake, *Icarus*, *182*, 2, doi:10.1016/j.icarus.2005.09.021.
- Fedorov, A., et al. (2008), Comparative analysis of Venus and Mars magnetotails, *Planet. Space Sci.*, *56*, 812–817, doi:10.1016/j.pss.2007.12.012.
- Feldman, W. C., et al. (2002), Global Distribution of Neutrons from Mars: Results from Mars Odyssey, *Science*, *297*, 75–78, doi:10.1126/science.1073541.
- Feldman, W. C., et al. (2004), Global distribution of near-surface hydrogen on Mars, *J. Geophys. Res.*, *109*, E09006, doi:10.1029/2003JE002160.
- Fox, J. L. (2009), Morphology of the dayside ionosphere of Mars: Implications for ion outflows, *J. Geophys. Res.*, *114*(E13), E12005, doi:10.1029/2009JE003432.
- Fränz, M., et al. (2006), Plasma moments in the environment of Mars. Mars Express ASPERA-3 Observations, *Space Sci. Rev.*, *126*, 165–207, doi:10.1007/s11214-006-9115-9.

- Fränz, M., E. Dubinin, E. Nielsen, J. Woch, S. Barabash, R. Lundin, and A. Fedorov (2010), Transterminator ion flow in the Martian ionosphere, *Planet. Space Sci.*, *58*, 1442–1454, doi:10.1016/j.pss.2010.06.009.
- Futaana, Y., et al. (2008), Mars Express and Venus Express multi-point observations of geoeffective solar flare events in December 2006, *Planet. Space Sci.*, *56*, 873–880, doi:10.1016/j.pss.2007.10.014.
- Futaana, Y., S. Barabash, M. Holmström, A. Fedorov, H. Nilsson, R. Lundin, E. Dubinin, and M. Fränz (2010), Backscattered solar wind protons by Phobos, *J. Geophys. Res.*, *115*(A14), A10213, doi:10.1029/2010JA015486.
- Galli, A., P. Wurz, H. Lammer, H. I. M. Lichtenegger, R. Lundin, S. Barabash, A. Grigoriev, M. Holmström, and H. Gunell (2006), The Hydrogen Exospheric Density Profile Measured with ASPERA-3/NPD, *Space Sci. Rev.*, *126*, 447–467, doi:10.1007/s11214-006-9089-7.
- Gosling, J. T., and V. J. Pizzo (1999), Formation and Evolution of Corotating Interaction Regions and their Three Dimensional Structure, *Space Sci. Rev.*, *89*, 21–52, doi:10.1023/A:1005291711900.
- Greeley, R., N. Lancaster, S. Lee, and P. Thomas (1992), Martian aeolian processes, sediments, and features, in *Mars*, edited by H. H. Kieffer et al., pp. 730–766, University of Arizona Press, Tucson.
- Gurnett, D. A., et al. (2005), Radar Soundings of the Ionosphere of Mars, *Science*, *310*, 1929–1933, doi:10.1126/science.1121868.
- Gurnett, D. A., et al. (2008), An overview of radar soundings of the martian ionosphere from the Mars Express spacecraft, *Adv. Space Res.*, *41*, 1335–1346, doi:10.1016/j.asr.2007.01.062.
- Halekas, J. S., and D. A. Brain (2010), Global distribution, structure, and solar wind control of low altitude current sheets at Mars, *Icarus*, *206*, 64–73, doi:10.1016/j.icarus.2008.12.032.

- Halekas, J. S., D. A. Brain, R. J. Lillis, M. O. Fillingim, D. L. Mitchell, and R. P. Lin (2006), Current sheets at low altitudes in the Martian magnetotail, *Geophys. Res. Lett.*, *33*, L13101, doi:10.1029/2006GL026229.
- Halekas, J. S., D. A. Brain, R. P. Lin, J. G. Luhmann, and D. L. Mitchell (2008), Distribution and variability of accelerated electrons at Mars, *Adv. Space Res.*, *41*, 9, doi:10.1016/j.asr.2007.01.034.
- Halekas, J. S., J. P. Eastwood, D. A. Brain, T. D. Phan, M. Øieroset, and R. P. Lin (2009), In situ observations of reconnection Hall magnetic fields at Mars: Evidence for ion diffusion region encounters, *J. Geophys. Res.*, *114*(A13), A11204, doi:10.1029/2009JA014544.
- Halekas, J. S., D. A. Brain, and J. P. Eastwood (2011), Large-amplitude compressive “sawtooth” magnetic field oscillations in the Martian magnetosphere, *J. Geophys. Res.*, *116*, A07222, doi:10.1029/2011JA016590.
- Hanson, W. B., S. Sanatani, and D. R. Zuccaro (1977), The Martian ionosphere as observed by the Viking retarding potential analyzers, *J. Geophys. Res.*, *82*, 4351–4363, doi:10.1029/JS082i028p04351.
- Hara, T., K. Seki, Y. Futaana, M. Yamauchi, M. Yagi, Y. Matsumoto, M. Tokumaru, A. Fedorov, and S. Barabash (2011), Heavy-ion flux enhancement in the vicinity of the Martian ionosphere during CIR passage: Mars Express ASPERA-3 observations, *J. Geophys. Res.*, *116*, A02309, doi:10.1029/2010JA015778.
- Hara, T., K. Seki, Y. Futaana, M. Yamauchi, S. Barabash, A. O. Fedorov, M. Yagi, and D. C. Delcourt (2013), Statistical properties of planetary heavy-ion precipitations toward the Martian ionosphere obtained from Mars Express, *J. Geophys. Res. Space Physics*, *118*, 5348–5357, doi:10.1002/jgra.50494.
- Hara, T., K. Seki, H. Hasegawa, D. A. Brain, K. Matsunaga, and M. H. Saito (2014), The spatial structure of Martian magnetic flux ropes recovered by the Grad-Shafranov reconstruction technique, *J. Geophys. Res. Space Physics*, *119*, doi:10.1002/2013JA019414.

- Hasegawa, H., et al. (2004), Reconstruction of two-dimensional magnetopause structures from Cluster observations: verification of method, *Ann. Geophys.*, *22*, 1251–1266, doi:10.5194/angeo-22-1251-2004.
- Hasegawa, H., B. U. Ö. Sonnerup, B. Klecker, G. Paschmann, M. W. Dunlop, and H. Rème (2005), Optimal reconstruction of magnetopause structures from Cluster data, *Ann. Geophys.*, *23*, 973–982, doi:10.5194/angeo-23-973-2005.
- Hasegawa, H., B. U. Ö. Sonnerup, C. J. Owen, B. Klecker, G. Paschmann, A. Balogh, and H. Rème (2006), The structure of flux transfer events recovered from Cluster data, *Ann. Geophys.*, *24*, 603–618, doi:10.5194/angeo-24-603-2006.
- Hau, L.-N., and B. U. Ö. Sonnerup (1999), Two-dimensional coherent structures in the magnetopause: Recovery of static equilibria from single-spacecraft data, *J. Geophys. Res.*, *104*, 6899–6918, doi:10.1029/1999JA900002.
- Hu, Q., and B. U. Ö. Sonnerup (2002), Reconstruction of magnetic clouds in the solar wind: Orientations and configurations, *J. Geophys. Res.*, *107*, 1142, doi:10.1029/2001JA000293.
- Hu, Q., C. W. Smith, N. F. Ness, and R. M. Skoug (2004), Multiple flux rope magnetic ejecta in the solar wind, *J. Geophys. Res.*, *109*, A03102, doi:10.1029/2003JA010101.
- Jakosky, B. M., and R. J. Phillips (2001), Mars' volatile and climate history, *Nature*, *412*, 237–244, doi:10.1038/35084184.
- James, P. B., H. H. Kieffer, and D. A. Paige (1992), The seasonal cycle of carbon dioxide on Mars, in *Mars*, edited by H. H. Kieffer et al., pp. 934–968, University of Arizona Press, Tucson.
- Johnson, R. E., and J. G. Luhmann (1998), Sputter contribution to the atmospheric corona on Mars, *J. Geophys. Res.*, *103*(E2), 3649–3654, doi:10.1029/97JE03266.
- Kallio, E., J.-Y. Chaufray, R. Modolo, D. Snowden, and R. Winglee (2011), Modeling of Venus, Mars, and Titan, *Space Sci. Rev.*, *162*, 267–307, doi:10.1007/s11214-011-9814-8.

- Kivelson, M. G., and C. T. Russell (1995), *Introduction to Space Physics*, Cambridge atmospheric and space science series, Cambridge University Press.
- Knudsen, W. C., K. Spenser, K. L. Miller, and V. Novak (1980), Transport of ionospheric O⁺ ions across the Venus terminator and implications, *J. Geophys. Res.*, *85*(A13), 7803–7810, doi:10.1029/JA085iA13p07803.
- Knudsen, W. C., P. M. Banks, and K. L. Miller (1982), A new concept of plasma motion and planetary magnetic field for Venus, *Geophys. Res. Lett.*, *9*(7), 765–768, doi:10.1029/GL009i007p00765.
- Krymskii, A. M., T. K. Breus, N. F. Ness, M. H. Acuña, J. E. P. Connerney, D. H. Crider, D. L. Mitchell, and S. J. Bauer (2002), Structure of the magnetic field fluxes connected with crustal magnetization and topside ionosphere at Mars, *J. Geophys. Res.*, *107*(A9), 1245, doi:10.1029/2001JA000239.
- Lammer, H., H. I. M. Lichtenegger, C. Kolb, I. Ribas, E. F. Guinan, R. Abart, and S. J. Bauer (2003), Loss of water from Mars: Implications for the oxidation of the soil, *Icarus*, *165*, 9–25, doi:10.1016/S0019-1035(03)00170-2.
- Lammer, H., et al. (2013), Outgassing History and Escape of the Martian Atmosphere and Water Inventory, *Space Sci. Rev.*, *174*, 113–154, doi:10.1007/s11214-012-9943-8.
- Law, C. C., and P. A. Cloutier (1995), Observations of magnetic structure at the dayside ionopause of Venus, *J. Geophys. Res.*, *100*, 23,973–23,982, doi:10.1029/95JA02756.
- Leblanc, F., and R. E. Johnson (2001), Sputtering of the Martian atmosphere by solar wind pick-up ions, *Planet. Space Sci.*, *49*, 6, doi:10.1016/S0032-0633(01)00003-4.
- Leblanc, F., and R. E. Johnson (2002), Role of molecular species in pickup ion sputtering of the Martian atmosphere, *J. Geophys. Res.*, *107*(E2), 5010, doi:10.1029/2000JE001473.

- Li, L., Y. Zhang, Y. Feng, X. Fang, and Y. Ma (2011), Oxygen ion precipitation in the Martian atmosphere and its relation with the crustal magnetic fields, *J. Geophys. Res.*, *116*(A15), A08204, doi:10.1029/2010JA016249.
- Luhmann, J. G., and T. E. Cravens (1991), Magnetic fields in the ionosphere of Venus, *Space Sci. Rev.*, *55*, 201–274, doi:10.1007/BF00177138.
- Luhmann, J. G., and R. C. Elphic (1985), On the dynamo generation of flux ropes in the Venus ionosphere, *J. Geophys. Res.*, *90*, 12,047–12,056, doi:10.1029/JA090iA12p12047.
- Luhmann, J. G., and J. U. Kozyra (1991), Dayside pickup oxygen ion precipitation at Venus and Mars - Spatial distributions, energy deposition and consequences, *J. Geophys. Res.*, *96*(A4), 5457–5467, doi:10.1029/90JA01753.
- Luhmann, J. G., R. E. Johnson, and M. H. G. Zhang (1992), Evolutionary impact of sputtering of the Martian atmosphere by O⁺ pickup ions, *Geophys. Res. Lett.*, *19*(21), 2151–2154, doi:10.1029/92GL02485.
- Luhmann, J. G., W. T. Kasprzak, and C. T. Russell (2007), Space weather at Venus and its potential consequences for atmosphere evolution, *J. Geophys. Res.*, *112*, E04S10, doi:10.1029/2006JE002820.
- Luhmann, J. G., et al. (2008), Venus Express observations of atmospheric oxygen escape during the passage of several coronal mass ejections, *J. Geophys. Res.*, *113*, E00B04, doi:10.1029/2008JE003092.
- Lundin, R. (2011), Ion Acceleration and Outflow from Mars and Venus: An Overview, *Space Sci. Rev.*, *162*, 309–334, doi:10.1007/s11214-011-9811-y.
- Lundin, R., H. Borg, B. Hultqvist, A. Zakharov, and R. Pellinen (1989), First measurements of the ionospheric plasma escape from Mars, *Nature*, *341*, 609–612, doi:10.1038/341609a0.

- Lundin, R., O. Norberg, E. M. Dubinin, N. Pisarenko, and H. Koskinen (1991), On the momentum transfer of the solar wind to the Martian topside ionosphere, *Geophys. Res. Lett.*, *18*, 1059–1062, doi:10.1029/90GL02604.
- Lundin, R., et al. (2004), Solar wind induced atmospheric erosion at Mars: First results from ASPERA-3 on Mars Express, *Science*, *305*, 1933–1936, doi:10.1126/science.1101860.
- Lundin, R., et al. (2006a), Plasma Acceleration Above Martian Magnetic Anomalies, *Science*, *311*, 980–983, doi:10.1126/science.1122071.
- Lundin, R., et al. (2006b), Auroral Plasma Acceleration Above Martian Magnetic Anomalies, *Space Sci. Rev.*, *126*, 333–354, doi:10.1007/s11214-006-9086-x.
- Lundin, R., H. Lammer, and I. Ribas (2007), Planetary Magnetic Fields and Solar Forcing: Implications for Atmospheric Evolution, *Space Sci. Rev.*, *129*, 245–278, doi:10.1007/s11214-007-9176-4.
- Lundin, R., S. Barabash, M. Holmström, H. Nilsson, M. Yamauchi, M. Fränz, and E. M. Dubinin (2008a), A comet-like escape of ionospheric plasma from Mars, *Geophys. Res. Lett.*, *35*, L18203, doi:10.1029/2008GL034811.
- Lundin, R., S. Barabash, A. Fedorov, M. Holmström, H. Nilsson, J.-A. Sauvaud, and M. Yamauchi (2008b), Solar forcing and planetary ion escape from Mars, *Geophys. Res. Lett.*, *35*, L09203, doi:10.1029/2007GL032884.
- Lundin, R., S. Barabash, M. Holmström, H. Nilsson, M. Yamauchi, E. M. Dubinin, and M. Fränz (2009), Atmospheric origin of cold ion escape from Mars, *Geophys. Res. Lett.*, *36*, L17202, doi:10.1029/2009GL039341.
- Lundin, R., S. Barabash, M. Yamauchi, H. Nilsson, and D. Brain (2011a), On the relation between plasma escape and the Martian crustal magnetic field, *Geophys. Res. Lett.*, *38*, L02102, doi:10.1029/2010GL046019.

- Lundin, R., S. Barabash, E. Dubinin, D. Winningham, and M. Yamauchi (2011b), Low-altitude acceleration of ionospheric ions at Mars, *Geophys. Res. Lett.*, *38*, L08108, doi:10.1029/2011GL047064.
- Lundin, R., S. Barabash, M. Holmström, H. Nilsson, Y. Futaana, R. Ramstad, M. Yamauchi, E. Dubinin, and M. Fraenz (2013), Solar cycle effects on the ion escape from Mars, *Geophys. Res. Lett.*, *40*, 6028–6032, doi:10.1002/2013GL058154.
- Ma, Y., A. F. Nagy, K. C. Hansen, D. L. DeZeeuw, T. I. Gombosi, and K. G. Powell (2002), Three-dimensional multispecies MHD studies of the solar wind interaction with Mars in the presence of crustal fields, *J. Geophys. Res.*, *107*(A10), 1282, doi:10.1029/2002JA009293.
- Ma, Y., A. F. Nagy, I. V. Sokolov, and K. C. Hansen (2004), Three-dimensional, multispecies, high spatial resolution MHD studies of the solar wind interaction with Mars, *J. Geophys. Res.*, *109*(A18), A07211, doi:10.1029/2003JA010367.
- Ma, Y. J., A. F. Nagy, C. T. Russell, R. J. Strangeway, H. Y. Wei, and G. Toth (2013), A global multispecies single-fluid MHD study of the plasma interaction around Venus, *J. Geophys. Res. Space Physics*, *118*, 321–330, doi:10.1029/2012JA018265.
- McClements, K. G., and R. O. Dendy (1993), Ion Cyclotron Harmonic Wave Generation by Ring Protons in Space Plasmas, *J. Geophys. Res.*, *98*(A7), 11,689–11,700, doi:10.1029/93JA00158.
- McEnulty, T. R., J. G. Luhmann, I. de Pater, D. A. Brain, A. Fedorov, T. L. Zhang, and E. Dubinin (2010), Interplanetary coronal mass ejection influence on high energy pick-up ions at Venus, *Planet. Space Sci.*, *58*, 1784–1791, doi:10.1016/j.pss.2010.07.019.
- Mitchell, D. L., R. P. Lin, H. Rème, D. H. Crider, P. A. Cloutier, J. E. P. Connerney, M. H. Acuña, and N. F. Ness (2000), Oxygen Auger electrons observed in Mars' ionosphere, *Geophys. Res. Lett.*, *27*(13), 1871–1874, doi:10.1029/1999GL010754.
- Mitchell, D. L., R. P. Lin, C. Mazelle, H. Rème, P. A. Cloutier, J. E. P. Connerney, M. H. Acuña, and N. F. Ness (2001), Probing Mars' crustal magnetic field and

- ionosphere with the MGS Electron Reflectometer, *J. Geophys. Res.*, *106*(E10), 23,419–23,428, doi:10.1029/2000JE001435.
- Modolo, R., G. M. Chanteur, E. Dubinin, and A. P. Matthews (2005), Influence of the solar EUV flux on the Martian plasma environment, *Ann. Geophys.*, *23*, 433–444, doi:10.5194/angeo-23-433-2005.
- Morgan, D. D., D. A. Gurnett, D. L. Kirchner, J. L. Fox, E. Nielsen, and J. J. Plaut (2008), Variation of the Martian ionospheric electron density from Mars Express radar soundings, *J. Geophys. Res.*, *113*, A09303, doi:10.1029/2008JA013313.
- Morgan, D. D., D. A. Gurnett, F. Akalin, D. A. Brain, J. S. Leisner, F. Duru, R. A. Frahm, and J. D. Winningham (2011), Dual-spacecraft observation of large-scale magnetic flux ropes in the Martian ionosphere, *J. Geophys. Res.*, *116*(A15), A02319, doi:10.1029/2010JA016134.
- Nagy, A. F., J. Kim, and T. E. Cravens (1990), Hot hydrogen and oxygen atoms in the upper atmospheres of Venus and Mars, *Ann. Geophys.*, *8*, 251–256.
- Nagy, A. F., et al. (2004), The plasma Environment of Mars, *Space Sci. Rev.*, *111*, 33–114, doi:10.1023/B:SPAC.0000032718.47512.92.
- Nilsson, H., et al. (2006), Investigation of the Influence of Magnetic Anomalies on Ion Distributions at Mars, *Space Sci. Rev.*, *126*, 355–372, doi:10.1007/s11214-006-9030-0.
- Nilsson, H., E. Carlsson, D. A. Brain, M. Yamauchi, M. Holmström, S. Barabash, R. Lundin, and Y. Futaana (2010), Ion escape from Mars as a function of solar wind conditions: A statistical study, *Icarus*, *206*, 40–49, doi:10.1016/j.icarus.2009.03.006.
- Nilsson, H., N. J. T. Edberg, G. Stenberg, S. Barabash, M. Holmström, Y. Futaana, R. Lundin, and A. Fedorov (2011), Heavy ion escape from Mars, influence from solar wind conditions and crustal magnetic fields, *Icarus*, *215*, 475–484, doi:10.1016/j.icarus.2011.08.003.

- Okamoto, T. J., et al. (2008), Emergence of a Helical Flux Rope under an Active Region Prominence, *Astrophys. J. Lett.*, *673*, L215–L218, doi:10.1086/528792.
- Penz, T., et al. (2004), Ion loss on Mars caused by the Kelvin-Helmholtz instability, *Planet. Space Sci.*, *52*, 1157–1167, doi:10.1016/j.pss.2004.06.001.
- Pèrez-de-Tejada, H. (1987), Plasma flow in the Mars magnetosphere, *J. Geophys. Res.*, *92*(A5), 4713–4718, doi:10.1029/JA092iA05p04713.
- Pèrez-de-Tejada, H. (1998), Momentum transport in the solar wind erosion of the Mars ionosphere, *J. Geophys. Res.*, *103*(E13), 31,499–31,508, doi:10.1029/1998JE900001.
- Phan, T. D., G. Paschmann, J. T. Gosling, M. Oieroset, M. Fujimoto, J. F. Drake, and V. Angelopoulos (2013), The dependence of magnetic reconnection on plasma β and magnetic shear: Evidence from magnetopause observations, *Geophys. Res. Lett.*, *40*, 11–16, doi:10.1029/2012GL054528.
- Qiu, J., Q. Hu, T. A. Howard, and V. B. Yurchyshyn (2007), On the Magnetic Flux Budget in Low-Corona Magnetic Reconnection and Interplanetary Coronal Mass Ejections, *Astrophys. J.*, *659*, 758–772, doi:10.1086/512060.
- Ramstad, R., Y. Futaana, S. Barabash, H. Nilsson, S. Martin Del Campo B, R. Lundin, and K. Schwingenschuh (2013), Phobos 2/ASPERA data revisited: Planetary ion escape rate from Mars near the 1989 solar maximum, *Geophys. Res. Lett.*, *40*, 477–481, doi:10.1002/grl.50149.
- Richardson, I. G., et al. (2006), Major geomagnetic storms ($\text{Dst} \leq -100$ nT) generated by corotating interaction regions, *J. Geophys. Res.*, *111*, A07S09, doi:10.1029/2005JA011476.
- Russell, C. T., and R. C. Elphic (1979), Observation of magnetic flux ropes in the Venus ionosphere, *Nature*, *279*, 616–618, doi:10.1038/279616a0.
- Shiota, D., K. Kusano, T. Miyoshi, and K. Shibata (2010), Magnetohydrodynamic Modeling for a Formation Process of Coronal Mass Ejections: Interaction Between

- an Ejecting Flux Rope and an Ambient Field, *Astrophys. J.*, *718*, 1305–1314, doi:10.1088/0004-637X/718/2/1305.
- Shizgal, B. D., and G. G. Arkos (1996), Nonthermal escape of the atmospheres of Venus, Earth, and Mars, *Rev. Geophys.*, *34*, 483–505, doi:10.1029/96RG02213.
- Shue, J.-H., J. K. Chao, H. C. Fu, C. T. Russell, P. Song, K. K. Khurana, and H. J. Singer (1997), A new functional form to study the solar wind control of the magnetopause size and shape, *J. Geophys. Res.*, *102*, 9497–9512, doi:10.1029/97JA00196.
- Slavin, J. A., et al. (2009), MESSENGER Observations of Magnetic Reconnection in Mercury’s Magnetosphere, *Science*, *324*(5927), 606–610, doi:10.1126/science.1172011.
- Sonnerup, B. U. Ö., and M. Guo (1996), Magnetopause transects, *Geophys. Res. Lett.*, *23*, 3679–3682, doi:10.1029/96GL03573.
- Sonnerup, B. U. Ö., H. Hasegawa, and G. Paschmann (2004), Anatomy of a flux transfer event seen by Cluster, *Geophys. Res. Lett.*, *31*, L11803, doi:10.1029/2004GL020134.
- Strangeway, R. J., and C. T. Russell (1996), Plasma waves and field-aligned currents in the Venus plasma mantle, *J. Geophys. Res.*, *101*(A8), 17,313–17,324, doi:10.1029/96JA00927.
- Sturrock, P. A. (1994), *Plasma Physics: An Introduction to the Theory of Astrophysical, Geophysical and Laboratory Plasmas*, Stanford-Cambridge program, Cambridge University Press.
- Swisdak, M., B. N. Rogers, J. F. Drake, and M. A. Shay (2003), Diamagnetic suppression of component magnetic reconnection at the magnetopause, *J. Geophys. Res.*, *108*, 1218, doi:10.1029/2002JA009726.
- Swisdak, M., M. Opher, J. F. Drake, and F. Alouani Bibi (2010), The Vector Direction

- of the Interstellar Magnetic Field Outside the Heliosphere, *Astrophys. J.*, *710*, 1769–1775, doi:10.1088/0004-637X/710/2/1769.
- Tanaka, K. L., D. H. Scott, and R. Greeley (1992), Global stratigraphy, in *Mars*, edited by H. H. Kieffer et al., pp. 345–382, University of Arizona Press, Tucson.
- Terada, N., S. Machida, and H. Shinagawa (2002), Global hybrid simulation of the Kelvin-Helmholtz instability at the Venus ionopause, *J. Geophys. Res.*, *107*(A2), 1471, doi:10.1029/2001JA009224.
- Terada, N., Y. N. Kulikov, H. Lammer, H. I. M. Lichtenegger, T. Tanaka, H. Shinagawa, and T. Zhang (2009), Atmosphere and water loss from early Mars under extreme solar wind and extreme ultraviolet conditions, *Astrobiology*, *9*, 55–70, doi:10.1089/ast.2008.0250.
- Tsurutani, B. T., et al. (2006), Corotating solar wind streams and recurrent geomagnetic activity: A review, *J. Geophys. Res.*, *111*, A07S01, doi:10.1029/2005JA011273.
- Vennerstrom, S., N. Olsen, M. Purucker, M. H. Acuña, and J. C. Cain (2003), The magnetic field in the pile-up region at Mars, and its variation with the solar wind, *Geophys. Res. Lett.*, *30*(7), 1369, doi:10.1029/2003GL016883.
- Vignes, D., M. H. Acuña, J. E. P. Connerney, D. H. Crider, H. Rème, and C. Mazelle (2004), Magnetic Flux Ropes in the Martian Atmosphere: Global Characteristics, *Space Sci. Rev.*, *111*, 223–231, doi:10.1023/B:SPAC.0000032716.21619.f2.
- Withers, P. (2009), A review of observed variability in the dayside ionosphere of Mars, *Adv. Space Res.*, *44*, 277–307, doi:10.1016/j.asr.2009.04.027.
- Wolff, R. S., B. E. Goldstein, and C. M. Yeates (1980), The onset and development of Kelvin-Helmholtz instability at the Venus ionopause, *J. Geophys. Res.*, *85*(A13), 7697–7707, doi:10.1029/JA085iA13p07697.
- Yagi, M., K. Seki, Y. Matsumoto, D. C. Delcourt, and F. Leblanc (2010), Formation of a sodium ring in Mercury’s magnetosphere, *J. Geophys. Res.*, *115*(A14), A10253, doi:10.1029/2009JA015226.

- Yamauchi, M., et al. (2006), IMF direction derived from cycloid-like ion distributions observed by Mars Express, *Space Sci. Rev.*, *126*, 239–266, doi:10.1007/s11214-006-9090-1.
- Yamauchi, M., et al. (2008), Advanced method to derive the IMF direction near Mars from cycloidal proton distributions, *Planet. Space Sci.*, *56*, 1145–1154, doi:10.1016/j.pss.2008.02.012.
- Yamauchi, M., et al. (2011), Comparison of accelerated ion populations observed upstream of the bow shocks at Venus and Mars, *Ann. Geophys.*, *29*, 511–528, doi:10.5194/angeo-29-511-2011.
- Yamauchi, M., et al. (2012), Ion acceleration by multiple reflections at Martian bow shock, *Earth, Planets, and Space*, *64*, 61–71, doi:10.5047/eps.2011.07.007.
- Yeroshenko, Y., W. Riedler, K. I. Schwingenschuh, J. G. Luhmann, M. Ong, and C. T. Russell (1990), The magnetotail of Mars: Phobos observations, *Geophys. Res. Lett.*, *17*, 885–888, doi:10.1029/GL017i006p00885.

Publications

- [1] **Hara, T.**, K. Seki, Y. Futaana, M. Yamauchi, M. Yagi, Y. Matsumoto, M. Tokumaru, A. Fedorov, and S. Barabash (2011), Heavy-ion flux enhancement in the vicinity of the Martian ionosphere during CIR passage: Mars Express ASPERA-3 Observations, *J. Geophys. Res.*, *116*, A02309, doi:10.1029/2010JA015778.
- [2] **Hara, T.**, K. Seki, Y. Futaana, M. Yamauchi, S. Barabash, A. O. Fedorov, M. Yagi, and D. C. Delcourt (2013), Statistical properties of planetary heavy-ion precipitations toward the Martian ionosphere obtained from Mars Express, *J. Geophys. Res. Space Physics*, *118*, 5348–5357, doi:10.1002/jgra50494.
- [3] **Hara, T.**, K. Seki, H. Hasegawa, D. A. Brain, K. Matsunaga, and M. H. Saito (2014), The spatial structure of Martian magnetic flux ropes recovered by the Grad-Shafranov reconstruction technique, *J. Geophys. Res. Space Physics*, *119*, doi:10.1002/2013JA019414.
- [4] **Hara, T.**, K. Seki, H. Hasegawa, D. A. Brain, K. Matsunaga, M. H. Saito, and D. Shiota (2014), Study on formation processes of Martian flux ropes downstream from crustal magnetic fields based on Grad-Shafranov reconstruction, *submitted to J. Geophys. Res. Space Physics*.
- [5] Shiota, D., R. Kataoka, Y. Miyoshi, **T. Hara**, C. Tao, K. Masunaga, Y. Futaana, and N. Terada (2014), Inner heliosphere MHD modeling applicable to space weather forecasting for the other planets, *submitted to Space Weather*.